UC Berkeley
UC Berkeley Electronic Theses and Dissertations

Title

Wearable Sweat Sensors for Personalized Health Monitoring

Permalink

https://escholarship.org/uc/item/325259gg

Author

Bariya, Mallika S.

Publication Date

2021

Peer reviewed|Thesis/dissertation

Wearable Sweat Sensors for Personalized Health Monitoring

by

Mallika S. Bariya

A dissertation submitted in partial satisfaction of the

requirements for the degree of

Doctor of Philosophy

in

Engineering – Materials Science and Engineering

in the

Graduate Division

of the

University of California, Berkeley

Committee in charge:

Professor Ali Javey, co-Chair

Professor Junqiao Wu, co-Chair

Professor Mark Asta

Professor Ana Claudia Arias

Spring 2021

Wearable Sweat Sensors for Personalized Health Monitoring

Copyright 2021

by

Mallika S. Bariya

Abstract

Wearable Sweat Sensors for Personalized Health Monitoring

By

Mallika S. Bariya

Doctor of Philosophy in Materials Science and Engineering

University of California, Berkeley

Professor Ali Javey, co-Chair

Wearable sensors that allow continuous, real-time, and point-of-care monitoring of body state have many advantages over invasive, hospital-based tests. Wearable sensors that probe the chemical state of the body by measuring analytes in sweat have generated particular interest in recent years, due to sweat's rich composition and ease of access. Preliminary studies have revealed that sweat composition and secretion rate may indicate blood concentrations or health conditions including dehydration, metabolic conditions, and stress, enabling physiological health to be tracked dynamically without painful, disruptive, and discrete tests. However, accessing sweat for measurement poses unique challenges. Sensors must limit evaporation and mixing of old and fresh sweat, must be robust under the mechanical rigors of prolonged on-body wear, and must be expanded towards low sweat volumes and secretion rates in order to collect sweat without needing to exercise. Careful interpretation of sensor measurements must also be performed to account for cross-dependencies between measured parameters and to develop personalized and universal correlations between sweat measurements and established health metrics.

In this dissertation, I discuss the vision of wearable sweat sensors for personalized health monitoring and present technological progress towards realizing this goal. Chapter 1 introduces background and challenges of sweat sensing, as well as key considerations and components of wearable sweat sensors. Chapter 2 addresses high-throughput fabrication of electrochemical sweat sensors via roll-to-roll processing. Chapter 3 discusses the integration of microfluidics to enable dynamic sweat capture and analysis of both composition and sweat secretion rate, with a focus on sweat that is secreted via exercise or local drug-based stimulation. Chapter 4 moves beyond these disruptive modes of sweat generation to present a platform for rapidly accumulating and analyzing sweat at rest, via functionalized gloves that dramatically inhibit evaporation. Chapter 5 presents a complementary system using microfluidics to dynamically monitor sweat at rest, including while sitting and sleeping. Throughout these chapters, small-scale human subject trials and studies highlight the potential of wearable sweat sensors for personalized health and fitness monitoring applications. Chapter 6 concludes by discussing work that must be done to enable sweat sensing to become a viable and ubiquitous tool for health monitoring outside the lab.

Table of Contents

Acknowledgements

There are many people I want to thank for supporting me over the last five years. Foremost, I would like to thank Professor Ali Javey for his guidance and vision. I have learned invaluable skills as a researcher, collaborator, mentor, and communicator during my time in his lab, and I will carry these with me throughout my life.

I would like to thank the other members of my qualifying and dissertation committees – Professor Junqiao Wu, Professor Mark Asta, Professor Ana Claudia Arias, Professor Jie Yao, and Professor Liwei Lin. Their suggestions and feedback provided fresh perspectives on my research and have greatly strengthened this dissertation.

I am so grateful for my lab colleagues. Hnin Yin Yin Nyein and Li-Chia Tai were wonderful friends and mentors, and I am privileged to have worked with such kind, open, and skilled researchers for many years. I would also like to thank the rest of the sensor subgroup over the years, including Wei Gao, Lu Li, Zhen Yuan, Yuanjin Lin, Jiangqi Zhao, Lei Hou, Serena Blacklow, Noelle Davis, Tiffany Liaw, Christine Ahn, Ziba Shahpar, Minghan Chao, and Rahul Ghattamaneni. Our research and personal discussions, both in and out of lab, were a highlight of grad school. Beyond our group, I'm grateful for long-term collaborations with Dr. Jussi Hiltunen and Liam Gillan at VTT Finland and with Professor Gyoujin Cho's group at Sunchon National University. I also want to thank the members and staff of the research centers I have been a part of, including NASCENT at Austin and BSAC at Berkeley, for opportunities to share my research and interact with the broader academic community.

I want to thank my friends and family for their unending encouragement and support over the last five years. This dissertation is dedicated to my grandparents Seema, Ajit, and Jayantilal, my parents Suhag and Anand, and to Suhita and Hari, Mohini, and Ven. I would not have made it through grad school without you. You have done more for me than I can ever express.

Chapter 1: Introduction to wearable sweat sensors

The following chapter has been previously published in a similar format, and is reprinted and/or adapted with permission from the following work:

M. Bariya, H. Y. Y. Nyein, A. Javey. Wearable Sweat Sensors. *Nat Electron,* **2018**, *1*, 160-171.

1.1 Introduction

Healthcare systems today are mostly reactive. Patients contact doctors *after* they have developed ailments with noticeable symptoms, and are thereafter passive recipients of care and monitoring by specialists. This approach largely fails in preventing the onset of health conditions, prioritizing diagnostics and treatment over proactive healthcare. It further occludes individuals from being active agents in monitoring their own health.

The growing field of wearable sensors (*i.e.*, wearables) aims to tackle the limitations of centralized, reactive healthcare by giving individuals insight into the dynamics of their own physiology. The long-term vision is to develop sensors that can be integrated into wearable formats like clothing, wristbands, patches, or tattoos to continuously probe a range of body indicators. By relaying physiological information as the body evolves over healthy and sick states, these sensors will enable individuals to monitor themselves without expensive equipment or trained professionals (**Fig. 1**). Various physical and chemical sensors will need to be integrated to obtain a complete picture of dynamic health. These sensors will generate vast time-series of data that will need to be parsed with big data techniques to generate personalized baselines indicative of the user's health[1–4]. Sensor readings that cohere with the established baseline can then indicate the body is in a healthy, equilibrium state, while deviations from the baseline can provide early warning about developing health conditions. Eventually, deviations caused by different pathologies can be "fingerprinted" to make diagnosis more immediate and autonomous. Together, the integration of wearables with big data analytics can enable individualized fitness monitoring, early detection of developing health conditions, and better management of chronic diseases. This envisioned medical landscape built around continuous, point-of-care sensing spearheads personalized, predictive, and ultimately preventive healthcare.

1.2 The case for sweat-based wearables

While available wearables mostly track indicators like heart rate and physical activity, they fail to provide information at a deeper, molecular level. This technological gap has encouraged rapid advancement in chemical sensors that can non-invasively detect analytes in accessible biofluids, providing a window into the body's overall dynamic biomolecular state[5–15]. There are several candidate biofluids but most have limitations for wearable sensing. Blood and interstitial fluid (IF) can be continuously probed by implantable devices but are difficult to access non-

Figure 1: Big Data for Human Health. In the envisioned landscape of personalized medical and fitness monitoring, wearable sensors integrated into 'smart' wristbands or patches will generate vast quantities of data potentially indicative of human health. Collected sensor readings can be parsed with big data techniques to uncover actionable correlations between molecular indicators and health state. These discoveries will enable point-of-care detection of developing health conditions for personalized and ultimately preventive healthcare.

invasively through a wearable platform. Tears can be uncomfortable or risky to source, and irritation can produce reflex tears that confound sensor readings[5]. Urine-based sensors cannot be implemented in a wearable format, while the composition of saliva, highly altered by one's last meal, may provide limited physiological insight. In contrast, sweat shows great promise for wearable sensing. It can be generated non-invasively and on-demand (such as through local chemical stimulation) at convenient locations on the body, ideal for continuous monitoring. Sensors can be placed close to the site of sweat generation, allowing for fast detection before analytes biodegrade. While sweat presents its own challenges for reliably measuring and interpreting biomarker concentrations, its advantages over other biofluids have rapidly promoted it to the forefront of wearable technology innovation[16].

Sweat contains a wealth of chemical information that could potentially indicate the body's deeper biomolecular state (**Table 1** in the Appendix of this chapter). While probing blood or interstitial fluid can directly reflect certain diseases, the relation between sweat analyte levels and health status is still poorly understood. To understand how sweat analytes correlate with blood or IF levels, and hence the utility of probing sweat for medical or fitness monitoring, it is crucial to first understand the mechanisms by which analytes are partitioned into sweat.
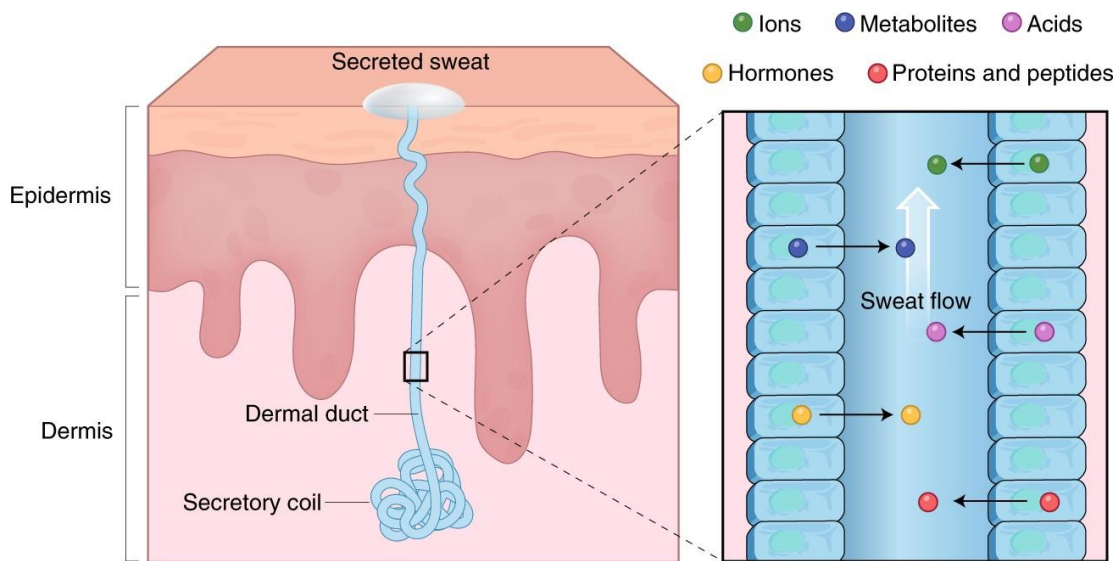
2

Figure 2: Sweat Gland Structure and Biomarker Partitioning. Eccrine sweat glands are comprised of a secretory coil where sweat is first generated and a dermal duct that conveys sweat through the epidermis to the skin surface. In the process, a variety of analytes including ions, metabolites, acids, hormones, proteins, and peptides are partitioned into sweat from nearby blood and interstitial fluid[17]. Adapted by permission from Macmillan Publishers Ltd.

Most accessible sweat comes from eccrine glands composed of a secretory coil, where sweat is first generated, and a dermal duct that carries sweat to the skin surface[17]. During this process, analytes including ions, metabolites, acids, hormones, and small proteins and peptides are partitioned into sweat (**Fig. 2**). The most abundant ion species are Na^+ and Cl^-, responsible for the production of sweat. Na^+ and Cl^- are actively transported between blood and the secretory coil to create an osmolality difference that forces water into the sweat gland. As sweat flows through the dermal duct, Na^+ and Cl^- are reabsorbed through channels in the dermal duct walls. The rate of reabsorption is fairly constant and causes Na^+ and Cl^- in the final secreted sweat to typically increase with sweat rate[18].

The secretion mechanisms of most other analytes in sweat are poorly understood, though many are theorized to passively or actively partition from nearby blood or IF. The exact method of partitioning, combined with factors including size, charge, and dependence on sweat rate, impact the final concentration of analytes in secreted sweat. Ions including Ca^{2+} and K^+ are present in mM ranges. Weak acids or bases, such as ammonia, can diffuse into the sweat gland and ionize due to high sweat pH, trapping them in the secretory coil and producing mM concentrations several times higher than in blood. Other species, including lactate and urea, could partition from blood or be generated during the sweat gland's own metabolic activity, producing mM levels. Larger molecules like glucose can be found in the µM range, orders of magnitude lower than in blood, while proteins including hormones and neuropeptides occur in nM or pM traces[18]. Apart from naturally generated analytes, alcohols, drugs, and heavy metals can also be secreted in sweat as the body attempts to eject toxins[19–22].

The composition of sweat depends not only on mechanisms of analyte partitioning but also the method of sweat stimulation. Sweat produced as a result of exercise, heat, stress, or chemical stimulation can be expected to vary in composition, and the type of sweat sourced for wearable sensing must be application driven. For example, sweat produced during vigorous exercise, when the body undergoes rapid physiological changes, will have dynamic analyte profiles that reflect high metabolic activity[6]. While this is pertinent to fitness monitoring, medical screenings are better realized with "equilibrium" sweat sourced from the body at rest[7]. This can be achieved with local chemical stimulation of the sweat glands, a process called iontophoresis that will be discussed in detail further on. For now, it is important to remember that the method of biomarker arrival in the sweat gland, coupled with the method of eliciting sweat secretion, act together to determine final biomarker concentrations in sweat and their correlation with the body's overall physiological state.

Using sweat to non-invasively probe the body is not a new concept. Historically, the canonical case of sweat-based medical screening has been for cystic fibrosis (CF)[23]. CF is a progressive disease that ravages the lungs while also causing Cl^- reabsorption channels in sweat glands to malfunction. Patients with CF have unusually high Cl^- in their sweat. Iontophoretic sweat collection and testing can provide quick screenings and are the clinical standard for CF diagnosis today. Sweat also has historic relevance for drug testing in sports[24]. Sweat patches worn by athletes can absorb drug metabolites in sweat and retroactively reveal if the athlete doped during a competition. Common methods of obscuring urine-based drug tests, including drinking extra fluid, do not easily translate to sweat. Sweat patches are thus an attractive alternative to urine-based or more invasive tests.

Despite its advantages for select applications, off-body sweat sensing involves large overheads as sweat samples must be collected, stored, and remotely tested in a lab by trained professionals with expensive equipment. It is difficult to obtain large enough sample volumes and avoid evaporation, and chemical degradation between sweat collection and testing can limit the sensitivity and reliability of off-body tests. In contrast, wearable sweat sensors can restrict sweat collection and analysis to the point of generation, allowing for autonomous and even continuous sensing without the intervention of specialists. For applications including athletics that involve dynamic physiological changes, wearable sensors can provide immediate measurements that can keep individuals informed of their health state at dramatically reduced time scales compared to off-body sweat tests. However, on-body sweat sensing grapples with its own problems involving low sweat volumes, irregular sweating without stimulation, possibility of biodegradation or evaporation. These challenges, which must be tackled with technological and scientific solutions, more precisely include:

1. *Low sweat rates*
   Sweat secretion rates during exertive exercise reach about 20 nL/gland/min[18]. In a 1 cm^2 area on the forehead or arm, only about 3 µL of sweat are generated per minute, with sedentary sweat rates still lower. Sweat rates can also be expected to vary with factors including activity intensity and hydration level, and differ broadly between individuals.

Sensors that are robust across these conditions and able to detect analytes in small quantities of fluid must be singularly scaled and sensitive.

2. *Sample evaporation*

   While restricting sensing to the point of secretion largely addresses this issue, evaporation can still be problematic as it acts quickly on small volumes of exposed sweat, changing the concentration of constituent biomarkers. Fast detection is needed to ensure sensor readings are not corrupted by evaporation artefacts.

3. *Contamination from skin*

   Chemicals absorbed into skin from cosmetic products or environmental exposure can leech into secreted sweat. Incorporating ways to isolate sweat from the skin surface is crucial to prevent these chemical interferents from skewing sensor readings.

4. *Obtaining fresh sweat*

   New sweat secreted onto the skin surface mixes with older sweat. Without techniques to control sweat flow such that detection only occurs in the freshest sweat, sensor readings can at best give rolling averages of analyte profiles rather than real-time measurements.

5. *Sweat rate effects*

   Various analyte concentrations are dependent on sweat rate. Na^+ and Cl^- aid in sweat generation and are typically more concentrated at higher sweat rates. For larger molecules, it is possible that higher sweat rates afford less time for concentrations to equilibrate across sweat glands and the surrounding blood or IF[18]. This implies that while sweat sensor readings may be accurate, they are heavily dependent on the rate at which analytes are extracted to the skin surface instead of being purely reflective of analyte levels in blood or IF. Identifying and compensating for sweat rate effects is necessary if sweat composition is to be correlated with analyte levels deeper in the body.

Several of these challenges can be addressed through technological innovation at a device level. Addressing sweat rate effects is more complex, requiring a holistic understanding of biomarker partitioning mechanisms and their dependence on sweat rate. While expanding our fundamental knowledge of sweat gland physiology can help address this problem, an alternate method is to conduct large-scale correlation studies with multiplexed sensing to characterize sweat rate dependencies. This will be discussed in greater detail later on.

1.3 State-of-the-art wearable sweat sensors

Many wearable sweat sensors have been developed in recent years (**Fig. 3**) and combine different form factors, substrates, and detection mechanisms[6,8,9,19]. For continuous fitness monitoring, sensors integrated into common athletic accessories like wristbands or headbands can be comfortably worn with minimal obstruction of motion. For medical uses, patch-style formats are preferable and can discreetly adhere to the skin with greater flexibility of location. Built-in iontophoresis capabilities can be included for local extraction of equilibrium sweat. To implement these form factors, a variety of substrates have been demonstrated including temporary tattoos, soft polymers, and hybrid systems combining flexible plastics with traditional silicon integrated
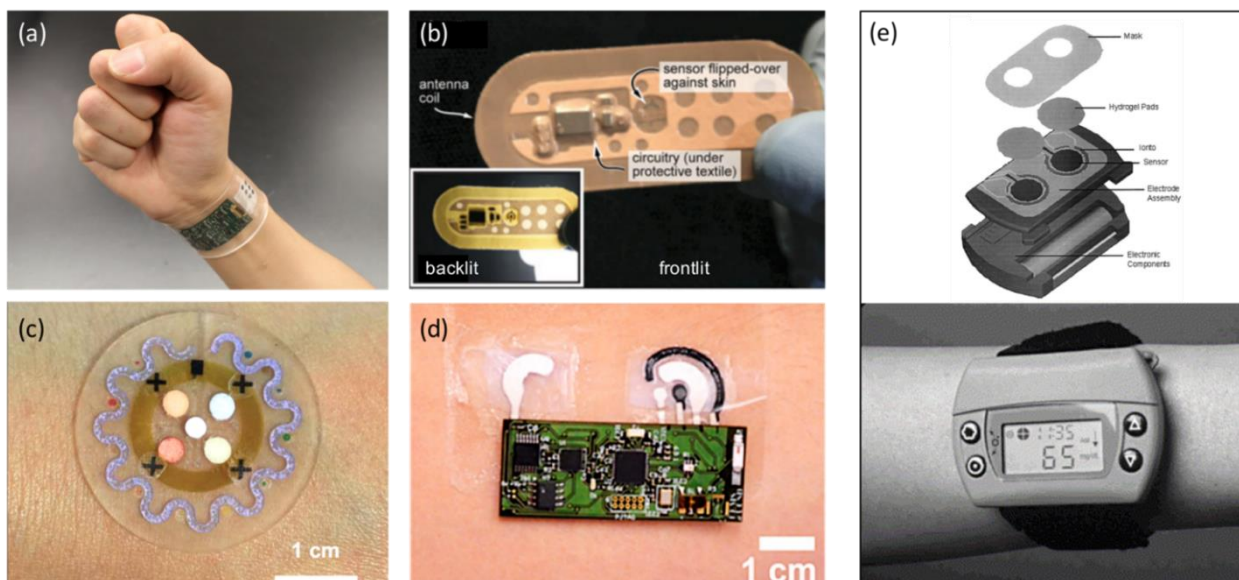
Figure 3: Wearable Sweat Sensors. (a) A multiplexed electrochemical system for continuous monitoring of a panel of analytes in sweat, integrated into a 'smart' wristband for fitness monitoring. Wireless transmission to a custom phone app allows easy readout of analyte concentrations[6]. **(b)** A Band-Aid-style patch for continuous detection of ions in sweat, with RFID antenna for wireless signal transmission. Adapted with permission from reference[9]. **(c)** One-time, colorimetric detection of sweat analytes is realized using colorimetric assay reagents encased in microfluidic wells[8]. Reprinted with permission from AAAS. **(d)** Screen-printed electrodes on a tattoo substrate achieve ethanol detection in iontophoretic sweat. Reprinted (adapted) with permission from[19]. Copyright (2016) American Chemical Society. **(e)** GlucoWatch used reverse iontophoresis for semi-continuous glucose measurement[36,37]. Republished with permission of P.B. Hoeber from[37]; permission conveyed through Copyright Clearance Center, Inc. Reprinted from[36] with permission from Elsevier.

circuits (ICs)[6,8,11,12,25]. Various sensing mechanisms are available to detect analytes in sweat. The most common and versatile method is electrochemical detection, which measures currents or potentials at functionalized electrodes to transduce analyte concentrations[25]. Another prominent technique is colorimetric detection, relying on reagents that undergo measurable color changes upon exposure to their target analytes[8,26]. Still other methods include impedance-based and optical sensing[27–29]. While several of these techniques have been used for sensing simple ions and metabolites, in future they can be combined with developments in affinity-based aptamers or synthetic polymer templates for selective recognition of more complex molecules[30–32]. However, more work is needed to explore the robustness of these latter methods for on-body sensing. To contextualize these sensor design choices and indicate some of the challenges for reliable sensing, we will now explore a number of representative sweat sensors in detail. These devices give a sense of how far sweat sensing technology has advanced and indicate where further innovation is needed.

Fig. 3(a) shows a wearable electrochemical sensor packaged as a wristband, capable of measuring ions and metabolites simultaneously[6]. The sensing component employs a flexible plastic substrate with electrodes functionalized towards different analytes, allowing continuous, multiplexed measurements. A soft polymeric well can surround the sensing electrodes to absorb pressure variations while also creating a chamber for sweat to fill. This minimizes sweat evaporation and keeps the sensing electrodes from abrading through direct skin contact. A printed circuit board (PCB) calibrates raw analyte signals into meaningful concentrations and transmits to a customized phone app for easy read-out. This is ideal for fitness monitoring, providing profiles of changing analyte concentrations that can inform the user of depleting electrolytes or dehydration. However, care must be taken to prevent delamination of the flexible components during exercise.

Fig. 3(b) shows an RFID chip adapted for electrochemical sensing of ions in sweat[9]. Sensing electrodes are electroplated onto the same substrate as the wireless transmission component, allowing the whole device to be condensed into a wearable patch similar to a Band-Aid. This form factor enables intimate contact between sensor and skin, and allows the device to be worn anywhere on the body. The RFID antenna transmits analyte readings to a smartphone for continuous monitoring during exercise. However, this sensor relies on near-field communication (NFC) between the smartphone and passive patch components in order to trigger sensing and data transmission. While basic charge storage components are included in the patch to allow short-term, low-power processes to continue even when the smartphone is temporarily out of range, the smartphone must be held in close proximity for normal operation and presents risks of disconnection and lost data. This system thus constitutes a semi-wearable, non-autonomous platform in which the user must be actively involved to bring about sensing.

Fig. 3(c) shows a sensor that utilizes colorimetric detection[8]. A microfluidic base guides sweat into chambers containing reagents that change color according to the concentration of their target analytes. A custom phone app can image the sensor to convert color into concentration. This device allows simultaneous measurement of metabolites, pH, and sweat rate while minimizing contamination from skin. The soft substrate and adhesive provide easy mounting, and the colorimetric scheme affords minimal power consumption. This device can give quick analyte estimates during exercise when highly resolved quantification is not necessary, but it does not allow for continuous measurement or hands-off imaging. As the goal for wearables is to allow autonomous sensing with minimal user involvement in the sensor detection or transmission pathways, this sensor represents a semi-wearable prototype that will need to be modified to allow user-independent sensing.

Wearable sensors can alternately be designed to locally stimulate sweating via iontophoresis. This allows equilibrium sweat to be sourced without the need for exercise, ideal for medical screenings in sedentary situations. In addition to sensing electrodes, iontophoretic devices must include additional electrodes for local current application (**Fig. 4(a)**)[7]. Hydrogels cast on these electrodes entrap a sweat-inducing drug that is driven under the skin by current flow. Sweat
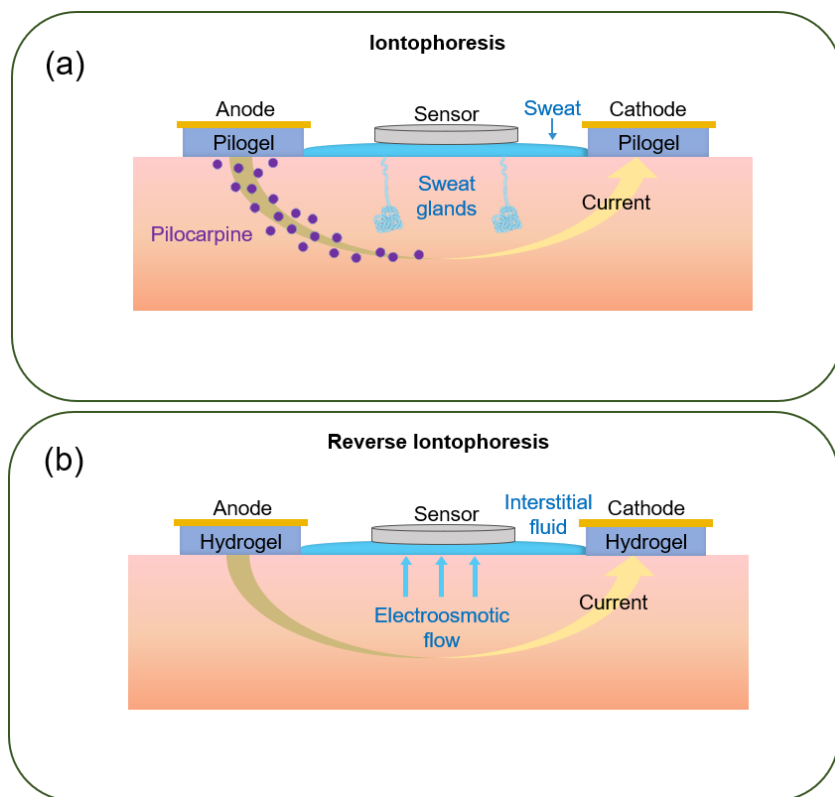
Figure 4: Iontophoresis and Reverse Iontophoresis. (a) Iontophoresis relies on topical current application for local sweat stimulation. Current is applied between Pilogels, or hydrogels containing the sweat stimulating drug pilocarpine. The drug is driven beneath the skin surface and triggers nearby glands to secrete sweat, which wearable sensors can then access. **(b)** Reverse iontophoresis uses current application to electro-osmotically drive interstitial fluid (IF) through the epidermis to the skin surface. No drug is involved in this case – hydrogels simply isolate the current applying electrodes from the skin surface to prevent irritation. Analytes that are advectively transported to the skin surface along with IF can be detected by wearable sensors. Note: schematics are not to scale.

glands in the vicinity are then stimulated to secrete sweat that can be used to detect "equilibrium" analyte levels.

Fig. 3(d) shows a temporary tattoo-based biosensor capable of conducting iontophoresis and detecting ethanol in induced sweat[19]. The sensing component includes electrochemical electrodes screen-printed onto temporary-tattoo paper. A small PCB attached to the tattoo controls iontophoresis and allows transmission of alcohol measurements. This patch design offers a discreet and non-obtrusive form factor for decentralized screening of alcohol abuse. While the tattoo-based design allows for easy wear and highly conformal contact, induced sweat is not contained and subject to evaporation, and the high degree of contact can create noisy artefacts from movement

or strain of the underlying skin. Additionally, this system may be better suited for one-time use rather than continuous monitoring as repeated application of iontophoretic current at the same location can be harmful to the underlying skin[33]. **Fig. 3(e)** depicts GlucoWatch, an electrochemical wearable that was commercialized but ultimately discontinued[34–37]. GlucoWatch aimed for semi-continuous glucose sensing for diabetes management using a process called reverse iontophoresis (**Fig 4(b)**). Like iontophoresis, reverse iontophoresis relies on topical current application to extract biofluid. In this case, no drug is involved – the current electro-osmotically extracts interstitial fluid instead of sweat, and molecules like glucose are transported to the skin surface advectively. Glucose in IF correlates well with plasma levels, and GlucoWatch showed great promise for non-invasive diabetes monitoring[38]. However, users complained of skin burning due to repeated high current application, and the sensor was eventually withdrawn from market. This underscores the technical challenges that still oppose continuous IF or sweat induction for medical monitoring. One-time application of iontophoresis or reverse iontophoresis works well for diagnostics, but devices with lower current density requirements – or alternate technological solutions – are needed to expand its applicability.

1.4 Sweat sensor components

Having surveyed some representative sweat sensing platforms, we can now review the fundamental characteristics of a sweat sensor. Different detection schemes have different platform and system requirements. While colorimetric, optical, and other methods have advantages for certain applications, electrochemical techniques have shown more widespread success for point-of-care biofluid analysis to date[5,39]. For this reason, we choose to focus on the unique requirements for electrochemical sweat sensors going forward. These devices comprise of two integrated parts: a sensing component with functionalized electrodes to transduce analyte concentrations into electrical signals, and an electronic component to process, calibrate, and transmit these signals for easy read-out. We will review requirements for each component and techniques to optimize their performance.

1.4.1 Sensing component

- Sensor-body interface

A key requirement for wearable sensors is that they minimally impact user mobility and comfort while being resilient to the mechanical strains and distortions that accompany on-body use. For this reason, sensing components are ideally fabricated on substrates that are soft, deformable, and do not delaminate from the underlying skin. Materials including fabrics, paper, and soft polymers and plastics have been common choices[40,41]. Electrode fabrication methods that have shown success on flexible substrates include photolithography and printing techniques such as screen printing, flexography, and gravure printing[42]. Roll-to-roll compatible fabrication holds particular promise for delivering the large scale, high throughput processing necessary for commercial viability. Considerations for using flexible substrate-based sensing components include ensuring functional membrane layers deform along with the substrate without rupturing

and sensor working area does not change dramatically during deformation to avoid motion-related signal artefacts. For printed components, optimization of ink composition and pre-processing can address these challenges. Another criterion for flexible sensors is that electrodes fabricated on the substrate robustly connect to electronics or wireless transmission components. Especially in hybrid systems that combine soft sensing components with more rigid electronic platforms, weak connections between the components can cause signal error or even disconnection under mechanical strain or motion[43]. More rigid sensing substrates, such as flexible PET, can sometimes afford more robust connection to electronics than highly deformable materials like paper laminates, in which case trade-offs must be made to achieve an optimal system. Miniaturizing the sensing component so that the skin it contacts is locally flat is another approach to achieving a sound sensor-body interface. This method helps to relax deformability requirements on the substrate.

- ▪ Sensing modalities

Electrochemical methods have advantages over other chemical detection schemes due to their high sensitivity, selectivity, low response times, and ease of adaption for wearable formats. In recent years, various electrochemical sensing modalities have been demonstrated towards wearable sweat analysis. These include potentiometry, chronoamperometry, square wave anodic stripping voltammetry (SWASV), cyclic voltammetry (CV), differential pulse voltammetry (DPV), and electrochemical impedance spectroscopy (EIS). Potentiometric techniques, in which potentials of the sensing electrodes undergo measurable changes with target analyte concentration, have shown great utility for detecting the dominant ion species in sweat, including Na^+, K^+ and Ca^{2+} [6,7,44,45]. Chronoamperometry is frequently used for enzyme-based sensing, detecting current produced during triggered redox reactions of the target analyte at a constant applied potential[7,18,19,45,46]. For instance, glucose oxidase enzyme entrapped on a sensing electrode interacts with glucose in sweat to produce a current proportional to glucose concentration[6,7,46]. Other sensing modalities such as SWASV, CV, DPV, and EIS have been utilized for detection of heavy metals, drugs, and hormones[20,47–51]. Voltammetry measurements are performed by sweeping through the potential range in which redox reaction of the target species occurs, and the redox current peaks are subsequently measured. Specifically, CV is widely used for preliminary electrochemical characterization of the sensor to explore electron transfer kinetics and redox processes, and towards detecting molecules including glucose, uric and ascorbic acid in sweat[47,52,53]. DPV is used for detecting organic and inorganic species by stimulating them to bind on the sensor surface, and is commonly used to detect proteins[31,54,55]. SWASV is a technique that has shown success for detection of trace metals, especially when combined with effective pre-concentration of the target species onto the sensing surface to amplify the signal. Despite attaining low level detection, major problems with voltammetry methods include the overlap of redox potentials, presence of interfering compounds active on the sensing surface, and the formation of intermetallic compounds that degrade the detection signal[54]. EIS is used to transduce bioaffinity binding by analyzing complex impedances in Nyquist plots, and can sometimes serve as an

alternate detection modality to voltammetric methods. However, EIS typically requires longer measurement periods and post-processing to counter larger uncertainties[56]. **Table 1** surveys the sensing modalities used for different analytes in greater detail, while **Table 2** in the Appendix of this chapter summarizes how the advantages and disadvantages of each modality impact its suitability for different targets.

- ▪ Sensing attributes

To allow for robust and accurate quantification of analytes, several attributes of sweat sensors must be optimized. These include selectivity, sensitivity, limit of detection, stability, response time, and reproducibility. Below, we discuss steps to optimize these attributes with major focus on the ion-selective and enzymatic sensors that have dominated sweat sensing to date.

1. Selectivity

Selectivity is the ability of a sensor to preferentially detect its target analyte in the presence of other potentially interfering species. This is the most fundamental requirement for a biosensor, and is realized by using selective recognition elements on the sensing electrode (**Table 1** in the Appendix of this chapter). Ion-selective electrodes (ISEs) use permselective lipophilic ion exchangers and ion-selective ionophores to achieve this attribute[57]. ISE selectivity has been explored using table-top ionic solutions but the complexity of sweat means that their performance must be further validated for *in situ* sweat sensing[57,58]. Work within the wearable sensing community has shown that pH and Na^+ ISEs retain remarkable selectivity in sweat[6,7,44,45,59,60]. In contrast, sensors relying on redox reactions for detection usually have difficulty achieving high selectivity. Even when target-specific enzymes are incorporated, high voltages may need to be applied to trigger the enzymatic reaction. These voltages can prompt other electrochemically active compounds in sweat to undergo redox transitions as well, creating interfering signals. To address this problem, an electron transfer mediator can be incorporated to lower the redox potential of the target reaction[61,62]. This technique is canonically used in glucose sensors, which combine a Prussian Blue mediator with glucose oxidase enzyme to preferentially detect glucose[63]. Similar to the high target specificity afforded by enzymes, biosensors based on antibodies and aptamers bind to their specific target with high affinity based on precise 3D compatibility of their receptors with target molecules. However, bioaffinity-based sensors are challenging to implement in wearable formats due to long response times, difficult detection procedures, and limited reusability[64]. These issues will be explored in greater detail further on[65]. Another key factor that influences selectivity is biofouling, the accumulation of chemical species on the sensing layer that gradually degrades sensor performance over time. This effect can be reduced by incorporating semipermeable membranes like Nafion and cellulose acetate for size and charge exclusion, or adding pre-oxidizing layers at the front end of the sensing interface to inactivate electroactive interferents[61,66].

2. Sensitivity

Sensitivity is a measure of how acutely the sensor signal changes in response to changes in analyte concentration. Calibration curves of sensor signal against step-wise increased analyte

concentration can be generated and the sensor sensitivity extracted as the slope of the curve in cases where hysteresis is negligible. As many important sweat analytes are normally well-regulated to remain within a tight concentration range, highly sensitive sensors are required to capture small but physiologically relevant fluctuations in concentration[18,59]. This is particularly relevant when continuous monitoring of the evolution of biomarker profiles is needed, such as for tracking electrolyte levels during exercise. However, applications including certain drug or blood alcohol content (BAC) tests may require only binary information to determine the presence or absence of a drug above a predefined tolerance level. In these cases, sensors need not have very high sensitivity but must be able to distinguish between concentrations above or below the threshold. The sensitivity of potentiometric sensors is typically governed by the Nernst equation, which predicts that an electrode at ambient temperature will undergo a 59 mV step in potential per 10x change in monovalent ion concentration. Higher valence ions will produce a smaller step. Though uncommon, it is possible to achieve beyond-Nernstian slopes to improve sensitivity of higher valence species by incorporating lipophilic anionic sites and acidic ionophores[67]. Increasing enzyme loading within enzymatic sensing electrodes can improve sensitivity by amplifying measured currents, as can pre-concentration of target species for voltammetric sensing of larger molecules[20,68,69]. Including nanomaterials such as carbon nanotubes (CNTs) or metal nanoparticles can improve electron transfer kinetics through the sensing stack to further amplify detection currents[68]. However, care must be taken to ensure these nanomaterials do not leech into skin during on-body use[70].

3. Detection limit

Detection limit indicates the lowest concentration a sensor can discern and stems from signal to noise ratios. Noise can arise from interfering analytes, sensor drift, or local concentration variations amongst a host of other sources. Improving detection limits requires amplifying the target signal or suppressing background noise, both of which can be achieved with the right materials and detection schemes. Sensors should be engineered to have their detection limit lie below the physiologically relevant concentration range of their target analyte. Detection limits as low as 10^{-8} to 10^{-11} M can be achieved with ion-selective electrodes. These low bounds are achieved by electrochemical deposition of conducting polymers like polypyrrole, which have been explored for trace-level monitoring[71]. Detection limits of enzymatic and voltammetric sensors can be lowered by using nanoparticles and nanostructures to improve binding affinity or increase the number of reaction sites[72,73]. Still, many chemical species including proteins and peptides occur in extremely trace concentrations, and further work is needed to reduce sweat sensor detection limits for these complexes.

4. Stability

Stability refers to a sensor's ability to maintain its signal over time without attenuation by drift or degradation. All electrochemical sensors suffer from signal drift, which can create accumulated errors over time that are especially damaging for continuous measurements. This

limits the sensor lifetime for long-term operation. Sources of signal drift vary with detection method. In ion-selective sensors, formation of a thin aqueous layer between the sensing membrane and underlying conductive electrode can cause changes in effective compositions of the sensor stack itself over time, producing potential drifts[74]. Adding hydrophobic chemical species can minimize this effect, while electrochemically depositing conducting polymers such as polystyrene, polypyrrole, and polyaniline further improve stability[75,76]. Drift issues also afflict enzymatic sensors. Enzymes can be chemically inactivated due to byproducts of redox reactions and can even detach from the sensing membrane over time, causing signal attenuation and loss of sensitivity. Passivation of electrode active sites and biofouling create further issues[77]. These effects can be minimized by immobilizing enzymes in support matrices, crosslinking with polymers, and forming polyionic-enzyme complexes for enzyme retention[78,79]. However, chemically modifying enzymes in this way can reduce their activity, so a balance must be struck to optimize both stability and sensitivity.

5. *Response time*

Response time governs how long it takes for the sensor response to stabilize to a reliable value when analyte concentration changes. For continuous monitoring, having fast response times is critical to ensure dynamic changes in sweat composition are captured in near-real time. Response times are usually influenced by the target analyte, sample composition, mass transport and reaction rates, as well as the activity of the recognition element. Transport and reaction kinetics can be improved by optimizing thickness and permeability of the sensing membrane[77]. Typically, addition of antifouling layers delays the response time by presenting barriers to diffusion. Faster response times are generally achieved when activities of recognition species are high and the thickness of the sensing stack is low.

6. *Reproducibility*

To be valuable to the larger community for point-of-care health monitoring, sensors must perform reliably and require minimal overhead before use to accurately extract concentration measurements from sensor signals. To achieve this, performance across many sensors of the same kind must be reproducible. A single calibration curve should be uniformly applicable across these sensors so that the sensing characteristics of each device need not be extensively measured individually before use. One-point calibration will be necessary to account for baseline differences in sensor signals, but a universal calibration curve ensures that *only* one preliminary measurement is required, minimizing the complexity of device set up and preparation before on-body use. The degree of reproducibility required depends on sensor sensitivity and the smallest change in analyte concentration that can be considered physiologically significant. Then, reproducibility entails that sensors of the same kind must produce signals that, after conditioning, translate to the same concentration with deviation within the physiologically relevant delta in concentration. Drift can lead to greater spread in sensor readings and usually must also be reduced to improve raw signal precision across a collection of sensing components. Sensor development in academic settings

typically involves manual drop-casting of functionalized layers onto the sensing electrodes, which can lead to performance variations due to human error. This can be minimized by moving towards controlled fabrication methods such as screen-printing and roll-to-roll processes that allow high-throughput production of sensors with high uniformity. The vision will be to incorporate ink-based printing of electrodes and sensing membranes as well as integration of microfluidics and electronics via roll-to-roll fabrication.

1.4.2 Electronic component

Sensing components are not functional in themselves without electronics to enact appropriate detection schemes, process the sensor signals, filter noise, and transmit final calibrated readings for easy readability and display. Here we discuss the role of electronics within electrochemical sweat sensing platforms.

Some of the most successful sweat sensing platforms utilize hybrid electronics, combining flexible sensing substrates that conform to the body with traditional silicon ICs for signal processing and transmission. Various topologies and substrates are available for electronic components, including soft plastics or polymers with printed conductive elements or flexible PCBs[6–9,19]. Of these, PCBs have shown particular promise as they can be mass produced cost-effectively using existing industrial processes. PCBs designed with off-the-shelf components have been well suited for research-level development of sweat sensor prototypes, but application specific integrated circuits (ASICs) can in future enable more miniaturized systems that consolidate different electrical processes for lower power consumption while improving wearability.

Minimizing power consumption is a key consideration for developing wearables that allows sensors to operate continuously for longer periods of time. To understand where power drain is dominant in a typical wearable sweat sensor and how it can be reduced, we will consider the platform presented by Gao et al which allows continuous, multiplexed sensing of ions and metabolites[6]. The electronic backbone of this device comprises of an analog front-end to condition the sensor signal, an analog-to-digital converter (ADC), a pre-programmed microcontroller that calibrates the signal into concentration values, and a Bluetooth transmission component to relay this reading to a paired phone app for easy read-out. Power consumption in the analog front-end arises from active components including op-amps and amounts to a few mW depending on the exact circuitry, with similar power also being drawn by the ADC and microcontroller. The Bluetooth transmission component uses around 30 mW and dominates power consumption in this device, but can be improved upon using newer technology including Bluetooth Low Energy (BLE)[80]. Depending on the application, periodic transmission by which the device alternates between data transferring and low-power states can be sufficient when only semi-continuous analyte readings are needed, and could further decrease energy overheads[65,81]. Apart from Bluetooth, near-field communication (NFC) modalities can enable signal transmission without the need to battery-power transmission components within the sensor itself, instead allowing power

from the receiving device to trigger sensor measurement and data collection. However, this affords much shorter-range interaction between the sensor and receiving phone, in some cases preventing continuous, autonomous sensing without user involvement in bringing the receiver close to the sensor. A third data relaying option involves directly showing sensor readings on a display. However, without appended capabilities for storing and downloading data, this topology prevents data accumulation or dissemination to healthcare providers and is therefore less attractive for integrated health monitoring applications. Overall, the choice of wireless communication protocol depends on a host of criteria including power consumption, data generation rates, bandwidth requirements, and compatibility with the remaining sensor circuitry[82]. Beyond integrating low-power transmission components, harvesting energy from heat, motion, or the environment and developing wearable energy storage options such as miniaturized supercapacitors is another area of active research for lowering power consumption in wearable devices[65,83].

Filtering raw sensor signals to eliminate noise is a key role of electronic components. Motion can contribute to noise, particularly by altering connectivity and impedances at the interface between the sensing component and PCB. Low pass filters can be included in the analog front-end to eliminate high frequency noise from motion or fluctuations in the sensing layer environment. Different sensing modalities will need to preserve DC, transient, or AC signal components depending on whether the sensor is designed for potentiometric or amperometric sensing, voltammetric techniques, or impedance-based sensing; appropriate filtering and conditioning pathways to isolate the desired signal components must be developed accordingly. The filter orders and cut-off frequencies can also be tailored according to the sensing scheme and data sampling rate. Other examples of noise and unwanted signal artefacts arise during certain types of multiplexed measurement. When passive measurements of current or potential are combined with active measurements that require applying and scanning voltages, the applied fields can interfere with passive electrode readings. Switches can be incorporated to alternate between sensing pathways and thereby prevent crosstalk and electromagnetic interference.

For many sweat sensor prototypes, signal transduction occurs at the sensing component while signal conditioning is restricted to the electronic component. This model is effective when sensor working areas and signal amplitudes are large enough that the process of signal transfer between sensing component and signal conditioning unit does not produce significant attenuation or noise. However, as working electrode areas are miniaturized, the signals generated by area-dependent sensors (such as enzymatic sensors) are reduced and it becomes important to minimize signal loss between transduction and conditioning. In such cases, conditioning may need to be shifted towards the transducer by incorporating elements directly onto the sensing component.

While interest primarily focuses on the device aspects of sweat-based wearables, attention must also be diverted to the wider framework in which they will be used. This is critical in order to tackle privacy and safety challenges associated with continuous, personalized health monitoring and big data processing of medical information[84]. Wearable sensors integrated into larger systems connecting individuals, emergency responders, and healthcare providers cause medical

information to become distributed over networks instead of centralized. In this new landscape, it is essential that user privacy is protected using encryption schemes and personal identifiers. Further, access to sensor data must be regulated to prevent tampering by malicious parties that could lead to false diagnoses or compromised treatment recommendations[1,2]. As advances in sweat sensing and other wearable technology contribute to the wider digitization of information in the 'Internet of Things' (IoT), parallel efforts become necessary to ensure safe storage and handling of data.

1.5 Data integrity for meaningful sweat analysis

While ensuring stability and sensitivity along with the other discussed attributes can produce a good sensor, this does not guarantee meaningful sensor readings for on-body measurement. Contamination from skin and sweat evaporation can corrupt the concentrations of analytes in sweat such that sensor measurements, though accurate, now reflect post-secretion changes in sweat composition. Similarly, sweat rate effects can impact final analyte concentrations such that they are no longer solely reflective of profiles deeper in the body. We touched upon these data integrity issues earlier, and we will now discuss two key approaches to tackling them: utilizing microfluidics and multiplexed sensing.

Integrating microfluidics into wearable sweat sensors overcomes many issues diminishing data integrity. Once sweat enters the microfluidic channels, it is isolated from the skin surface, preventing continual leeching of chemicals from skin into sweat. Channels can be designed to direct old sweat away from the sensor and allow new sweat to travel in. This ensures as real-time readings as possible instead of producing rolling averages of analyte concentrations. Finally, microfluidics can encase sweat as it travels over the sensing electrodes, minimizing evaporation. Several of the sweat sensing platforms discussed previously already utilize microfluidics, but they must become ubiquitous in future sensor development[8,16,26].

Measuring multiple analytes simultaneously can help elucidate whether changes in sensor signals stem from true changes in analyte concentrations or from sweat rate effects. For example, an increase in Na^+ levels could indicate physiological changes in the body or an increase in sweat rate. Parallel sensing of an analyte like K^+ that doesn't depend strongly on sweat rate, or direct monitoring of sweat rate itself, can help distinguish between these potential causes[16,18]. Other changes could stem from dependencies of the sensors themselves instead of the analytes. For example, the activity of enzymes entrapped in sensing layers can change with pH. Consequently, a change in a glucose sensor signal may stem from a change in sweat pH rather than fluctuations in secreted glucose. Multiplexed sensing of glucose and pH can resolve this issue. Skin temperature can also impact sensor signals, and should be monitored simultaneously with sweat analytes to allow accurate calibrations. Further questions of data integrity arise when sensors demonstrate cross-reactivity with more than one analyte rather than being perfectly selective. For example, even after utilizing ionophores, Ca^{2+} and K^+ sensors still respond to changes in Na^+

content[6,60]. Multiplexed sensing provides a solution to this problem as well – the responses of a group of semi-selective sensors can be assessed collectively to generate a pattern that is indicative
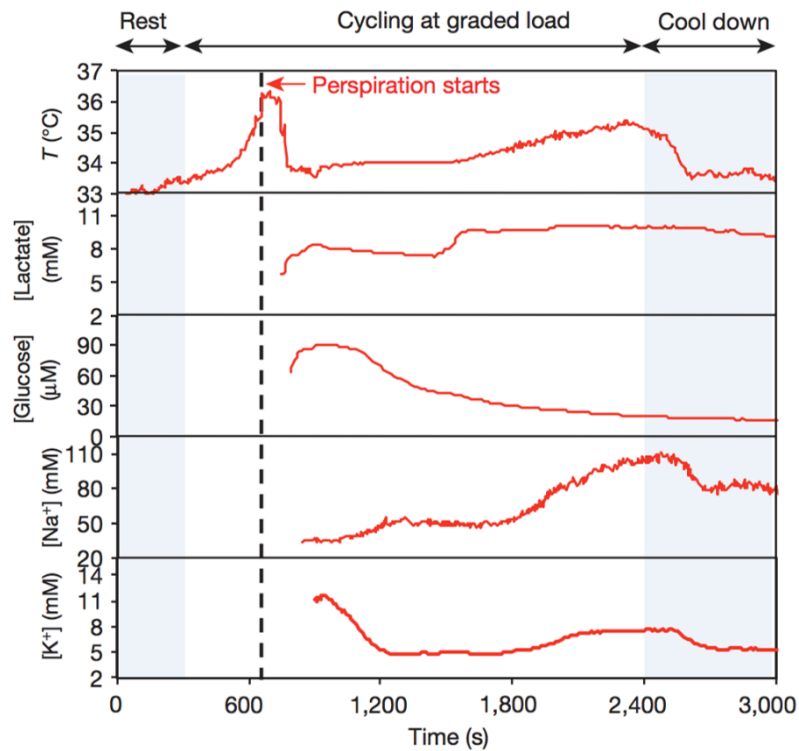

Figure 5: Multiplexed Sensing of Sweat Analytes. Real-time monitoring of a panel of biomarkers secreted in sweat during constant load exercise[6].

of a certain analyte and its concentration, even if each sensor alone cannot uniquely transduce this information[85]. Overall, multiplexed sensing can help isolate interdependencies between analytes, sensors, and environmental factors to ensure that measured concentrations are maximally indicative of deeper physiology. As an example, **Fig. 5** shows multiplexed sensing of a panel of sweat biomarkers during exercise[6].

1.6 The future of sweat sensing

Rapidly growing interest in the physiological information contained in sweat has led to sensor development for analytes including ions, metabolites, and heavy metals. Many of these analytes are low-hanging fruit, easy to detect because they are present in relative high µM or mM concentrations and can be measured with simple yet selective schemes. However, sweat contains a wealth of other constituents present in trace amounts much harder to detect, including hormones, proteins, and peptides. These complex molecules serve regulatory or signaling functions in the body, and studies with sweat patches have suggested that their concentrations in sweat may correlate directly with blood[86]. Detecting these molecules in sweat could thus provide deeper physiological insight into homeostasis mechanisms and the body's overall state of health.

Neuropeptide Y (NPY) is a promising candidate for future detection. This peptide is involved in the body's stress response and has been found in greater concentration in the sweat of patients with depression compared to healthy cohorts[87]. Sweat-based monitoring of NPY could make mental health more quantifiable and transparent. Cytokines are another class of proteins present in sweat[86]. Interleukin 6 is a cytokine involved in the body's immune system response to injury or infection, and could provide insight into the body's reaction to physical trauma. More comprehensively, analysis of entire protein panels has revealed differences in the composition of sweat from healthy versus schizophrenic patients[88]. These biomarkers and their potential applications represent some of the opportunities for sweat sensors going forward. Methods for detecting these molecules include using antibodies or aptamers for affinity-based sensing. Antibodies have historically been used for molecular recognition, but their poor stability and potential for cross-reactivity make them difficult to adapt for wearable sensing. Aptamers have emerged as an alternative to antibodies due to their higher stability, ease of synthesis, and better performance at low analyte concentrations However, it is difficult to identify selective aptamers for detection of small molecules due to limited ligand-aptamer interactions and limited functional groups[32]. Additionally, factors including pH and temperature influence 3D aptamer morphologies and degrade their ability to bind target molecules[64]. Beyond these difficulties for producing stable, high-affinity sensors, additional challenges lie in compensating for the extensive dilution of these analytes between blood and sweat. Refining measurement techniques and sensor platforms for these molecules will represent the next watershed for sweat sensing, allowing detection capabilities to be extended to a new class of physiologically relevant analytes.

As detection capabilities improve and expand towards new chemicals, it becomes important to investigate the physiological relevance of sweat for health monitoring. Understanding the mechanisms by which analytes partition into sweat could shed light on how their concentrations reflect the body's overall state, yet these processes are poorly understood for all but the simplest ions and metabolites. Instead, population studies that apply data mining techniques on large sets of sensor measurements could be used to identify correlations between sweat analytes and health status. This big data approach allows the significance of sweat analytes to be reverse-engineered from amassed data without *a priori* understanding the deeper chemical processes that govern their secretion[4]. Correlation studies can identify how sweat analyte profiles differ between healthy and afflicted physiologies, ultimately guiding new methods of non-invasive, personalized diagnostics and monitoring.

Wearable sensors combined with data mining have been previously shown to add value over conventional medical screenings, often by providing early warning of developing pathologies before traditional symptoms manifest. In one study, a team of researchers showed how physiological data from wearable sensors indicated the onset of life-threatening sepsis in premature infants[89]. Changes in infants' heart rate and respiratory rate variability were used to diagnose sepsis even before fever or high white blood cell counts were detected. In another study, an individual was monitored with wearable sensors for over a year, continuously mining data on

parameters including heart rate, body temperature, and blood oxygen content[3]. The study found that periods marked by high sensor variation from their usual baselines correlated with the subject developing health conditions including Lyme disease and viral infection. These studies
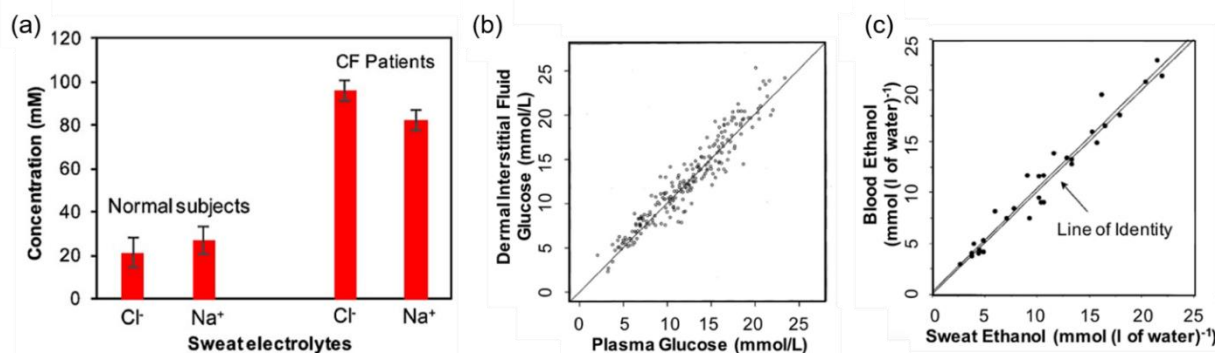

Figure 6: Correlating Non-Invasive Biomarkers with Health Status. (a) Sweat Na^+ and Cl^- levels, measured by a wearable platform with iontophoresis capabilities, are shown to differentiate normal subjects from cystic fibrosis patients[7]. **(b)** 1-to-1 correlation between blood and interstitial fluid glucose allows for non-invasive diabetes management. Reprinted from[38] with permission from Elsevier. **(c)** Sweat ethanol is shown to directly correlate with blood ethanol, underscoring the possibility of sweat-based monitoring of alcohol abuse[90]. Reused with permission from[90].

demonstrate how big data can be used to uncover actionable correlations between sensor readings and health status, even without a complete understanding of their causal relationship. Methods of fusing and interpreting large data sets include statistical methods, pattern recognition, and artificial intelligence for extracting correlations and enabling health status predictions[1,2]. In future, developing these algorithms in application-specific contexts will be critical to utilizing wearable sensors for human health. While the cases above rely on physiological signals that are one step removed from the chemical processes that govern our body, probing molecules directly has the potential to uncover deeper insights and correlations. Population studies on sweat analytes can thus be a powerful step towards enabling new forms of personalized healthcare.

For certain pathologies, sweat analytes correlate directly with health status (**Fig. 6**). Sweat Cl^- concentration, for example, can be compared against a universal threshold to diagnose cystic fibrosis[7]. In other cases, analytes accessed non-invasively through iontophoresis or reverse iontophoresis individually correlate with blood levels. If blood-based thresholds are typically used for screening in these cases, analogous sweat thresholds can be determined for non-invasive diagnosis. This type of correlation has been demonstrated between sweat ethanol and blood alcohol content (BAC)[19,90]. In most other cases, however, correlations between sweat levels and health status are not as straightforward. Several sweat markers may need to be considered collectively in order to be indicative of health conditions, and even then, they may not uncover universal thresholds for diagnosis. Instead, personalized baselines of relevant analytes will need to be identified for each individual through continuous sweat measurements. Deviations from this

baseline could then provide individual-specific indications of developing health conditions. This approach is relevant to athletic monitoring as well – preliminary work on dehydration during long-term exercise suggests that sudden changes in sweat Na$^+$ from a personalized baseline could correlate with the onset of dehydration[6]. For such applications, big data techniques are especially important in order to extract subtle and possibly surprising patterns from large amounts of continuous, multiplexed measurements. These complex correlation studies remain a key challenge for establishing the wider utility of sweat sensing for human health.

Subsequent chapters of this thesis will present platforms and approaches that pave the way for better understanding and utilizing the physiological significance of sweat. These chapters will focus on device aspects as well as the deployment of sensors in small-scale subject studies. Platforms will be introduced that use integrated microfluidics to make accurate, dynamic, and multiplexed measurements of sweat rate and composition, critical for uncovering correlations. Mass production approaches will be presented for high-throughput and repeatable sensor fabrication towards enabling subject studies with large sensor volume demands. Sensors for accessing sweat at rest, without disruptive, deliberate sweat induction, will be introduced as a way to better preserve sweat-to-blood correlations and enable routine sweat analysis during daily activities. Preliminary findings from small-scale subject studies will be presented to reveal promising application areas in which sweat might provide physiological insight, and to guide deeper investigations. Overall, these chapters will reveal multi-faceted approaches for enabling meaningful sweat sensing beyond the lab, and present avenues for future work in this field.

1.7 References

1. Zheng, Y. L. *et al.* Unobtrusive Sensing and Wearable Devices for Health Informatics. *IEEE Trans. Biomed. Eng.* **61,** 1538–1554 (2014).
2. Andreu-Perez, J., Poon, C. C. Y., Merrifield, R. D., Wong, S. T. C. & Yang, G. Z. Big Data for Health. *IEEE J. Biomed. Health Inform.* **19,** 1193–1208 (2015).
3. Li, X. *et al.* Digital Health: Tracking Physiomes and Activity Using Wearable Biosensors Reveals Useful Health-Related Information. *PLOS Biol.* **15,** e2001402 (2017).
4. Bottles, K., Begoli, E. & Worley, B. Understanding the Pros and Cons of Big Data Analytics. *Physician Executive* **40**, 6-12 (2014).
5. Bandodkar, A. J. & Wang, J. Non-invasive wearable electrochemical sensors: a review. *Trends Biotechnol.* **32,** 363–371 (2014).
6. Gao, W. *et al.* Fully integrated wearable sensor arrays for multiplexed *in situ* perspiration analysis. *Nature* **529,** 509-514 (2016).
7. Emaminejad, S. *et al.* Autonomous sweat extraction and analysis applied to cystic fibrosis and glucose monitoring using a fully integrated wearable platform. *Proc. Natl. Acad. Sci.* **114,** 4625–4630 (2017).
8. Koh, A. *et al.* A soft, wearable microfluidic device for the capture, storage, and colorimetric sensing of sweat. *Sci. Transl. Med.* **8,** 366ra165-366ra165 (2016).
9. Rose, D. P. *et al.* Adhesive RFID Sensor Patch for Monitoring of Sweat Electrolytes. *IEEE Trans. Biomed. Eng.* **62,** 1457–1465 (2015).

10.   Sonner, Z., Wilder, E., Gaillard, T., Kasting, G. & Heikenfeld, J. Integrated sudomotor axon reflex sweat stimulation for continuous sweat analyte analysis with individuals at rest. *Lab. Chip* **17,** 2550–2560 (2017).

11.   Bandodkar, A. J. *et al.* Tattoo-Based Noninvasive Glucose Monitoring: A Proof-of-Concept Study. *Anal. Chem.* **87**, 394–398 (2014).

12.   Jia, W. *et al.* Electrochemical Tattoo Biosensors for Real-Time Noninvasive Lactate Monitoring in Human Perspiration. *Anal. Chem.* **85**, 6553–6560 (2013).

13.   Kim, J. *et al.* Wearable salivary uric acid mouthguard biosensor with integrated wireless electronics. *Biosens. Bioelectron.* **74,** 1061 (2015).

14.   Huang, X. *et al.* Stretchable, Wireless Sensors and Functional Substrates for Epidermal Characterization of Sweat. *Small* **10,** 3083–3090 (2014).

15.   Lee, H. *et al.* Wearable/disposable sweat-based glucose monitoring device with multistage transdermal drug delivery module. *Sci. Adv.* **3,** e1601314 (2017).

16.   Heikenfeld, J. Non-invasive Analyte Access and Sensing through Eccrine Sweat: Challenges and Outlook circa 2016. *Electroanalysis* **28,** 1242–1249 (2016).

17.   Heikenfeld, J. Bioanalytical devices: Technological leap for sweat sensing. *Nature* **529,** 475-476 (2016).

18.   Sonner, Z. *et al.* The microfluidics of the eccrine sweat gland, including biomarker partitioning, transport, and biosensing implications. *Biomicrofluidics* **9,** 031301 (2015).

19.   Kim, J. *et al.* Noninvasive Alcohol Monitoring Using a Wearable Tattoo-Based Iontophoretic-Biosensing System. *ACS Sens.* **1,** 1011–1019 (2016).

20.   Gao, W. *et al.* Wearable Microsensor Array for Multiplexed Heavy Metal Monitoring of Body Fluids. *ACS Sens.* **1,** 866–874 (2016).

21.   N, D. G. N. and F. The current status of sweat testing for drugs of abuse: a review. *Curr Med Chem.* **20,** 545-61 (2013).

22.   Kidwell, DA, Holland, JC & Athanaselis, S. Testing for drugs of abuse in saliva and sweat. *J. Chromatogr. B. Biomed. Sci. App.* **713,** 111–135 (1998).

23.   Desax, M.-C. *et al.* Nanoduct® sweat testing for rapid diagnosis in newborns, infants and children with cystic fibrosis. *Eur. J. Pediatr.* **167,** 299–304 (2008).

24.   Houglum, J.E., Harrelson, G. & Seefeldt, T. *Principles of Pharmacology for Athletic Trainers*. Ch. 17 (Slack Inc., 2016).

25.   Gao, W. *et al.* Wearable sweat biosensors. in *2016 IEEE International Electron Devices Meeting (IEDM)* 6.6.1-6.6.4 (2016).

26.   Choi, J., Kang, D., Han, S., Kim, S. B. & Rogers, J. A. Thin, Soft, Skin-Mounted Microfluidic Networks with Capillary Bursting Valves for Chrono-Sampling of Sweat. *Adv. Healthc. Mater.* **6,** (2017).

27.   Daniels, J. S. & Pourmand, N. Label-Free Impedance Biosensors: Opportunities and Challenges. *Electroanalysis* **19,** 1239–1257 (2007).

28.   Singh, M., Truong, J., Reeves, W. B. & Hahm, J. Emerging Cytokine Biosensors with Optical Detection Modalities and Nanomaterial-Enabled Signal Enhancement. *Sensors* **17,** (2017).

29.   Morris, D. *et al.* Bio-sensing textile based patch with integrated optical detection system for sweat monitoring. *Sens. Actuators B Chem.* **139,** 231–236 (2009).

30.   R. Corrie, S., W. Coffey, J., Islam, J., A. Markey, K. & F. Kendall, M. A. Blood, sweat, and tears: developing clinically relevant protein biosensors for integrated body fluid analysis. *Analyst* **140,** 4350–4364 (2015).

31. Uzun, L. & Turner, AP. Molecularly-imprinted polymer sensors: realising their potential. *Biosens. Bioelectron.* **76,** 131–144 (2016).

32. Pfeiffer, F. & Mayer, G. Selection and Biosensor Application of Aptamers for Small Molecules. *Front. Chem.* **4,** (2016).

33. Prausnitz, M. R. The effects of electric current applied to skin: A review for transdermal drug delivery. *Adv. Drug Deliv. Rev.* **18,** 395–425 (1996).

34. Garg, S. K. *et al.* Correlation of fingerstick blood glucose measurements with GlucoWatch biographer glucose results in young subjects with type 1 diabetes. *Diabetes Care* **22,** 1708–1714 (1999).

35. Tierney, M. J. *et al.* The GlucoWatch® biographer: a frequent, automatic and noninvasive glucose monitor. *Ann. Med.* **32,** 632-641 (2010).

36. Tierney, M. J. *et al.* Clinical evaluation of the GlucoWatch® biographer: a continual, non-invasive glucose monitor for patients with diabetes. *Biosens. Bioelectron.* **16,** 621–629 (2001).

37. Tierney, M. J. *et al.* Design of a Biosensor for Continual, Transdermal Glucose Monitoring. *Clin. Chem.* **45,** 1681–1683 (1999).

38. Bantle, J. P. & Thomas, W. Glucose measurement in patients with diabetes mellitus with dermal interstitial fluid. *J. Lab. Clin. Med.* **130,** 436–441 (1997).

39. Nemiroski, A. *et al.* Universal mobile electrochemical detector designed for use in resource-limited applications. *Proc. Natl. Acad. Sci.* **111,** 11984–11989 (2014).

40. Windmiller, J. R. & Wang, J. Wearable Electrochemical Sensors and Biosensors: A Review. *Electroanalysis* **25,** 29–46 (2013).

41. Zeng, W. *et al.* Fiber-Based Wearable Electronics: A Review of Materials, Fabrication, Devices, and Applications. *Adv. Mater.* **26,** 5310–5336 (2014).

42. Grau, G. *et al.* Gravure-printed electronics: recent progress in tooling development, understanding of printing physics, and realization of printed devices. *Flex. Print. Electron.* **1,** 023002 (2016).

43. Khan, Y. *et al.* Flexible Hybrid Electronics: Direct Interfacing of Soft and Hard Electronics for Wearable Health Monitoring. *Adv. Funct. Mater.* **26,** 8764–8775 (2016).

44. Schazmann, B. *et al.* A wearable electrochemical sensor for the real-time measurement of sweat sodium concentration. *Anal. Methods* **2,** 342–348 (2010).

45. Anastasova, S. *et al.* A wearable multisensing patch for continuous sweat monitoring. *Biosens. Bioelectron.* **93,** 139–145 (2017).

46. Abellán-Llobregat, A. *et al.* A stretchable and screen-printed electrochemical sensor for glucose determination in human perspiration. *Biosens. Bioelectron.* **91,** 885–891 (2017).

47. Ray Windmiller, J. *et al.* Electrochemical sensing based on printable temporary transfer tattoos. *Chem. Commun.* **48,** 6794–6796 (2012).

48. Kim, J. *et al.* Wearable temporary tattoo sensor for real-time trace metal monitoring in human sweat. *Electrochem. Commun.* **51,** 41–45 (2015).

49. Munje, R. D., Muthukumar, S., Selvam, A. P. & Prasad, S. Flexible nanoporous tunable electrical double layer biosensors for sweat diagnostics. *Sci. Rep.* **5,** 14586 (2015).

50. Kinnamon, D., Ghanta, R., Lin, K.-C., Muthukumar, S. & Prasad, S. Portable biosensor for monitoring cortisol in low-volume perspired human sweat. *Sci. Rep.* **7,** 13312 (2017).

51. Kilic, T., Brunner, V., Audoly, L. & Carrara, S. Smart e-Patch for drugs monitoring in schizophrenia. in *2016 IEEE International Conference on Electronics, Circuits and Systems (ICECS)* 57–60 (2016).

52.   Wang, J. Study of Electrode Reactions and Interfacial Properties. in *Analytical Electrochemistry* 29–66 (John Wiley & Sons, Inc., 2006).

53.   Amos Mugweru, Becky L. Clark & Michael V. Pishko. Electrochemical Sensor Array for Glucose Monitoring Fabricated by Rapid Immobilization of Active Glucose Oxidase within Photochemically Polymerized Hydrogels. *J. Diabetes Sci. Technol.* **1,** 366–371 (2007).

54.   Wang, J. Controlled-Potential Techniques. in *Analytical Electrochemistry* 67–114 (John Wiley & Sons, Inc., 2006).

55.   Yoshizumi, J., Kumamoto, S., Nakamura, M. & Yamana, K. Target -induced strand release (TISR) from aptamer – DNA duplex: A general strategy for electronic detection of biomolecules ranging from a small molecule to a large protein. *Analyst* **133,** 323–325 (2008).

56.   Liu, X., Duckworth, P. A. & Wong, D. K. Y. Square wave voltammetry versus electrochemical impedance spectroscopy as a rapid detection technique at electrochemical immunosensors. *Biosens. Bioelectron.* **25,** 1467–1473 (2010).

57.   Current-polarized ion-selective membranes: The influence of plasticizer and lipophilic background electrolyte on concentration profiles, resistance, and voltage transients. *Sens. Actuators B Chem.* **136,** 410–418 (2009).

58.   Telting-Diaz, M. & Bakker, E. Effect of Lipophilic Ion-Exchanger Leaching on the Detection Limit of Carrier-Based Ion-Selective Electrodes. *Anal. Chem.* **73,** 5582–5589 (2001).

59.   Patterson, M. J., Galloway, S. D. R. & Nimmo, M. A. Variations in regional sweat composition in normal human males. *Experimental Physiology* **85,** 869-75 (2000).

60.   Nyein, H. Y. Y. *et al.* A Wearable Electrochemical Platform for Noninvasive Simultaneous Monitoring of Ca^{2+} and pH. *ACS Nano* **10,** 7216–7224 (2016).

61.   Njagi, J. I. & Kagwanja, S. M. The Interface in Biosensing: Improving Selectivity and Sensitivity. in *Interfaces and Interphases in Analytical Chemistry* **1062,** 225–247 (American Chemical Society, 2011).

62.   Mehrvar, M. & Abdi, M. Recent Developments, Characteristics, and Potential Applications of Electrochemical Biosensors. *Anal. Sci.* **20,** 1113–1126 (2004).

63.   Wang, J. Electrochemical Glucose Biosensors. *Chem. Rev.* **108,** 814–825 (2008).

64.   McKeague, M. & DeRosa, M. C. Challenges and Opportunities for Small Molecule Aptamer Development. *Journal of Nucleic Acids* **2012,** 748913 (2012).

65.   Bandodkar, A. J., Jeerapan, I. & Wang, J. Wearable Chemical Sensors: Present Challenges and Future Prospects. *ACS Sens.* **1,** 464–482 (2016).

66.   Burugapalli, K., Wang, N., Trzebinski, J., Song, W. & Cass, A. *Nanomaterials in Glucose Sensing*. Ch. 5 (ASME Press, 2014).

67.   Bakker, E., Bühlmann, P. & Pretsch, E. Polymer Membrane Ion-Selective Electrodes– What are the Limits? *Electroanalysis* **11,** 915–933 (1999).

68.   Grieshaber, D., MacKenzie, R., Vörös, J. & Reimhult, E. Electrochemical Biosensors - Sensor Principles and Architectures. *Sensors* **8,** 1400–1458 (2008).

69.   Ahmed, M. U., Zourob, M. & Tamiya, E. *Food Biosensors*. Ch.9 (RSC Publishing, 2016).

70.   Hurt, R. H., Monthioux, M. & Kane, A. Toxicology of carbon nanomaterials: Status, trends, and perspectives on the special issue. *Carbon* **44,** 1028–1033 (2006).

71.   Bakker, E. & Pretsch, E. Potentiometric sensors for trace-level analysis. *TrAC Trends Anal. Chem.* **24,** 199–207 (2005).

72.	Rathee, K., Dhull, V., Dhull, R. & Singh, S. Biosensors based on electrochemical lactate detection: A comprehensive review. *Biochem. Biophys. Rep.* **5,** 35–54 (2016).

73.	Zhu, C., Yang, G., Li, H., Du, D. & Lin, Y. Electrochemical Sensors and Biosensors Based on Nanomaterials and Nanostructures. *Anal. Chem.* **87,** 230–249 (2015).

74.	Fibbioli, M. *et al.* Potential Drifts of Solid-Contacted Ion-Selective Electrodes Due to Zero-Current Ion Fluxes Through the Sensor Membrane. *Electroanalysis* **12,** 1286–1292 (2000).

75.	Zhu, J., Qin, Y. & Zhang, Y. Preparation of all solid-state potentiometric ion sensors with polymer-CNT composites. *Electrochem. Commun.* **11,** 1684–1687 (2009).

76.	Mir, M., Lugo, R., Tahirbegi, I. B. & Samitier, J. Miniaturizable Ion-Selective Arrays Based on Highly Stable Polymer Membranes for Biomedical Applications. *Sensors* **14,** 11844–11854 (2014).

77.	Rocchitta, G. *et al.* Enzyme Biosensors for Biomedical Applications: Strategies for Safeguarding Analytical Performances in Biological Fluids. *Sensors* **16,** 780 (2016).

78.	Cosnier, S. Biomolecule immobilization on electrode surfaces by entrapment or attachment to electrochemically polymerized films. A review. *Biosens. Bioelectron.* **14,** 443–456 (1999).

79.	Zhang, M., Smith, A. & Gorski, W. Carbon Nanotube−Chitosan System for Electrochemical Sensing Based on Dehydrogenase Enzymes. *Anal. Chem.* **76,** 5045–5050 (2004).

80.	Gomez, C., Oller, J. & Paradells, J. Overview and Evaluation of Bluetooth Low Energy: An Emerging Low-Power Wireless Technology. *Sensors* **12,** 11734–11753 (2012).

81.	Burnette, D. W. *et al.* Intelligent wireless communications for continuous analyte monitoring. (2016).

82.	Yilmaz, T., Foster, R. & Hao, Y. Detecting Vital Signs with Wearable Wireless Sensors. *Sensors* **10,** 10837–10862 (2010).

83.	Bahk J., Fang, H., Yazawa, K. and Shakouri A. Flexible thermoelectric materials and device optimization for wearable energy harvesting. *J. Mater. Chem. C* **3,** 10362-374 (2015).

84.	Thierer, A. The Internet of Things and Wearable Technology: Addressing Privacy and Security Concerns without Derailing Innovation. *RICH. J.L. & TECH.* **21,** (2015)

85.	Albert, K. J. *et al.* Cross-Reactive Chemical Sensor Arrays. *Chem. Rev.* **100,** 2595–2626 (2000).

86.	Marques-Deak, A. *et al.* Measurement of cytokines in sweat patches and plasma in healthy women: Validation in a controlled study. *J. Immunol. Methods* **315,** 99–109 (2006).

87.	Cizza, G. *et al.* Elevated Neuroimmune Biomarkers in Sweat Patches and Plasma of Premenopausal Women with Major Depressive Disorder in Remission: The POWER Study. *Biol. Psychiatry* **64,** 907–911 (2008).

88.	Raiszadeh, M. M. *et al.* A Proteomic Analysis of Eccrine Sweat: Implications for the Discovery of Schizophrenia Biomarker Proteins. *J. Proteome Res.* **11,** 2127 (2012).

89.	McGregor, C., Catley, C. & James, A. Variability analysis with analytics applied to physiological data streams from the neonatal intensive care unit. in *2012 25th IEEE International Symposium on Computer-Based Medical Systems (CBMS)* 1–5 (2012).

90.	Buono, M. J. Sweat ethanol concentrations are highly correlated with co-existing blood values in humans. *Exp. Physiol.* **84,** 401–404 (1999).

91.	Guinovart, T., J. Bandodkar, A., R. Windmiller, J., J. Andrade, F. & Wang, J. A potentiometric tattoo sensor for monitoring ammonium in sweat. *Analyst* **138,** 7031–7038 (2013).

92. Mickelsen, O. & Keys, A. The composition of sweat, with special reference to vitamins. *J. Biol. Chem.* **149,** 479–490 (1943).

93. Shields, J. B., Johnson, B. C., Hamilton, T. S. & Mitchell, H. H. The excretion of ascorbic acid and dehydroascorbic acid in sweat and urine under different environmental conditions. *J. Biol. Chem.* **161,** 351–356 (1945).

94. Wang, J. Fundamental Concepts. in *Analytical Electrochemistry* 1-28 (John Wiley & Sons, Inc., 2006).

95. Lisdat, F. & Schäfer, D. The use of electrochemical impedance spectroscopy for biosensing. *Anal. Bioanal. Chem.* **391,** 1555 (2008).

1.8 Appendix

1.8.1 Table 1: Analytes in Sweat and Select Detection Methods

Analyte	Concentration in sweat	Recognition element	Sensing modality	References
Na^+	10 -100 mM	Na ionophore	Potentiometry	6,7,44,45,59
Cl^-	10 -100 mM	Ag/AgCl		7,59
K^+	1-18.5 mM	K ionophore		6,59
Ca^{2+}	0.41-12.4 mM	Ca ionophore		59,60
pH	3 - 8	polyaniline		45,60
NH_4^+	0.1 - 1 mM	Ammonium ionophore		91
Glucose	10 - 200 μM	Glucose oxidase	Chronoamperometry	6,7,46
Lactate	5 - 20 mM	Lactate oxidase		45
Ethanol	2.5 - 22.5 mM	Alcohol oxidase		18,19
Uric acid	2 - 10 mM	Carbon	Cyclic voltammetry	47
Ascorbic acid	10 - 50 μM	Carbon		47,92,93
Zn^{2+}	100 - 1560 μg/l	Bi	Square wave stripping voltammetry	20,48
Cd^{2+}	<100 μg/l	Bi		20
Pb^{2+}	<100 μg/l	Bi, Au		20
Cu^{2+}	100 - 1000 μg/l	Au		20
Hg^+	<100 μg/l	Au		20
Cortisol	8 - 140 ng/ml	ZnO, MoS_2	Electrochemical Impedance Spectroscopy	49,50
F17464	-	Graphite	Differential Pulse Voltammetry	51

1.8.2 Table 2: Comparison of Electrochemical Detection Methods

Method	Overview	Advantages	Disadvantages	References
Potentiometry	The potential between the sensing and reference electrode is indicative of target ion concentration.	• Simple detection scheme and signal processing • Ideal for charged species with fixed charge state • Good for relatively concentrated species in the mM range	• Because this scheme measures activity as opposed to concentration, a selective membrane layer must be developed to target specific ions • Susceptible to interference from other charges for less concentrated ions • Only applicable for sensing charged species	6, 7, 54
Chronoamperometry	A fixed potential is applied to the sensing electrode and the resulting current due to stimulated redox reactions is proportional to target analyte concentration.	• Simple detection and easy post-processing to convert current to concentration • Mediators can be employed to lower the necessary potential and thus power consumption	• For trace species below µM ranges, the Faradaic signal can decay over time to give inaccurate concentration conversions • Typically need an enzyme to provide selectivity	6, 7, 19, 94
Voltammetry	A voltage scan is conducted between the sensing and reference electrode, and the resulting current features are extracted to determine concentration.	• Because different species have unique redox potentials, a voltage scan on the same two electrodes can be used to extract information on several analytes at once • There are a variety of sub-techniques to choose from to optimize signal-to-noise ratios • Can be coupled with pre-concentration techniques for detection of trace molecules, achieving higher limits of detection compared to chronoamperometry	• Voltage scans can trigger background reactions that occlude or interfere with the desired signal • Compared to chronoamperometry, this technique requires more complex post-processing to extract and identify peaks corresponding to the desired analyte	20, 48, 53-56, 94

Electrochemical Impedance Spectroscopy	Using an applied sinusoidal voltage, the impedance of the transducing surface is obtained to reflect the amount of binding of target species on the sensor surface, indicating concentration.	• Does not require electrochemically inactive species to be coupled to redox labels before detection, as selective binding of the target on the sensor surface intrinsically produces an impedance change	• Requires longer analysis times with more complex post-processing than voltammetric techniques • Sensitivity towards direct binding detection can be low, requiring amplification techniques to be incorporated	50, 56, 95

Chapter 2: Roll-to-roll gravure printed electrochemical sensors for wearable and medical devices

The following chapter has been previously published in a similar format, and is reprinted and/or adapted with permission from the following work:

M. Bariya[*], Z. Shahpar[*], H. Park, J. Sun, Y. Jung, W. Gao, H. Y. Y. Nyein, T. S. Liaw[1], L.-C. Tai, Q. P. Ngo, M. Chao, Y. Zhao, M. Hettick, G. Cho, A. Javey. Roll-to-Roll Gravure Printed Electrochemical Sensors for Wearable and Medical Devices. *ACS Nano,* **2018**, *12* (7), 6978-6987.

[*]These authors contributed equally.

2.1 Introduction

Wearable biosensors that can probe the body's physiological state at molecular levels have flourished in recent years and show great promise for enabling personalized, point-of-care health and fitness monitoring.[1–13] In particular, advancements in wearable electrochemical sensors have made it possible to non-invasively detect a variety of species including ions, metabolites, acids, heavy metals, and alcohols in biofluids including sweat, saliva, tears, and urine.[4,10,14] Some of the most successful platforms utilize hybrid electronics, combining flexible sensing components that can conformally interface to the body with the high performance and low power advantages of traditional silicon ICs for signal conditioning and transmission.[1–3,5,7,13, 32, 33] For many applications in medical screening or athletic monitoring, it is convenient for the sensing component to be disposable after one-time, on-body use. In this case, sensors of the same type must have consistent performance to ensure that for each new sensing component inserted into the device, minimal calibration is needed to accurately translate the sensor signal into meaningful concentration readings. This minimizes the overhead associated with sensor use, an important practical consideration for promoting wearable prototypes beyond a research setting. Developing high throughput, cost effective methods of fabricating sensing components with high uniformity is therefore critical for the commercial viability of wearable electrochemical devices.

The additive nature and high process speeds of roll-to-roll (R2R) printing technologies offer advantages over traditional methods like photolithography for high throughput fabrication of electronic components on flexible substrates. In fact, printing of conductive layers on skin-conformal materials has shown increasing promise and application for wearable electronics.[34-37] Of the various available printing techniques, R2R gravure printing shows particular utility as it is intrinsically robust and large-area compatible, making it well suited for industrial-scale production of inexpensive components or devices.[15,16] Further, the simple printing mechanics of R2R gravure allows faster printing speeds with superior resolution and consistency over screen printing, offset printing, or flexography.[15] For these reasons, R2R gravure has previously been developed to print flexible electronic devices including thin film transistors, wireless cyclic voltammetry tags, and a

carbon nanotube-based active matrix for tactile sensors, but has been underutilized in the context of recent advancements in wearable electrochemical biosensors.[17–20]

Here we present R2R gravure printed electrodes that can be functionalized into sensors for diverse electrochemical sensing applications (**Fig. 1**). The electrode arrays realize a canonical 3-electrode system comprising of working, reference, and counter electrodes (**Fig. 2**), and can be applied towards detecting ions, metabolites, heavy metals, and other small molecules. Large scale, high throughput fabrication on up to 150 meters of flexible substrate makes these electrodes feasible as inexpensive, disposable test strips for medical diagnostics or screening. They are also designed to be compatible with previously demonstrated platforms for *in situ* sweat monitoring, allowing them to be used in wearable sensing applications including continuous tracking of physiological indicators during exercise.[1] The printed electrodes are inert, flexible, and robust under the mechanical strains that accompany on-body use, with consistent electrochemical function that is critical to enabling reliable extraction of physiological data.
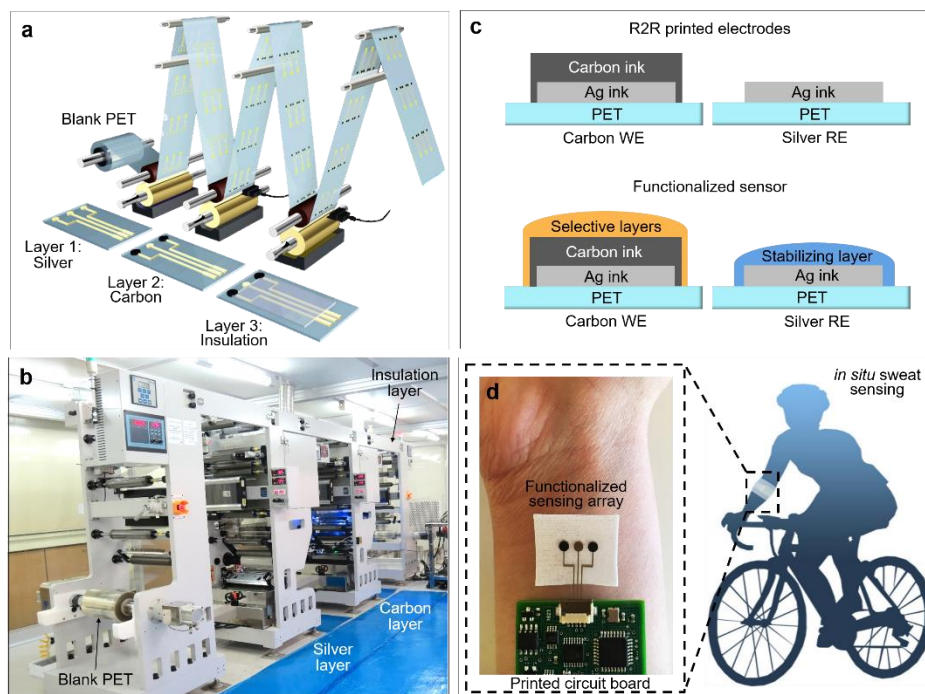
Figure 1. a) Roll-to-roll gravure printing of biocompatible electrode arrays on flexible PET substrate allows high-throughput, low-cost production of sensing electrodes that can be fabricated with controllable size and density. To print electrode arrays, 3 layers of ink are deposited including silver, carbon, and insulation layers. b) Image of the R2R gravure printing system with modular units for each layer labeled. c) Cross-section schematics of the gravure printed carbon and silver electrodes after printing and then after functionalization. Membranes to selectively target analytes are deposited over the working electrode (WE), while the silver electrode can also be modified to achieve a stable reference (RE). d) Gravure printed electrodes can be functionalized into sensors for in situ sensing applications such as continuous, real-time monitoring of analyte profiles in sweat. Sensors can be integrated with custom printed circuit boards for on-site signal processing and transmission, and the whole device worn as a 'smart' wristband during exercise for easy access to sweat.
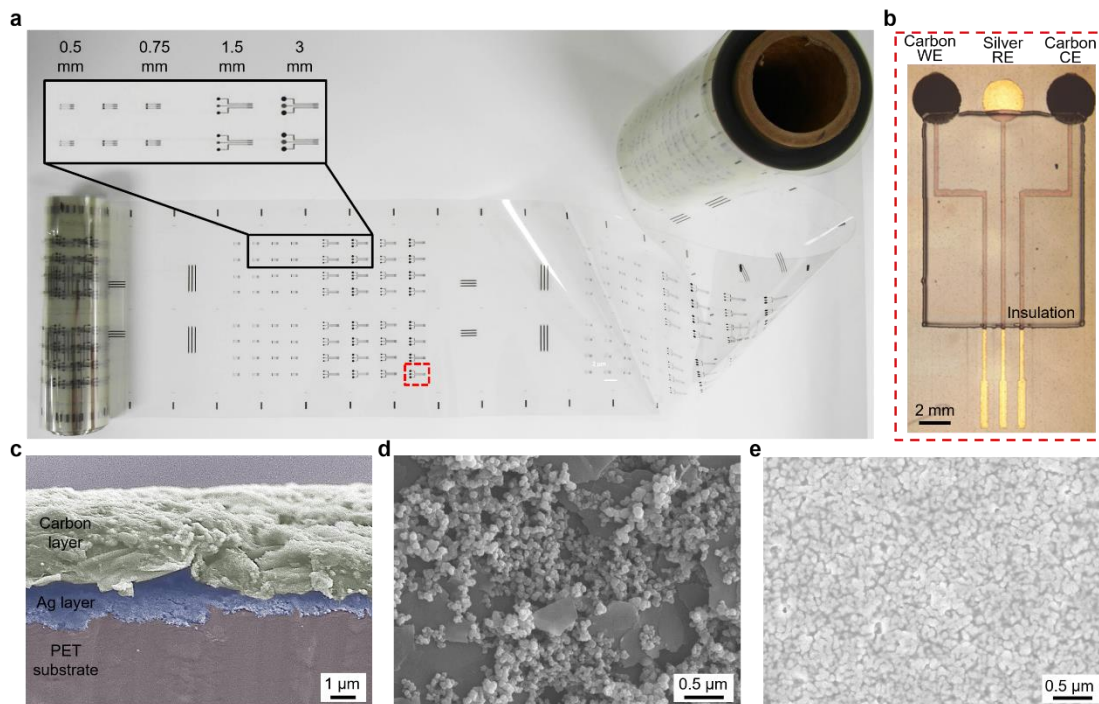
Figure 2. a) Roll-to-roll gravure printed electrodes on a 150-meter roll of PET substrate, with inset showing electrodes ranging from 3 mm down to 0.5 mm in diameter. Electrode array outlined in red is magnified in the subsequent panel. b) Optical micrograph of an array with 3 mm-diameter electrodes showing carbon working electrode, silver reference electrode, carbon counter electrode, and insulation layer. c) False color SEM of the carbon working electrode cross-section shows the hierarchical arrangement of carbon ink (colored yellow) over silver ink (colored blue) on PET substrate. Slight distortion of layer edges is an artefact of cutting for cross-section exposure. d) SEM of carbon electrode surface, and e) SEM of silver electrode surface show nanostructured ink components.

Special ink formulation is required to achieve printability under the physical constraints of R2R gravure. An important consequence is that relatively thin layers of ink (up to around 10 µm) are deposited compared to screen printing (up to 100 µm), creating more resistive features.[21] While screen printing allows a thick carbon layer alone to create conductive and inert electrodes, the thin carbon layer deposited by R2R gravure is inadequate. To address this problem, we design a bilayer working electrode morphology comprising of an underlying silver ink layer to impart conductivity, passivated by an upper carbon layer to achieve an electrochemically inert surface for detection of chemicals or redox processes. Silver ink alone is used for the reference electrode, while an insulating polyethylene resin-based ink is developed to sheathe the exposed electrode wires and prevent crosstalk or shorting in aqueous environments. This modified electrode architecture bridges the gap between requirements for stable electrochemical function and those for good printability using R2R gravure.

We design electrodes with millimeter-scale dimensions to satisfy three criteria: user comfort, sufficient biofluid access, and compatibility with the R2R gravure system. Millimeter-scale sensors are small enough to be unobtrusive when worn, yet large enough to effectively access sites of biofluid secretion such as sweat glands. On the forehead or arms, sweat gland densities are typically around 1.5 glands/mm^2 and generate several tens of nL/min/gland during exercise.[22] A 3 mm-diameter sensor could thus expect to access a couple μL of fresh sweat every few minutes, representing sufficient fluid volume for stable and near real-time readings. For these reasons and the fact that R2R gravure allows excellent pattern fidelity and throughput for printing millimeter-sized features, we design and evaluate electrodes that are 3 mm, 1.5 mm, and 0.75 mm in diameter with applications including perspiration monitoring in mind.[15] We then select the 1.5 mm electrode for more comprehensive studies of device performance variability.

2.2 Printed electrode surface treatment and characterization

We tailor ink rheology to combine printability requirements with mechanical and electrochemical robustness. Surface tension, viscosity, and wetting characteristics are considered along with other printing parameters to achieve layers with minimal defects or pinholes (**Table 2**). Using SEM and profilometer measurements, we establish that the printed silver ink layer is on average 250 nm thick with surface roughness of 20 nm. The carbon layer is 1.3 µm thick with roughness of 0.5 µm, and the insulation layer is 1.5 µm thick with roughness under 10 nm. The silver layer dominates the electrodes' electrical conductivity, and in final printed form has resistivity of 1.8 x 10^{-4} Ω·cm, comparable to that of other conductive silver inks used for gravure printing.[23]

The performance of solid-state electrochemical electrodes is highly dependent on the surface properties and state of the active electrode area. Pretreatment steps including thermal and electrochemical procedures are common for activating carbon-based electrodes by removing impurities from the electrode surface and increasing surface sensitivity to redox events.[24] To activate the gravure printed electrode arrays before measurement, we employ an optimized sequence of pretreatments including annealing at 160 °C for 1 hour before electrochemically cleaning via cyclic voltammetry (CV) in dilute hydrochloric acid. To investigate how each of these procedures impacts the electrode surface composition, we conduct XPS core level measurements using a monochromatic Al source on representative samples halted at different stages in the pretreatment process. In parallel, we explore these samples' electrochemical sensitivity to the $[Fe(CN_6)]^{4-}/[Fe(CN_6)]^{3-}$ redox couple. **Fig. S1** in the Appendix of this chapter summarizes these results to demonstrate the effects of pretreatment on the electrodes' surface composition and electrochemical performance. **Fig. S1 (a)-(c)** reveal that the sensitivity with which the electrodes can relay redox events is increasingly enhanced over the pretreatment procedures, as indicated by the greater definition of the $[Fe(CN_6)]^{4-}/[Fe(CN_6)]^{3-}$ oxidation and reduction peaks during CV measurements. Changes in the carbon electrode surface composition during pretreatment include an increase in the ratio of carbon-carbon bonds to carbon-oxygen bonds as demonstrated by their relative C 1s subpeak areas (**Fig. S1(d)-(f)**). Compositional changes in the oxygen content of the
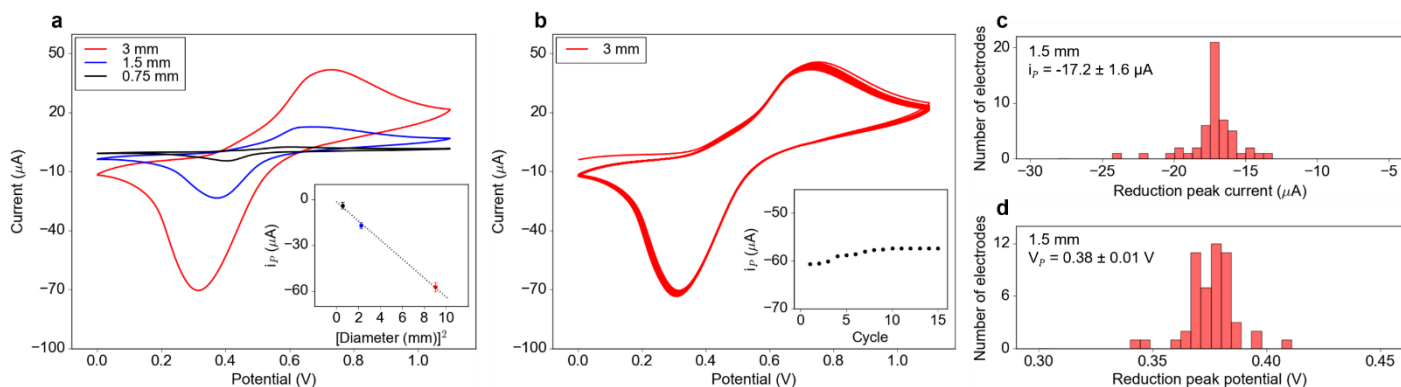
Figure 3. a) Cyclic voltammograms (CV) of 3 mm, 1.5 mm, and 0.75 mm-diameter gravure printed electrodes in 10 mM $K_3[Fe(CN)_6]$. Carbon electrodes constitute the working and counter, while the silver electrode acts as a reference. Inset: Reduction peak current i_P versus electrode diameter squared demonstrates a linear relation between the signal and electrode surface area, confirming consistent performance across electrode dimensions. CV response of 5 electrodes of each diameter are averaged for this curve, with standard deviations in i_P of 2.2, 2.0, and 3.1 µA for the 0.75 mm, 1.5 mm, and 3 mm electrodes respectively. b) Multi-cycle CV of a 3 mm electrode array demonstrates good stability, with each scan giving nearly identical current characteristics after initial stabilization. Inset: Reduction peak current is compared across cycles, with drift less than 0.2 µA between cycles. c) CV performance of a collection of 52 1.5 mm-diameter electrode arrays from throughout the printed roll are compared as histograms. Variations in (c) reduction peak current and (d) reduction peak potential are low, indicating uniform electrode quality across large swathes of the printed roll.

silver electrode surface is less dramatic, as indicated by the relative area ratios of Ag 3d subpeaks (**Fig. S1(g)-(i)**). Overall, pretreatment serves to enhance electrochemical sensitivity while adjusting surface compositions as solvents and residues from the printing process are thermally and electrochemically removed.

Across electrode dimensions, the pretreated electrode arrays demonstrate good redox kinetics with uniform performance throughout the gravure printed roll (**Fig. 3**). Cyclic voltammetry in a buffer solution of 10 mM potassium ferricyanide ($K_3[Fe(CN)_6]$) is selected to verify the electrodes' ability to evince oxidation and reduction events between the $[Fe(CN_6)]^{4-}$/$[Fe(CN_6)]^{3-}$ redox couple. Oxidation and reduction current peaks are comparable in size and scale linearly with electrode area as expected (**Fig. 3(a)**), and the CV response curve has low drift across multiple scan cycles after initial stabilization (**Fig. 3(b)**). For a more extensive analysis of electrode uniformity, the 1.5 mm-diameter electrode was chosen to compare CV results for electrodes sourced from throughout the printed roll. Specifically, we tested 52 electrode arrays from a 20 m segment of the printed roll; that is, 1 electrode array per unit of the gravure cylinder's full pattern to assess variation between printed units. Two key parameters, reduction peak potential and current, are compared as histograms for the 52 electrodes and show tight distributions with mean peak current of -17.2 ± 1.6 µA and potential of 0.38 ± 0.01 V (**Fig. 3(c)-(d)**). The low spread in
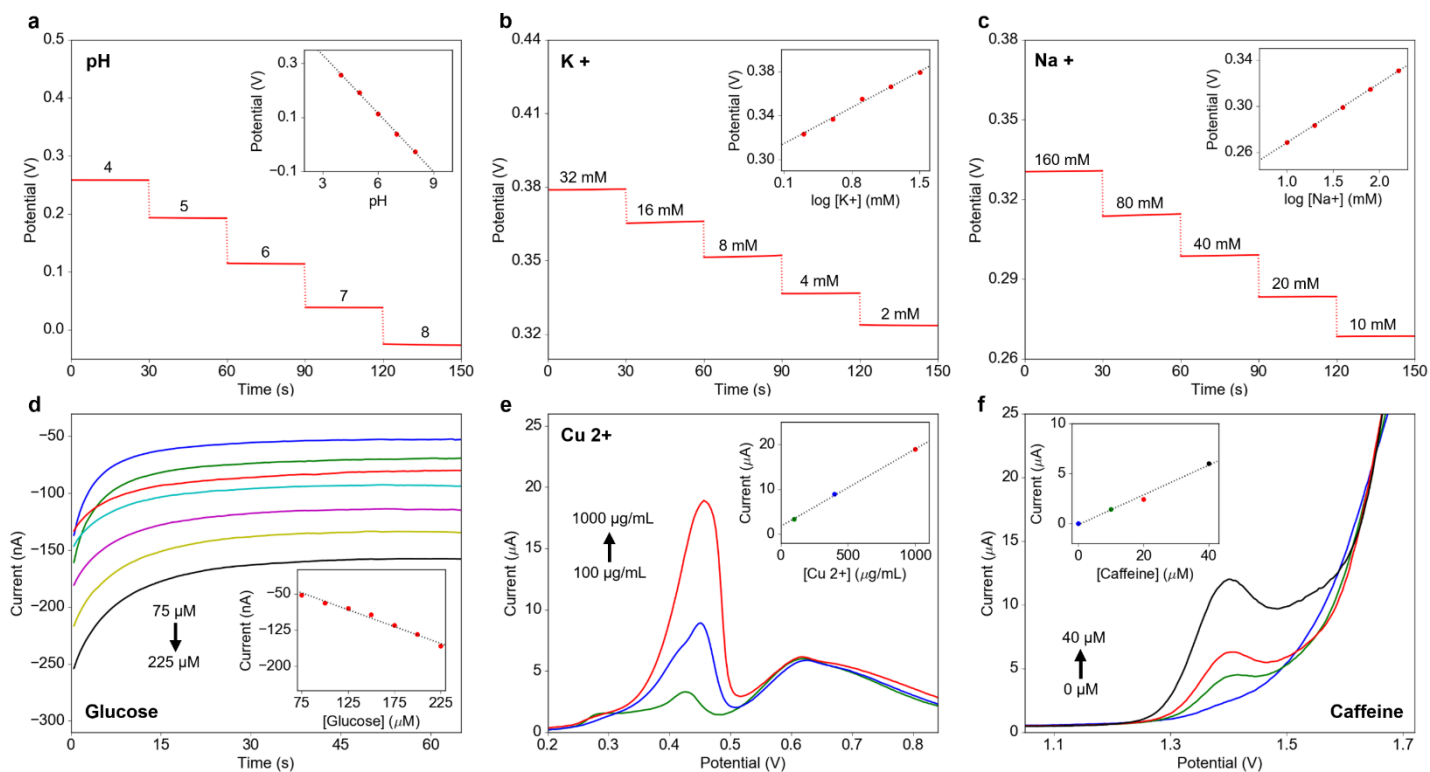
Figure 4. R2R gravure printed electrodes functionalized into different sensors are tested in varying concentrations of their target analytes; the resulting calibration curves are depicted in the insets. a) pH sensor, b) potassium (K^+) sensor, c) sodium (Na^+) sensor, d) glucose sensor, e) copper (Cu^{2+}) sensor, and f) caffeine sensor. Between concentration changes, 30 seconds of rest time are allowed for stabilization.

these parameters indicates that the electrodes have uniform properties and performance across large swathes of the printed roll.

2.3 Functionalized sensor characterization on printed electrodes

Biofluids contain a wealth of analytes including electrolytes, metabolites, heavy metals, and other small molecules. Detecting these species requires different methods of functionalizing electrodes to have selective recognition elements, as well as different electrochemical detection schemes. To demonstrate the printed electrodes' suitability for a diverse range of sensing modalities, we functionalize them into sensors for pH, potassium (K^+), sodium (Na^+), glucose, copper (Cu^{2+}), and caffeine. Ion sensing requires electrodeposition of ion-to-electron transducing films and casting of selective membrane layers to preferentially bring the target ion to the electrode surface. Potentiometric detection is employed. Glucose sensor fabrication involves deposition of a mediator layer before casting of enzyme entrapped in a hydrogel, and relies on amperometric detection. Heavy metal sensing combines pre-concentration techniques with square wave stripping voltammetry (SWSV) to detect redox peaks associated with electrodeposition of the target metal ion. Caffeine sensing uses differential pulse voltammetry (DPV) to similarly detect redox transformations of the target molecule.[25] **Fig. 4** shows the results of using these fabrication procedures and detection schemes to create and characterize sensors in buffer solutions of varying

analyte concentrations. Across physiologically relevant concentration ranges pertinent to each analyte, the sensors maintain linear calibration curves. Further, good stability during measurement in each concentration indicates high performing devices that are robust under a wide potential range and can be used for a variety of sensing applications, attesting to the quality of the underlying electrodes.

To further characterize performance of sensors fabricated on the R2R printed electrode arrays, we select one type of sensor and extensively probe its robustness under long-term and repeated use. We also assess performance uniformity across a collection of similarly fabricated sensors. For these tests, we use 1.5 mm-diameter electrodes sourced from throughout the printed roll and functionalize them into pH sensors via electro-polymerization of polyaniline on the working electrode. **Fig. 5(a)** shows long-term measurement of a representative pH sensor in a sequence of McIlvaine buffer solutions of varying pH. Near-Nernstian sensitivity of -54.2 mV/pH is preserved over the 45-minute interval with drift magnitude lower than 3.5 mV/hr. **Fig. 5(b)** demonstrates that the sensor responds consistently when cycled through buffer solutions of varying pH, with signal discrepancies of less than 1 mV between concentration cycles indicating good repeatability of results. **Fig. 5(c)** depicts a histogram of the sensitivities of 40 pH sensors fabricated on electrodes from throughout the gravure printed roll that collectively show mean sensitivity of -53.8 ± 0.9 mV/pH, while **Fig. 5(d)** compares their potential response at a single pH to demonstrate baseline variation in their voltage signals. The low spread in sensitivities confirms that one-point calibration is sufficient to convert any one pH sensor's electrical signal into a meaningful pH measurement, making these sensors simple to use in real-world applications with low preparatory overhead.

Following benchtop characterization in buffer solutions, we demonstrate that the printed electrode-based sensors are equally high performing in biofluids including sweat, urine, and saliva. Na^+ is chosen as the target analyte as its concentration in these biofluids is relevant to assessing kidney disease and heart failure among other health complications, as well as for monitoring electrolyte loss or dehydration during exercise.[1,26–29] Na^+ sensors are fabricated on the printed electrode arrays and used to measure sweat, urine, and saliva samples. The sensor results are compared with inductively coupled plasma spectrometry (ICP-MS), a standard method of measuring ionic content (**Table 1** in the Appendix of this chapter). There is good coherence between the sensor and ICP-MS results for all the tested samples and across orders of magnitude of Na^+ concentration. This highlights the reliability of the printed array-based sensors for accurate and wide-range quantification of analytes in diverse biofluids.

2.4 On-body sweat sensing with functionalized printed electrodes

To establish the versatility of these sensors for personalized health monitoring, we choose a model application in fitness tracking to exhibit sensor durability over continuous, long-term, *in situ* use. Sweat pH is chosen for monitoring as pH can indicate anaerobic metabolism and muscle fatigue and is thus useful to track continuously during exercise.[30] **Fig. 6** shows real-time, on-body
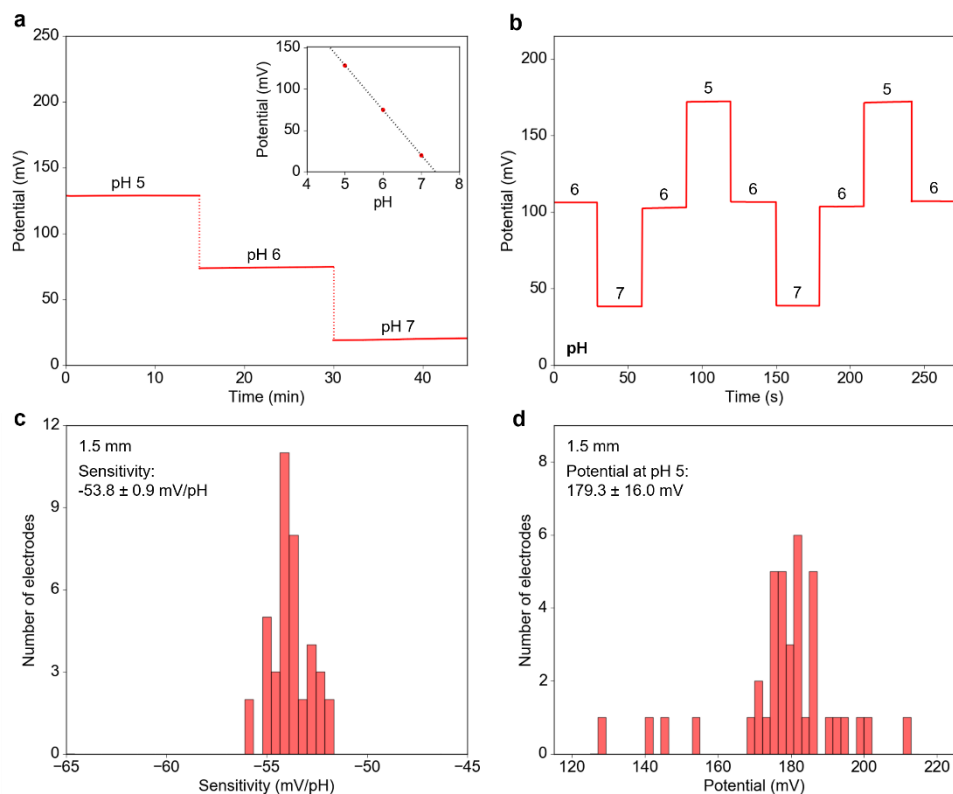
Figure 5. The pH sensor is chosen for extensive analysis of sensor performance and uniformity on the R2R printed electrodes. a) pH sensor is immersed in a sequence of buffer solutions of different pH and measured in each for 15 minutes. The sensor shows good stability with low drift over long-term measurement, with maintained near-Nernstian sensitivity. b) The sensor is cycled through solutions of pH 5, 6, and 7 and shows consistent signal for each pH, demonstrating repeatability. c) A collection of 40 pH sensors are fabricated and their sensitivities measured using calibration solutions of pH 5, 6, and 7. With a mean sensitivity of -53.8 ± 0.9 mV/pH, the printed electrode-based pH sensors show high uniformity in sensitivity with near-Nernstian performance. d) Potential values returned by the 40 pH sensors in a solution of pH 5 are compared as a histogram. Standard deviation of 16.0 mV implies that one-point calibration is necessary for obtaining accurate sensor measurements.

monitoring of sweat pH during stationary biking. The printed array-based pH sensor is secured conformally against the subject's arm by a wristband. A thin PDMS wall is included to surround the sensing electrodes, creating a well for sweat to accumulate in to reduce evaporation and prevent abrasion of the sensing layer against skin. The sensor can be connected to a commercial potentiometer or to custom circuitry that enables wireless data collection and transmission, as demonstrated previously for wearable sweat sensors.[1–3,7] Sweat pH measurement is conducted over a duration of exercise including 6 minutes of warm up followed by 45 minutes of biking at a power of 120 W (**Fig. 6(a)**). During the first 14 minutes, enough sweat does not fill the PDMS well to
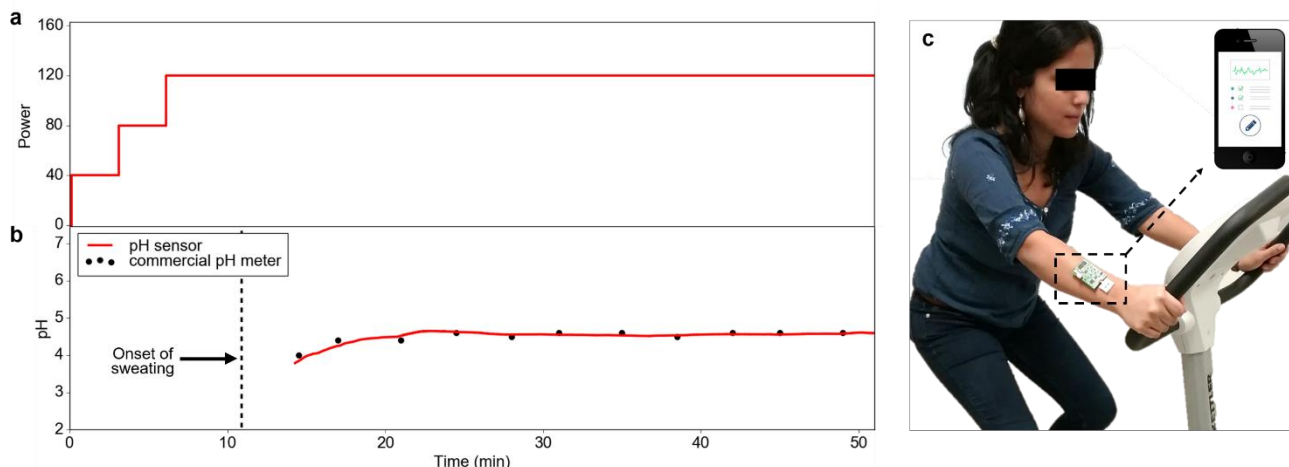
Figure 6. Real time, *in situ* measurement of sweat pH using a R2R gravure printed electrode-based sensor worn on the arm during stationary biking. a) Cycling power is gradually ramped up at the start of the trial and then maintained. b) Real-time sweat pH measurement shows an initial gradual increase and then is stable for the remainder of exercise, consistent with *ex situ* measurements of collected sweat samples using a commercial pH meter. Sweating begins 11 minutes into biking, but no sensor reading is shown for the first 14 minutes as accumulated sweat is too little for the sensor to give a meaningful response. c) Continuous pH analysis is enabled by configuring the sensor array with a custom PCB for signal processing and wireless transmission to a smart phone.

impinge on the sensor, so no meaningful pH reading is obtained. Once the well is adequately filled, the sensor starts reading and initially shows a gradual increase in pH reflecting a reduction in lactic acid content consistent with the literature (**Fig. 6(b)**).[3] Sweat pH is stable for the remaining duration of biking. During the trial, sweat is collected from the subject for *ex situ* testing with a commercial pH meter. The on-body data closely matches the commercial pH meter readings, demonstrating the accuracy of the printed array-based sensors for continuous, real-time measurement of physiological indicators in mechanically rigorous *in situ* environments.

While continuous on-body sensing demonstrates the extent to which these printed electrode-based biosensors can be utilized, they are also appropriate for one-time use in medical screening applications. The high throughput, cost effective production of R2R gravure printed electrodes, combined with their ability to easily interface with signal conditioning devices like custom PCBs, makes them well suited for use as inexpensive, disposable test strips for applications including cystic fibrosis diagnosis or sweat glucose monitoring.[13] Additionally, large-scale production of highly uniform sensors can enable research into the physiological relevance of non-invasively accessed biofluids. Uniformly performing R2R printed electrodes make it viable to conduct the population studies needed to understand how sweat, saliva, urine, or tear biomarkers reflect overall health and fitness. In future, gravure printing can be expanded towards direct printing of functional sensor membranes onto the underlying electrodes. More complex hierarchical structures could be implemented, including incorporating redox buffers into the electrode stack to improve reproducibility of potentials for calibration-free sensing.[31] Eventually,

these sensor fabrication processes could be combined with R2R integration of microfluidics and electronic components to enable high speed, large scale production of entire wearable sensing devices.

2.5 Conclusion

In summary, we have designed R2R gravure printed electrodes for a diverse range of noninvasive biosensing applications geared towards point-of-care health monitoring and diagnosis. With fine-tuned inks and printed layer stacking, the electrodes show consistent redox kinetics and are high performing under a variety of sensing modalities. They can be functionalized into sensors for analytes including ions, metabolites, and heavy metals, and are suitable both for continuous *in situ,* monitoring of physiological indicators as well as for *ex situ*, single-time measurements for medical screenings. We demonstrate high-throughput fabrication across large swathes of flexible substrate, enabling inexpensive, large-scale production of disposable sensing components for wearable hybrid electronics with a view to making personalized health monitoring at molecular levels accessible to the broader community.

2.6 Methods

2.6.1 Ink Formulation

Raw Ag dispersed solution (TEC-PR-041) purchased from InkTec Co., Ltd. Korea was reformulated to achieve stability in aqueous environments. The viscosity and wetting properties of the Ag ink were optimized by adding polymer binder. Specifically, 2g of PVB (poly(vinyl butyral)) with molecular weight of 272.341 g/mol (Sigma Aldrich) was dissolved in Terpineol (18 g) and used as the PVB solution to adjust viscosity and wetting. By adding 10 wt% of PVB binder solution to the Ag dispersed solution (TEC-PR-041; InkTec Co., Ltd. Korea), the viscosity and surface tension were respectively modified to 100 cp and 31 mN/m and provided the best quality Ag printed electrode. For the carbon working and counter electrodes, carbon ink was printed over the Ag layer using carbon paste (DC-15; Dozen TECH corp., Korea) diluted with ECA (Diethylene glycol monoethyl ether acetate) to achieve a viscosity of 350 cp. Insulating ink to passivate the printed Ag lines was formulated by dissolving 20 g of PE (polyethylene) resin (Daejung Chem. Korea) in 80 mL of ECA to achieve a viscosity of 210 cp and surface tension of 31 mN/m.

2.6.2 R2R Gravure Printing

To print the electrode arrays with layers of silver, carbon, and insulation ink, R2R gravure printing was carried on poly(ethylene terephthalate) (PET) web, 250 mm wide and 100 μm thick with lengths up to 150 m (AH71D, SKC, Korea). For continuous printing, R2R gravure with two printing units (manufactured by I-PEN, Korea) was combined with a custom-made servomechanism system with web tension of 5 ± 0.3 kgF. During the printing process, an overlay printing registration accuracy of ± 20 μm was maintained under a temperature of 23 ± 2 °C and a humidity of 35 ± 2 %. At the first printing unit, Ag electrodes were printed and dried by passing through a drying chamber (150 °C) for 1 min with a printing speed of 6 m/min. A carbon layer

was next printed on top of the printed Ag for the working and counter electrodes, and dried by passing through the drying chamber (150 °C) for 1 min. The printed roll was rewound and the Ag and carbon inks further cured for 3 min by again passing through the 150 °C heating chamber at a speed of 2 m/min. Finally, the insulator layer was printed on the rewound PET roll at the same speed of 6 m/min. The total printing time to complete the 3-layer printing and curing of 150,000 electrodes on 150 m of PET web was about 30 min. A summary of the R2R gravure system parameters for printing the electrode arrays is provided in Table 2 in the Appendix of this chapter.

2.6.3 Electrode Pretreatment

To activate the carbon electrodes, pretreatment processing was conducted in 2 stages. First, arrays from the R2R gravure printed roll were annealed at 160 °C for 1 hour and allowed to cool back to room temperature. They were then electrochemically cleaned using cyclic voltammetry (CV) in 0.1 M HCl from 0 to 0.8 V for 10 cycles at 100 mV/s to further remove residues and solvents from the printing process.

2.6.4 Sensor Functionalization

Functionalized sensing layers were deposited or grown on the printed arrays using procedures and recipes detailed in our previous work[1–3]. For the pH sensor, aniline was distilled at a temperature of 100 °C and a vapor pressure of 13 mmHg for purification before use. Polyaniline (PANI) was polymerized and electrodeposited on the working electrode surface with a 0.1 M aniline/1 M H_2SO_4 solution using cyclic voltammetry from −0.2 to 1 V for 25 cycles at 100 mV/s. For the sodium sensor, a membrane solution was prepared consisting of Na ionophore X (1% weight by weight, w/w), Na-TFPB (0.55% w/w), PVC (33% w/w), and DOS (65.45% w/w). 100 mg of the membrane cocktail was dissolved in 660 μL of tetrahydrofuran. For the potassium sensor, the membrane solution was composed of valinomycin (2% w/w), NaTPB (0.5%), PVC (32.7% w/w), and DOS (64.7% w/w). 100 mg of the membrane cocktail was dissolved in 350 μL of cyclohexanone. For both sodium and potassium sensors, PEDOT:PSS was chosen as the ion-to-electron transducer to minimize potential drift of the ISEs, and was deposited onto the working electrodes by galvanostatic electrochemical polymerization using a solution of 0.01 M EDOT/0.1 M NaPSS. A constant current of 14 μA (2 mA cm^{-2}) was applied to produce polymerization charges of 10 mC on each electrode. Following PEDOT:PSS growth, 10 μL of the sodium membrane cocktail and 4 μL of the potassium membrane cocktail were deposited onto their respective 3 mm electrodes, with cocktail volume scaled down with area for smaller sensor dimensions. For both sensors, the printed silver electrode was made into a PVB reference using a solution of 79.1 mg PVB and 50 mg of NaCl dissolved int 1 mL methanol, 36.2 mg F127, and 0.2 mg of multiwall carbon nanotubes added to minimize potential drift. 10 μL of this solution was deposited on the 3 mm Ag reference electrode but scaled with area for smaller sensor sizes. For the glucose sensor membrane solution, 1% chitosan solution with 2% acetic acid was prepared under magnetic stirring. This membrane solution was combined with glucose oxidase solution (1 mg enzyme in 100 μL of PBS of pH 7.2) in a 1:1 v/v ratio. Prussian Blue mediator was deposited

onto the carbon working electrode using cyclic voltammetry from 0 to 0.5 V with respect to the printed Ag reference for one cycle at 20 mV/s, using a plating solution of 2.5 mM $FeCl_3$, 100 mM KCl, 2.5 mM $K_3[Fe(CN)_6]$, and 100 mM HCl. 3 µL of the membrane solution was cast over the 3 mm electrodes and allowed to dry overnight at ambient temperature. Membrane solution volume was scaled with electrode area for smaller electrode dimensions. Copper sensors were realized by directly using the pretreated electrodes. Pre-concentration was conducted at -0.2 V for 30 seconds to accumulate copper onto the electrode, followed by square wave stripping voltammetry (SWSV) for detection. Caffeine sensors were prepared by casting 0.8 µL of 0.01% multiwall carbon nanotubes in ethanol, followed by 0.8 µL of 0.01% Nafion, on the pre-treated electrodes.

2.6.5 On-Body Measurement During Exercise

On-body sensor measurement during stationary biking was conducted at the University of California, Berkeley in compliance with human research protocol (CPHS 2014-08-6636) approved by the Berkeley Institutional Review Board (IRB). All subjects gave written, informed consent. An electronically braked leg-cycle ergometer (Kettler E3 Upright Ergometer Exercise Bike) was used for stationary biking. Subjects' wrists were cleaned with water and dried with gauze before securing the sensing patch.

2.7 References

(1) Gao, W.; Emaminejad, S.; Nyein, H. Y. Y.; Challa, S.; Chen, K.; Peck, A.; Fahad, H. M.; Ota, H.; Shiraki, H.; Kiriya, D.; Lien, D.-H.; Brooks, G. A.; Davis, R. W.; Javey, A. Fully Integrated Wearable Sensor Arrays for Multiplexed *In Situ* Perspiration Analysis. *Nature* **2016**, *529*, 509-514.

(2) Gao, W.; Nyein, H. Y. Y.; Shahpar, Z.; Fahad, H. M.; Chen, K.; Emaminejad, S.; Gao, Y.; Tai, L.-C.; Ota, H.; Wu, E.; Bullock, J.; Zeng, Y.; Lien, D.-H.; Javey, A. Wearable Microsensor Array for Multiplexed Heavy Metal Monitoring of Body Fluids. *ACS Sens*. **2016**, *1,* 866-874.

(3) Nyein, H. Y. Y.; Gao, W.; Shahpar, Z.; Emaminejad, S.; Challa, S.; Chen, K.; Fahad, H. M.; Tai, L.-C.; Ota, H.; Davis, R. W.; Javey, A. A Wearable Electrochemical Platform for Noninvasive Simultaneous Monitoring of Ca^{2+} and pH. *ACS Nano* **2016**, *10*, 7216-7224.

(4) Bariya, M.; Nyein, H. Y. Y.; Javey, A. Wearable Sweat Sensors. *Nat. Electron.* **2018**, *1*, 160–171.

(5) Rose, D. P.; Ratterman, M. E.; Griffin, D. K.; Hou, L.; Kelley-Loughnane, N.; Naik, R. R.; Hagen, J. A.; Papautsky, I.; Heikenfeld, J. C. Adhesive RFID Sensor Patch for Monitoring of Sweat Electrolytes. *IEEE Trans. Biomed. Eng.* **2015**, *62*, 1457–1465.

(6) Choi, J.; Kang, D.; Han, S.; Kim, S. B.; Rogers, J. A. Thin, Soft, Skin-Mounted Microfluidic Networks with Capillary Bursting Valves for Chrono-Sampling of Sweat. *Adv. Healthc. Mater.* **2017**, *6*, 1601355. DOI: 10.1002/adhm.201601355

(7) Kim, J.; Jeerapan, I.; Imani, S.; Cho, T. N.; Bandodkar, A.; Cinti, S.; Mercier, P. P.; Wang, J. Noninvasive Alcohol Monitoring Using a Wearable Tattoo-Based Iontophoretic-Biosensing System. *ACS Sens.* **2016**, *1*, 1011-1019.

(8) Jia, W.; Bandodkar, A. J.; Valdés-Ramírez, G.; Windmiller, J. R.; Yang, Z.; Ramírez, J.; Chan, G.; Wang, J. Electrochemical Tattoo Biosensors for Real-Time Noninvasive Lactate Monitoring in Human Perspiration. *Anal. Chem.* **2013**, *85,* 6553-6560.

(9) Bandodkar, A. J.; Jia, W.; Yardımcı, C.; Wang, X.; Ramirez, J.; Wang, J. Tattoo-Based Noninvasive Glucose Monitoring: A Proof-of-Concept Study. *Anal. Chem.* **2014**, *87*, 394-398.

(10) Bandodkar, A. J.; Wang, J. Non-Invasive Wearable Electrochemical Sensors: A Review. *Trends Biotechnol.* **2014**, *32*, 363–371.

(11) Sonner, Z.; Wilder, E.; Gaillard, T.; Kasting, G.; Heikenfeld, J. Integrated Sudomotor Axon Reflex Sweat Stimulation for Continuous Sweat Analyte Analysis with Individuals at Rest. *Lab. Chip* **2017**, *17*, 2550–2560.

(12) Kim, J.; Imani, S.; Araujo, W. R. de; Warchall, J.; Valdés-Ramírez, G.; Paixão, T. R. L. C.; Mercier, P. P.; Wang, J. Wearable Salivary Uric Acid Mouthguard Biosensor with Integrated Wireless Electronics. *Biosens. Bioelectron.* **2015**, *74*, 1061-1068.

(13) Emaminejad, S.; Gao, W.; Wu, E.; Davies, Z. A.; Nyein, H. Y. Y.; Challa, S.; Ryan, S. P.; Fahad, H. M.; Chen, K.; Shahpar, Z.; Talebi, S.*;* Milla, C.; Javey, A. Autonomous Sweat Extraction and Analysis Applied to Cystic Fibrosis and Glucose Monitoring Using a Fully Integrated Wearable Platform. *Proc. Natl. Acad. Sci.* **2017**, *114*, 4625–4630.

(14) Bandodkar, A. J.; Jeerapan, I.; Wang, J. Wearable Chemical Sensors: Present Challenges and Future Prospects. *ACS Sens.* **2016**, *1*, 464–482.

(15) Grau, G.; Cen, J.; Kang, H.; Kitsomboonloha, R.; Scheideler, W. J.; Subramanian, V. Gravure-Printed Electronics: Recent Progress in Tooling Development, Understanding of Printing Physics, and Realization of Printed Devices. *Flex. Print. Electron.* **2016**, *1*, 023002. DOI:10.1088/2058-8585/1/2/023002

(16) Abbel, R.; Meinders, E. R. Printing Technologies for Nanomaterials. In *Nanomaterials for 2D and 3D Printing*; Shlomogdassi; Kamyshny, A., Eds.; Wiley-VCH Verlag GmbH & Co. KGaA, 2017; pp 1–26.

(17) Jung, Y.; Park, H.; Park, J.-A.; Noh, J.; Choi, Y.; Jung, M.; Jung, K.; Pyo, M.; Chen, K.; Javey, A.; Cho, G. Fully Printed Flexible and Disposable Wireless Cyclic Voltammetry Tag. *Sci. Rep.* **2015**, *5*.

(18) Lau, P. H.; Takei, K.; Wang, C.; Ju, Y.; Kim, J.; Yu, Z.; Takahashi, T.; Cho, G.; Javey, A. Fully Printed, High Performance Carbon Nanotube Thin-Film Transistors on Flexible Substrates. *Nano Lett.* **2013**, *13*, 3864–3869.

(19) Lee, W.; Koo, H.; Sun, J.; Noh, J.; Kwon, K.-S.; Yeom, C.; Choi, Y.; Chen, K.; Javey, A.; Cho, G. A Fully Roll-to-Roll Gravure-Printed Carbon Nanotube-Based Active Matrix for Multi-Touch Sensors. *Sci. Rep.* **2015**, *5*.

(20) Yeom, C.; Chen, K.; Kiriya, D.; Yu, Z.; Cho, G.; Javey, A. Large-Area Compliant Tactile Sensors Using Printed Carbon Nanotube Active-Matrix Backplanes. *Adv. Mater.* **2015**, *27*, 1561–1566.

(21) Blayo, A.; Pineaux, B. Printing Processes and Their Potential for RFID Printing. In *Proceedings of the 2005 Joint Conference on Smart Objects and Ambient Intelligence: Innovative Context-aware Services: Usages and Technologies*; sOc-EUSAI '05, ACM: New York, NY, USA, 2005; pp 27–30.

(22) Heikenfeld, J. Non-invasive Analyte Access and Sensing through Eccrine Sweat: Challenges and Outlook circa 2016. *Electroanalysis* **2016**, *28*, 1242–1249.

(23) Kim, S.; Sung, H. J. Effect of Printing Parameters on Gravure Patterning with Conductive Silver Ink. *J. Micromechanics Microengineering* **2015**, *25*, 045004. DOI:10.1088/0960-1317/25/4/045004

(24) Wang, J. Practical Considerations. In *Analytical Electrochemistry*; John Wiley & Sons, Inc., 2006; pp. 115–163.

(25) Tai, L.-C.; Gao, W.; Chao, M.; Bariya, M.; Ngo, Q. P.; Shahpar, Z.; Nyein, H. Y. Y.; Park, H.; Sun, J.; Jung, Y.; Wu, E.; Fahad, H. M.; Lien, D.-H.; Ota, H.; Cho, G.; Javey, A. Methylxanthine Drug Monitoring with Wearable Sweat Sensors. *Adv. Mater.* **2018** (in press).

(26) White, A. G.; Gordon, H.; Leiter, L. Studies in Edema. II. The Effect of Congestive Heart Failure on Saliva Electrolye Concentrations. *J. Clin. Invest.* **1950**, *29*, 1445–1447.

(27) Goldberg, M.; Handler, J. S. Hyponatremia and Renal Wasting of Sodium in Patients with Malfunction of the Central Nervous System. *N. Engl. J. Med.* **1960**, *263*, 1037–1043.

(28) Sant'agnese, P. a. D.; Darling, R. C.; Perera, G. A.; Shea, E. Abnormal Electrolyte Composition of Sweat in Cystic Fibrosis of the Pancreas: Clinical Significance and Relationship to the Disease. *Pediatrics* **1953**, *12*, 549–563.

(29) Maughan, R. J. Fluid and Electrolyte Loss and Replacement in Exercise. *J. Sports Sci.* **1991**, *9*, 117–142.

(30) Patterson, M. J.; Galloway, S. D. R.; Nimmo, M. A. Effect of Induced Metabolic Alkalosis on Sweat Composition in Men. *Acta Physiol. Scand.* **2002**, *174*, 41–46.

(31) Hu, J.; Stein, A.; Bühlmann, P. Rational Design of All-Solid-State Ion-Selective Electrodes and Reference Electrodes. *Trends Anal. Chem.* **2016**, *76*, 102–114.

(32) Khan, Y.; Thielens, A.; Muin, S.; Ting, J.; Baumbauer, C.; Arias, A. C. A New Frontier of Printed Electronics: Flexible Hybrid Electronics. *Adv. Mater.* **2019,** *32*, 1905279.

(33) Wu, X.; Khan, Y.; Ting, J.; Zhu, J.; Ono, S.; Zhang, X.; Du, S.; Evans, J. W.; Lu, C.; Arias, A. C. Large-Area Fabrication of High-Performance Flexible and Wearable Pressure Sensors. *Adv. Electron. Mater.* **2020**, *6*, 1901310.

(34) Payne, M. E.; Zamarayeva, A.; Pister, V. I.; Yamamoto, N. A.; Arias, A. C. Printed, flexible lactate sensors: Design considerations before performing on-body measurements. *Sci. Rep*. **2019** *9*, 1-10.

(35) Lewis, J. A.; Ahn, B. Y. Three-Dimensional Printed Electronics. *Nature*, **2015**, *518,* 42-43.

(36) Kim, J.; Kumar, R.; Bandodkar, A. J.; Wang, J. Advanced Materials for Printed Wearable Electrochemical Devices: A Review. *Adv. Electron. Mater.* **2017,** *3*, 1600260.

(37) Gao, W.; Ota, H.; Kiriya, D.; Takei, K.; Javey, A. Flexible Electronics Toward Wearable Sensing. *Acc. Chem. Res.* **2019,** *52*, 523-533.

2.8 Appendix

2.8.1 Figure S1: Effect of pretreatment on electrochemical sensitivity and surface composition.
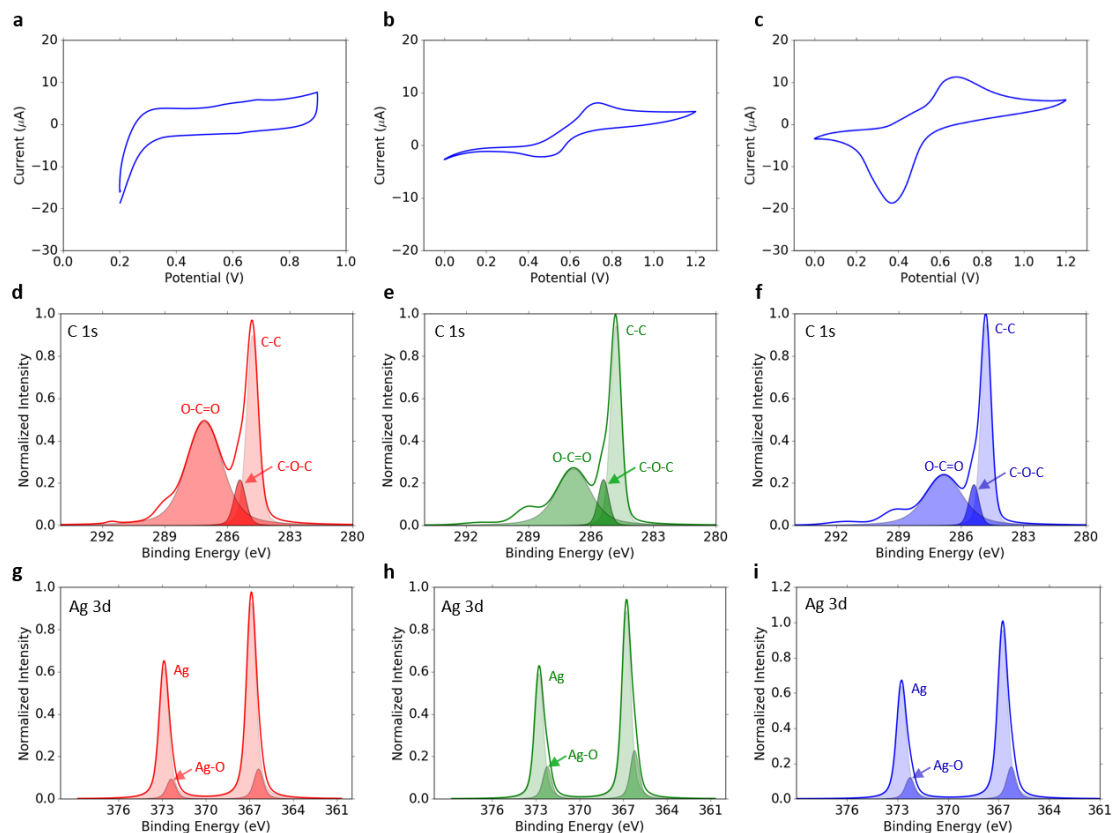

Figure S1. Effect of pretreatment on electrochemical sensitivity and surface composition. a) Cyclic voltammetry (CV) of a representative 1.5 mm array in 10 mM $K_3[Fe(CN)_6]$ before pretreatment, scanned at 100 mV/sec. b) CV of 1.5 mm array after annealing for 1 hr at 160 ⁰C. c) CV of 1.5 mm array after both annealing and acid-treatment (CV in dilute HCl) are conducted to activate the electrode surface. Overall, this optimized sequence of pretreatment procedures enhances electrode sensitivity to electrochemical events as indicated by increasingly prominent redox peaks. d) C 1s XPS spectrum showing main subpeaks (shaded) and total fit (solid line) of the carbon electrode before pretreatment, e) after the first pretreatment step of annealing, and f) after the second pretreatment step of acid treatment. There is a monotonic increase in the relative peak ratio of carbon-to-carbon versus carbon-to-oxygen subpeaks following each pretreatment steps. g) Ag 3d XPS spectrum showing main subpeaks (shaded) and total fit (solid line) of the silver electrode before pretreatment, h) after annealing, and i) after acid treatment. The ratio of silver-to-oxygen versus silver metal peaks reveals a slight increase in oxygen content after annealing, followed by a slight decrease after acid-treatment. Note: Only main subpeaks are shown for all C 1s spectra, with satellite or shake-up peaks omitted. Additionally, all depicted XPS spectra are charge corrected to the main C 1s subpeak position at 284.8 eV.

2.8.2 Table 1: Comparison of printed sensor response and ICP-MS results for biofluid samples.

Biosample	Measured [Na$^+$] (mM)	
	Na$^+$ Sensor	ICP-MS
Sweat 1	101.2	101.8
Sweat 2	65.2	65.2
Urine 1	137.6	137.4
Urine 2	109.3	110.4
Saliva 1	11.8	11.9
Saliva 2	4.7	5.0

Table 1. Collected biofluid samples tested *ex situ* for sodium content using a R2R printed electrode-based Na$^+$ sensor versus inductively coupled plasma spectrometry (ICP-MS). The sensor measurements cohere with ICP-MS results for sweat, urine, and saliva samples across a wide concentration range. For ICP-MS, samples were diluted before measurement and the resulting concentration signals appropriately compensated.

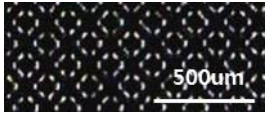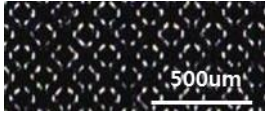*2.8.3 Table 2: Summary of the R2R gravure printing system.*

	Engraved Cell Structure (**D**epth(μm)/**L**ine(line)/**W**all(μm))	Printing Speed (m/min)	Blading Angle (°)	Web force (kg)	Nip force (kg)	Viscosity (cP)	Surface tension (mN/m)	Drying Temperature (°C)
1st layer - Silver ink	D – 10 μm L – 350 line W – 10 μm 	6	0	5	6	100	31	150
2nd layer - Carbon ink	D – 30 μm L – 185 line W – 5 μm 	6	9	5	6	350	30	150
3rd layer - Insulation ink	D – 30 μm L – 185 line W – 5 μm 	6	9	5	6	210	31	150

Table 2. Summary of the R2R gravure printing system. Schematics of the engraved cell structure along with printing parameters for each ink layer are shown.

2.8.3 Notes on CV data processing.

To calculate reduction peak current i_P from cyclic voltammetry (CV) data, baseline current must be identified as a reference for establishing the peak magnitude. To do this, Python code was written to tangentially extrapolate the high-voltage portion of the reverse scan up to a position under the reduction peak. At the peak voltage, this baseline was subtracted from the absolute peak current to obtain i_P.

2.8.4 Notes on SEM.

SEM images were recorded on a Zeiss Gemini Ultra-55 Analytical scanning electron microscope with accelerating voltage of 5 kV.

Chapter 3: High-throughput microfluidic sensors for regional and correlative analysis of iontophoretic and exercise sweat

Sections of the following chapter have been previously published in a similar format, and are reprinted and/or adapted with permission from the following works:

H. Y. Y. Nyein[*], M. Bariya[*], L. Kivimaki, S. Uusitalo, T. S. Liaw, E. Jansson, C. H. Ahn, J. A. Hangasky, J. Zhao, Y. Lin, T. Happonen, M. Chao, C. Liedert, Y. Zhao, L.-C. Tai, J. Hiltunen, A. Javey. Regional and Correlative Sweat Analysis Using High-Throughput Microfluidic Sensing Patches Towards Decoding Sweat. *Sci. Adv.* **2019**, *5*(8), eaaw9906.

Z. Yuan[*], L. Hou[*], M. Bariya[*], H. Y. Y. Nyein, L.-C. Tai, W. Ji, L. Li, and A. Javey. "A Multi-Modal Sweat Sensing Patch for Cross-Verification of Sweat Rate, Total Ionic Charge, and Na^{+} Concentration." *Lab Chip* **2019**, *19*(19), 3179-3189.

[*]These authors contributed equally.

3.1 Introduction

While recent sweat analysis has overwhelmingly focused on measuring biomarker concentrations, one of the most physiologically informative parameters is actually sweat secretion rate. Sweat rate is important to track as it modulates the concentrations of secreted analytes, and even stand-alone it can indicate evolving or unfavorable health conditions including cardiac complications, neuronal damage, and dehydration[1–5]. Precise and continuous sweat sensors are therefore an important component of wearable sweat sensing technology for medical and athletic applications.

We previously developed a microfluidic sweat sensing patch for simultaneous monitoring of sweat composition and sweat rate[6]. The patch has a flexible plastic substrate on which electrochemical sensors are patterned and functionalized. A polydimethylsiloxane (PDMS) microfluidic layer is bonded on top. This layer contacts skin when the patch is worn on-body, and has a central opening where sweat collects and enters the device before pushing into an enclosed, spiraling microchannel that moves older sweat away from the collection well as fresher sweat is pushed in. Electrochemical sensors are situated within the collection well to ensure composition measurements are made in the freshest sweat. Located within the spiraling microchannel are two parallel metal electrodes for electrical sweat rate measurement. As sweat accumulates in the device and flows in the channel, it increasingly covers and electrically connects the embedded electrodes, causing the admittance measured between them to rise. The rate at which the admittance signal changes can be related to the rate at which sweat is flowing in the channel. Assuming that all the sweat secreted within the collection well area pushes into the device and the channel without leakage, the flow rate in the device matches the sweat secretion rate on the skin surface. In this way, the admittance signal can be calibrated into a measure of sweat secretion rate.
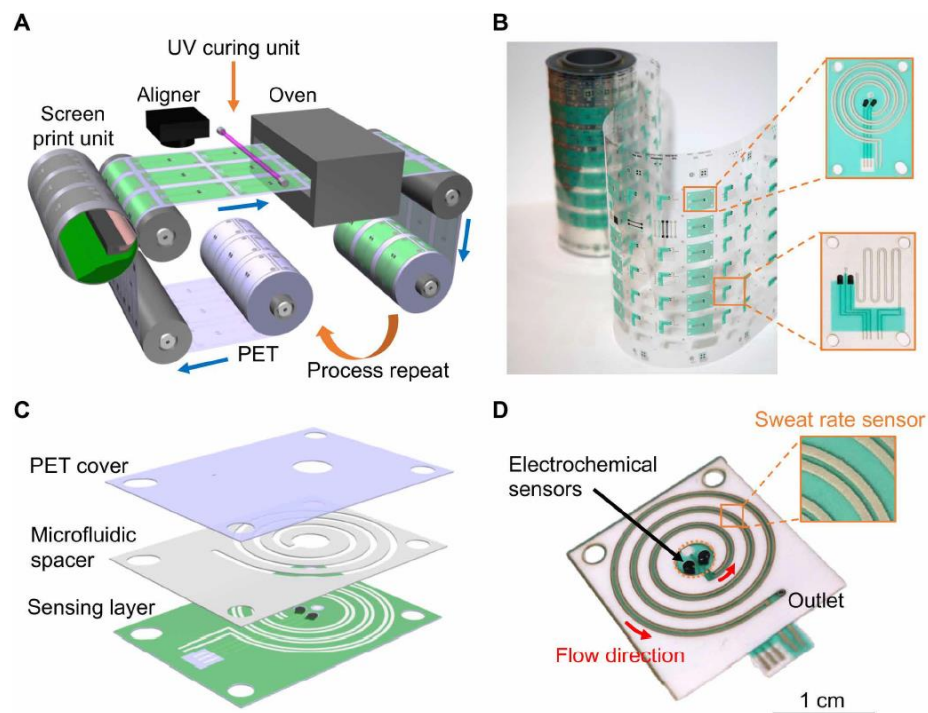
Figure 1. Schematics of roll-to-roll fabricated sweat sensing patches for regional and correlative sweat analysis. **a)** R2R rotary screen printing of the wearable biosensing patch and **b)** optical image of sensing electrode patterns printed via R2R processing are shown. **c)** The biosensing patch is assembled by combining the sensing layer, microfluidic adhesive spacer, and PET cover sheet. **d)** The assembled biosensing patch includes electrochemical sensors contained within the collection reservoir and electrical sweat rate sensor embedded in the microfluidic channel.

High throughput fabrication of sweat sensors with low inter-sensor variability is key to enabling sufficient data collection from subject studies to decode the physiological relevance of sweat and meaningfully interpret sensor measurements[7,8]. Towards this goal, we adapted roll-to-roll (R2R) processing techniques to produce microfluidic sensing patches at scale, including using

R2R screen printing of electrode and passivation layers and R2R laser-cutting of adhesives to define sweat collection wells and microchannels (**Figure 1**). **Figure 1a** shows a schematic of the roll-to-roll printing apparatus used to print electrochemical and sweat rate sensing arrays at rates of 60 patches per minute on 100-meter web lengths, while **Figure 1b** shows an image of the resulting printed roll with magnifications of two electrode array structures. Simultaneously, R2R laser cutting is used to define a microfluidic channel in a double-sided plastic adhesive layer and to cut out a sweat collection well opening in a capping layer that otherwise encloses the channel. These layers can be manually aligned and adhered over the printed electrode array layer (**Figure 1c**) to rapidly assemble a complete microfluidic sensing patch that can be functionalized for sweat composition and rate monitoring shown in **Figure 1d**.

3.2 Sweat-to-blood glucose relations in fasting iontophoretic sweat

One application for which the functionalized microfluidic sweat sensors can be used is to measure glucose concentrations in sweat and study their relation to blood glucose levels towards sweat-based diabetes diagnosis and monitoring. Conventionally, fasting blood glucose levels are measured via fingerstick blood glucose tests to determine whether an individual is likely to be non-diabetic, pre-diabetic, or diabetic, with universal concentration thresholds determining which category an individual falls into based on their blood glucose results. If sweat sampled during the fasting state is found to correlate with blood glucose measurements made at the same time, it would open up exciting opportunities for supplanting invasive blood tests with more convenient and continuous sweat-based monitoring. Importantly, the sweat that is sampled must reflect the body's equilibrium state. Exercise can alter the body's natural physiology and would therefore be an inappropriate method of sweat induction for studying fasting sweat-to-blood glucose correlations. Instead, iontophoretic sweat induction more closely preserves the overall resting body state. In this method, a cholinergic drug is transdermally delivered via topical application of a small current to locally stimulate the sweat glands. In this section, we use microfluidic sensors functionalized towards glucose to perform subject studies across healthy and diabetic cohorts to investigate correlations between iontophoretic sweat and blood glucose levels.

We first measure real-time glucose dynamics in the iontophoretic sweat of healthy and diabetic subjects as shown in **Figure 2a** and **2b** respectively. A new sensor patch is used per trial as the glucose sensors initially have similar currents and sensitivities within the batch but vary in their performance after undergoing wetting and drying that mechanically strains the sensing membranes. Two trials are conducted for each subject to observe longitudinal variations in how sweat glucose and sweat rate react to blood glucose changes. The glucose sensor response time is about a minute after sweat coverage of the sensor surface. This occurs within a couple minutes of the onset of sweating. Thirty minutes of measurements were performed. In the healthy subject's first trial, sweat glucose decreases from 80 to 72 μM over the 12-min sweating period while blood glucose decreases from 85 to 79 mg/dL. In the second trial, though the higher average sweat glucose parallels the higher blood glucose level, over the measurement period the sweat glucose concentration increases from 112 to 122 μM while the blood glucose level falls by 16 mg/dL. Sweat rate reduces relatively sooner in the first trial compared to the second. For the diabetic subject, sweat rate is relatively stable across both trials, and sweat glucose evolves in the same direction as blood glucose in both trials. In the first trial, sweat glucose increases from 40 to 74 μM as blood glucose increases by 10 mg/dL, while in the second trial sweat glucose decreases from 35 to 20 μM as blood glucose falls by only 1 mg/dL. The degree of change in sweat glucose concentration does not consistently track how much the blood glucose level has evolved. To verify this finding, we conduct off-body measurements of sweat glucose over multiple trials for a single healthy subject, as shown in **Figure 2c**. The glucose profiles over approximately 30 mins of sweat collection and measurement per trial show a rapid decrease in concentration followed by a gradual increase for this subject, indicating a complex glucose secretion dynamic that does not consistently
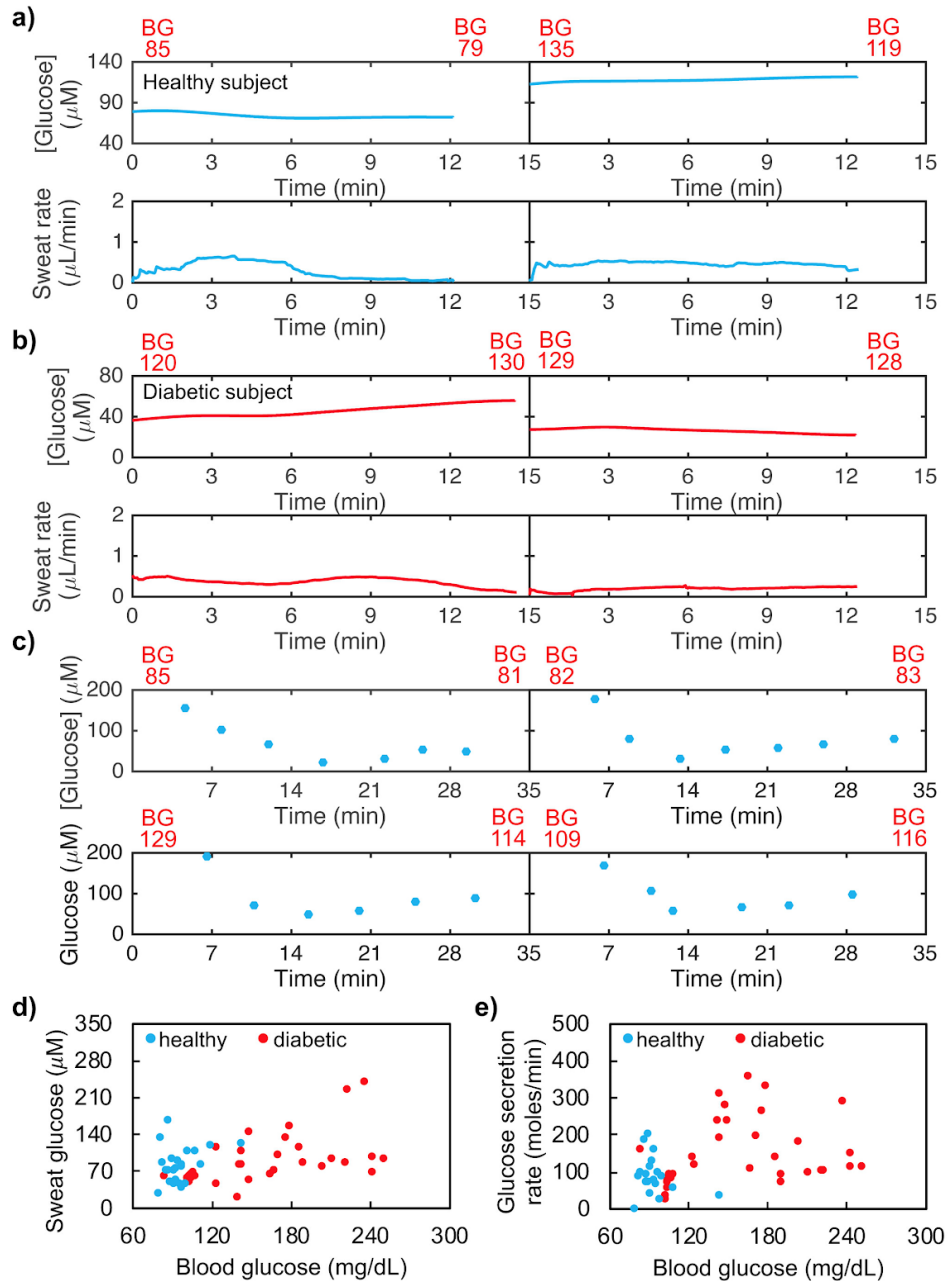
Figure 2. Regional analysis of iontophoretic sweat glucose and secretion rate in healthy and diabetic subjects. Real-time measurements of iontophoretic sweat [glucose] and sweat rate for **a)** one healthy and **b)** one diabetic subject repeated in two trials each show variation in sweat glucose response to changing blood glucose levels. **c)** Off-body measurements of dynamic glucose profiles in the iontophoretic sweat of one subject across four trials show that sweat glucose levels do not consistently evolve with blood glucose. **d)** Fasting levels of average sweat glucose versus blood glucose of 20 healthy and 28 diabetic subjects. **e)** Average sweat glucose secretion rate versus blood glucose across the healthy and diabetic cohorts.

follow the change in blood glucose. The glucose profiles for this subject differ from those of the subjects in **Figure 2a** and **2b**, which could be due to variation in the sweat rate profiles, with higher sweat rates diluting the secreted glucose concentrations for certain subjects, or due to more complex inter-subject variations. Further, the average sweat glucose level for each trial does not correlate one-to-one with average blood glucose: while average sweat [glucose] is 68, 78, 90, and 95 μM for the four trials, average blood glucose is 83, 83, 122, and 113 mg/dL respectively. In this study, time lag is not considered as we expect an equilibrium between sweat and blood and as the blood glucose levels remain relatively stable during fasting. Confirmation of the sweat glucose sensor accuracy, and verification of the sweat glucose concentrations and trends, is conducted via comparison to liquid chromatography in **Figures S1** and **S2** in the Appendix of this chapter. Further, all measured blood glucose values corresponding to the average values mentioned here are included in **Table S1** in the Appendix.

To investigate sweat-to-blood glucose relations more comprehensively, we conduct a population study of fasting blood and sweat glucose levels across healthy and diabetic cohorts of 20 and 28 subjects each. As fasting blood glucose can be indicative of diabetic state -- with universal thresholds for healthy, pre-diabetic, and diabetic diagnoses – it is important to determine whether fasting sweat levels consistently and universally correlate with blood[9]. **Figure 2d** shows the result of comparing average sweat glucose concentration with blood glucose across all subjects. All the data considered together gives a mild positive correlation with Pearson correlation coefficient of 0.3 and p-value of 0.016. Considering the healthy and diabetic cohorts independently, and removing an outlying point in both sets that is beyond two standard deviations of the mean, we obtain correlation coefficients of 0.28 with p-value of 0.167 and 0.42 with p-value of 0.016 respectively, indicating weak positive correlations in these sets with poor statistical significance. Overall, there is significant spread in the data, indicating that iontophoretic sweat glucose concentration does not robustly predict blood levels. However, sweat glucose concentration is expected to be sweat rate dependent – for example, one possible model suggests that glucose flux (the amount of glucose secreted through a sweat gland per time) is largely independent of sweat rate, meaning that glucose concentrations are diluted at higher sweat rates[10]. Taking this model into account, we consider how the glucose secretion rate relates to blood glucose by multiplying each subject's average sweat glucose concentration and sweat rate as shown in **Figure 2e**. The result is a poorer correlation with Pearson coefficient of 0.2. Given that a simple relation does not seem to exist across healthy and diabetic cohorts, obtaining longitudinal data for single subjects is one of the next steps to more deeply explore the glucose relation between sweat and blood. Understanding the mechanism of sweat glucose secretion could lend a physiological basis for more sophisticated models that account for or normalize by sweat rate, which may produce a stronger relationship with blood glucose. Stronger correlations may also be found by considering intra-subject correlations between sweat glucose flux and sweat rate. This remains an avenue of future work that could identify regimes in which sweat glucose matches blood concentrations. Overall, these results indicate that it would be difficult to accurately predict instantaneous blood glucose levels by considering iontophoresis sweat glucose and sweat rate alone with simple models. This
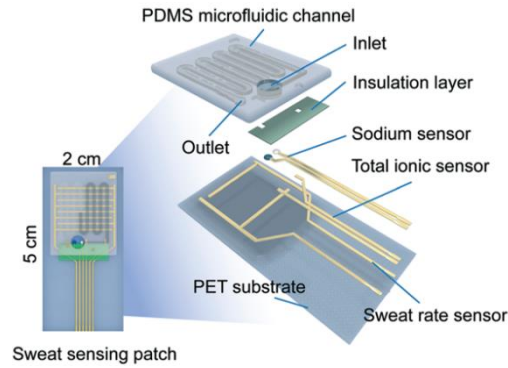
Figure 3. Sweat rate sensing patch with serpentine microchannel passing over interdigitated electrode gates for discrete but selective sweat rate measurement. In the blow-out of each layer, two gates are shown.

does not preclude the possibility of a more complex relation existing between sweat components and blood glucose, including multi-parameter dependencies and lag times. Further, while the lack of a uniform sweat-to-blood glucose correlation across all subjects makes it difficult to identify universal sweat thresholds for diabetes diagnostics or management, it is possible that more thorough longitudinal studies of sweat glucose could give rise to individual-specific relations between sweat and blood for personalized diabetes management.

Finally, to decode sweat glucose more holistically, it would be further insightful to compare glucose variations across body sites and for exercise sweat. Because the body undergoes dynamic physiological changes during the exertions of exercise, whereas local sweat stimulation via iontophoresis leaves the overall body largely in its resting state, the resulting sweat compositions may differ. For example, exercise sweat glucose may be more diluted due to the higher sweat secretion rates, and show decrease with time as glucose is rapidly flushed out of the sweat gland[11]. To better study these and other variable that affect sweat glucose, future studies should explore exercise sweat glucose trends across subjects, intra-subject regional variation in sweat glucose concentration, and the effect of sweat rate and sweat stimulation times on exercise and iontophoresis sweat glucose.

3.3 Discrete schemes for selective sweat rate measurement

The sweat rate sensing scheme involving admittance measurements between parallel electrodes embedded in a microfluidic allows for continuous sweat rate measurement but suffers from selectivity limitations. Specifically, the extracted admittance signal is not uniquely dependent on the position of sweat in the microchannel but also depends on the ionic concentration or conductivity of sweat, which can vary between individuals and over time during a single sweat secretion interval. This poses challenges for uniquely translating an admittance signal to a measure of sweat rate without simultaneously measuring and compensating for sweat conductivity variations.
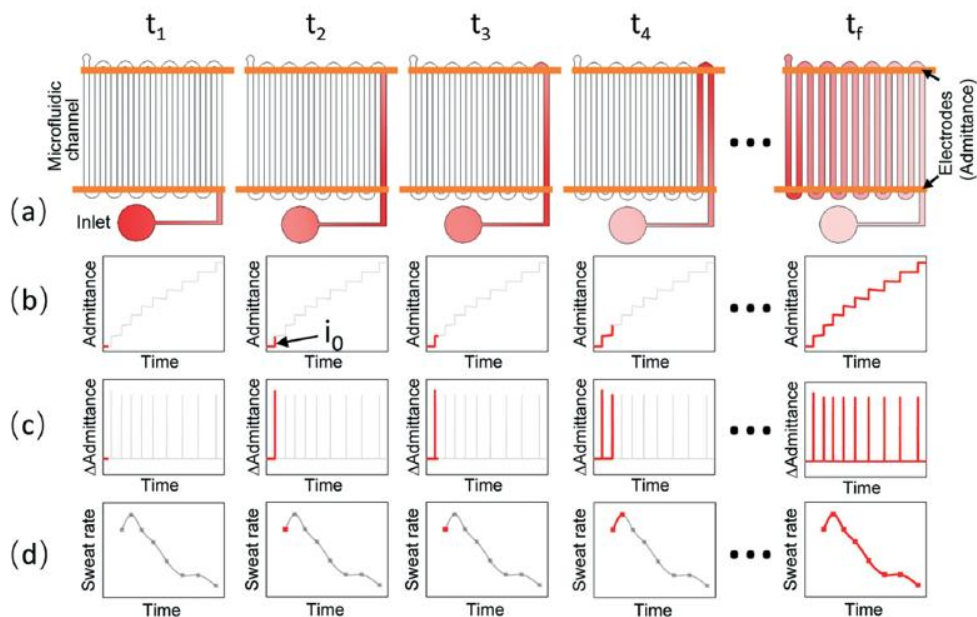
Figure 4. Schematic representation of how dynamic sweat rate measurements are made using the interdigitated sweat rate electrodes crossing the serpentine microchannel. (a) Schematic of fluid filling the serpentine microfluidic channel from time t_1 to t_f. Sweat rate electrode gates are shown in orange. A model ionic concentration gradient is indicated by the color gradient. (b) Corresponding admittance signal recorded between the sweat rate electrodes over time is shown in red. A step occurs each time fluid makes a new connection between the sweat rate electrode gates. Step height i_0 is determined by conductivity of the leading column of fluid. (c) Differential admittance signal. Spike occurs in response to fluid makes a new connection between the sweat rate electrode gates. The non-spike, background portion of the signal constitutes the drift within each admittance step shown in b. (d) As the spacing between electrode gates is known, this intervening volume can be divided by the time between differential admittance signal spikes to reconstruct sweat rate.

To address the selectivity limitations of the continuous sweat rate measurement scheme, an alternate method is developed that tracks discrete changes in admittance uniquely depending on the position of sweat within the microchannel. This modality uses electrodes nested within a serpentine microfluidic channel as shown in **Figure 3.** The electrical sweat rate sensor comprises of two electrodes, each with a projecting finger, or gate, over which the serpentine channel repeatedly passes. Each time fluid accumulating in the channel makes a new crossing of the electrode gates, the admittance measured between the electrodes discretely jumps. As these jumps occur when sweat has reached specific positions within the channel, the distance between electrode gates can be divided by the time between the admittance jumps to quantify sweat rate. This scheme

of processing admittance measurements to reconstruct sweat rate is shown schematically in **Figure 4**.

The actual magnitude of the admittance jump is set by the conductivity of the oldest captured sweat, which constitutes the front of the sweat column that is flowing in the channel and
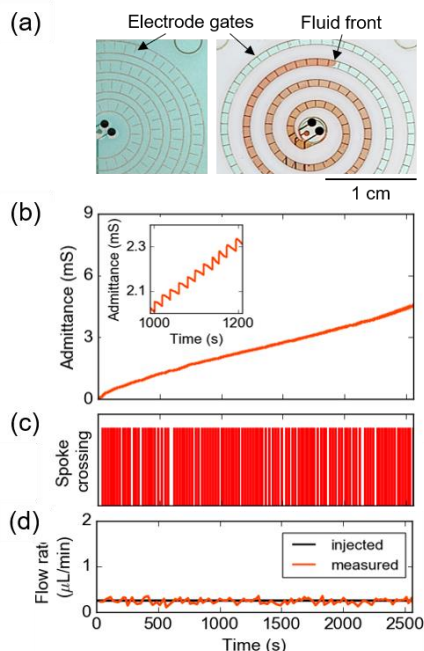

Figure 5. Updated discrete sweat rate sensor architecture. (a) The microfluidic has a spiraling microchannel with sweat rate electrode backbones on either side and interdigitated electrode gates that protrude into the channel. (b) As the sweat front advances in the channel, the admittance increases as a series of steps, visible in the inset. Each discrete step occurs when a new electrode gate or spoke is crossed. (c) The admittance signal can be processed to detect these sudden admittance increases. Here, each point at which a step crossing occurs is asserted as a red line. (d) The known channel volume between spokes is divided by the time between spoke crossings to estimate the flow rate at that time point. The measured rate (red) closely tracks the known, set injection rate (black) of fluid in the device.

making new connections between electrode gates. Because of the discrete nature of this measurement scheme, in which admittance jumps occur at well-defined distances within the channel and thus depend solely on sweat rate, this sensor overcomes the selectivity issues of the continuous sweat rate sensing scheme discussed above. By constructing a sensor architecture that considers sudden changes in impedance rather than impedance magnitude directly, we can isolate the effect of sweat volume to measure sweat rate with new selectivity. This isolation is enabled because physiological sweat ion changes occur over minutes, so dramatic changes in impedance that occur over seconds can accurately be ascribed to a new electrode gate being crossed, signifying the distance sweat has traveled for direct, accurate conversion to sweat rate.

To increase the frequency at which discrete sweat rate measurements can be made, more interdigitated electrode gates can be patterned for the serpentine channel to cross over. Expanding on this idea and combining architectures from the continuous and discrete sensing schemes, an updated sweat electrode architecture can be used with interdigitated electrode gates projecting into the channel from spiraling electrode backbones. The spacing between gates can be easily reduced
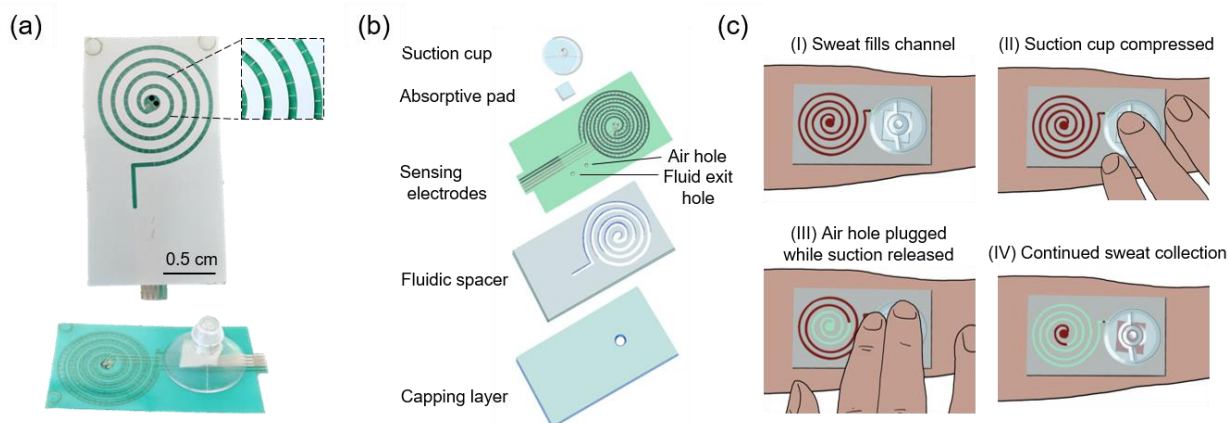

Figure 6. Prototype resettable microfluidic with suction pump for periodic sweat withdrawal. (a) The microfluidic has a spiraling microchannel with sweat rate electrode backbones on either side and interdigitated electrode gates that protrude into the channel. (b) Expansion of the layers of the microfluidic patch, with laser-cut fluidic channel and capping layer used to realize a collection well opening and an enclosed channel. Two exit holes are situated at the end of the channel, once for air to exit through during suction cup depression, and a second for sweat to be withdrawn through beneath the suction cup. (c) Prototype procedure for manually activating suction-based sweat withdrawal.

to increase the frequency of discrete sweat rate measurements. This pattern is depicted in **Figure 5** along with benchtop testing to demonstrate how discrete sweat rate measurement is performed.

3.4 Resettable microfluidics for prolonged sensor operating life

A limitation of both the continuous and discrete sweat rate sensing schemes is that sweat rate measurement can only continue as long as there is still available empty volume along the microchannel for the accumulating sweat front to advance into. Once the microchannel is filled, the admittance response plateaus in both sensing modalities. Fresh sweat can continue entering the device, pushing old sweat out of the exit hole at the end of the microchannel, but the rate of secretion can no longer be tracked. The microchannel holding capacity can be enhanced by increasing the channel length or the cross-sectional area. However, a very long channel can result in a large patch that is obtrusive to wear. A large cross-sectional area causes the sweat front to move slowly through the channel, increasing the time between each electrode gate crossing and limiting how frequently sweat rate measurements can be made. A narrow channel and an overall consolidated patch footprint are desirable but limit the volume capacity of the microfluidic.

A solution to this limitation is to introduce resettability into the sensing patch, whereby accumulated sweat can be periodically withdrawn from the device to create room for fresh sweat to newly cover the sweat rate electrodes or electrode gates. A simple demonstration of this idea is shown in **Figure 6**, in which a manually activated suction cup behaves as a negative pressure pump to draw sweat out of the channel. The microfluidic sensing patch is designed to have two exit holes, with the suction cup placed over the second. When the suction cup is depressed, air is
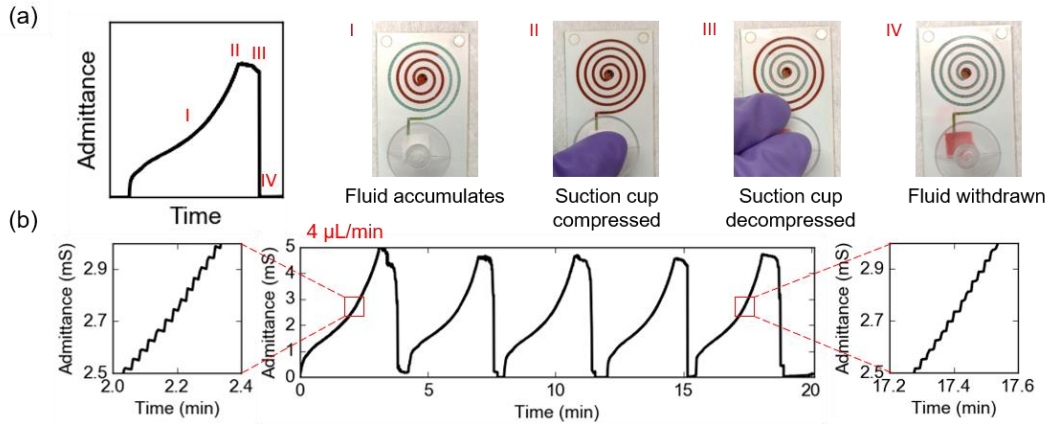

Figure 7. Recovery and repeatability of the sweat rate sensor signal upon multiple resets. (a) Schematic of how the measured signal increases as fluid accumulates in the microchannel before falling back to baseline levels when fluid is withdrawn. Red-dyed PBS buffer solution is used for visualization. (b) A device tested with PBS buffer solution injected in at 4 µL/min shows fairly reproducible step responses of the admittance signal over 5 resets. The step response can be processed to provide a measurement of flow rate.

ejected through the first exit hole to ensure sweat is not pushed backwards into the device. The user then blocks the first exit hole with one finger while decompressing the suction cup, drawing sweat out of the channel and into the region under the cup, where an absorptive pad can be placed to create a waste reservoir.

Figure 7 shows how the sweat rate electrode admittance response recovers back to baseline levels and repeatably increases again each time sweat is withdrawn to allow new sweat to enter the device, emphasizing that this scheme represents an effective simple starting point for realizing resettability. Going forward, a holding enclosure can be 3D printed and attached to the patch to hold the suction cup in place while still allowing it to depress and decompress for ease of actuation during on-body use. A filtering material that allows air to be pushed through but not liquids (such as Temish sheets produced by Nitto) can be overlayed over the air exit hole so that the hole need not be manually blocked during suction cup decompression. Ultimately, electronics and actuators can be included to automatically initiate sweat withdrawal periodically or once the channel is detected to be filled for fully automated resettability. This remains to be realized in future work.

3.5 Methods

3.5.1 Roll-to-roll fabrication of microfluidic patches

PET substrate (Melinex ST506 125 µm) was run at a speed of 2 m/min through ovens with a length of 4 m and heated to 140 °C. R2R printing on the primed PET included printing of (I) underlying silver electrodes, (II) carbon electrodes, (III) dielectric polymer layer, and (IV) upper spiral silver electrodes. The silver electrode head for electrochemical sensing is 1 mm in diameter while the carbon electrode head is 1.5 mm in diameter. The sweat rate sensor's silver electrode lines are 500 µm wide and spaced 300 µm apart. Alignment between printed layers was monitored by a camera module. Silver and carbon layers were cured in ovens while the dielectric layer was UV-cured. Materials and processing parameters used during R2R fabrication are listed in Table S1. The microfluidic contains a collection reservoir 5 mm in diameter and a channel that is 150 mm long with a cross-section of 180 um by 900 µm to contain a total volume of 24.3 uL. In this work, double sided adhesive tape (3M 9965) was used as the microfluidic layer. The cover sheet designed to enclose the microfluidic channel was formed from polyester film (3M 9984). After R2R processing, the sensing electrode layer, microfluidic adhesive, and cover sheet were cut by UV laser. Laser system (Elas) was equipped with a camera module to align laser beam with the alignment marks. Finally, the electrochemical sensors comprising sensing layer, microfluidic layer and cover lid were manually assembled as illustrated in Figure 1c.

Printing of the spiral Ag electrodes onto the thick dielectric layer required modifications to the printing tools and layer design/layout compared to when ink is printed directly onto smooth plastic substrate or over thinner printed layers. In order to achieve reliable and good ink transfer onto the dielectric layer, coarser screens with higher ink transfer but poorer resolution were used. As a result, the spiral lines have comparatively larger spacing and line widths. Resistance of the lower and upper printed Ag lines was measured by a stop-and-go characterization system with a 4-probe measurement unit (National Instruments PXI-4072).

3.5.2 Off-body sweat glucose analysis

For off-body sweat glucose measurement, 10 µL of collected sweat was injected onto the sensor surface and the current response recorded by benchtop electrochemical measurement instruments. Following measurement in sweat, a large volume of glucose stock solution (~ 1mL) was introduced to overwhelm the glucose contribution from the small sweat volume. Small volumes of high concentration glucose stock solution were successively injected to calibrate each sensor individually and then to back-calculate the glucose concentration indicated by the original current response to sweat.

3.5.3 On-body sweat analysis using the microfluidic patch

On-body human trials were carried out at the University of California, Berkeley in compliance with human research protocols (CPHS 2014-08-6636) and (CPHS 2015-05-7578) approved by the Berkeley Institutional Review Board (IRB). Iontophoresis trials were performed

using the ELITech Group Macroduct sweat collection system. Iontophoresis current application was conducted on the forearm for 5 min and the microfluidic patch attached immediately after. Blood glucose measurements were performed using commercial test kits (FreeStyle Precision Neo blood glucose meter and test strips) before and after sweat collection or on-body sensing. A new sweat patch was used per trial. Sensors in the patch were calibrated after removal from the subject's body, with identical protocol as off-body sensor calibration. For the sweat-to-blood glucose correlation study, subjects performed overnight fasting before their trials. Real-time sweat compositions and secretion rates were recorded using a custom-developed printed circuit board (PCB) reported earlier by our group in (36). The PCB contains on-site signal conditioning, analysis, and wireless data transmission to a mobile phone for real-time readout of the measured sweat analysis. Sweat rate and composition data obtained during on-body measurements were filtered in Matlab using the Hampel identifier.

3.5.4 Sweat glucose measurement using high performance liquid chromatography

Sweat samples were analyzed using high performance anion exchange chromatography with pulsed amperometric detection (HPAEC-PAD) on a Dionex ICS-5000 system (Thermofisher Scientific). Samples were injected (10 µL) and glucose was separated from all other sweat components on a Dionex CarboPAC PA-20 HPAEC column (length: 150 mm, inner diameter: 3mm, particle size: 6.5 µm) with an in-line column guard (length: 30 mm, inner diameter: 3mm, particle size: 6.5 µm) using an isocratic method (15 minutes, 0.010 M NaOH). The flow rate was set at 400 µL/min. The column was cleaned with 0.200 M NaOH (5 minutes) and re-equilibrated in 0.01 M NaOH (15 minutes) after each run. The column compartment was maintained at 30°C and the detector compartment at 25°C. Solvents were prepared using Milli-Q grade ultrapure water (resistivity >18.2 MΩ•cm at 25°C) and NaOH (50% w/w NaOH, Certified Grade, Fisher Scientific). A calibration curve was generated from the peak area of glucose standards with known concentrations (5–40 µM). All data was processed using Chromeleon Chromatography Data System software (version 7.1).

3.5.5 Fabrication of PDMS-based serpentine microfluidic patch

The electrodes were patterned on PET substrate through photolithography Shipley Micoposit S1818 photoresist) followed by evaporation of Cr/Au layers (30/80 nm). A 600 nm Parylene-C insulation layer was then deposited using SCS Labcoter 2 Parylene Deposition System. Then, the patterned device on PET substrate was treated with O_2 plasma and APTES, successively prior to bonding to the PDMS microfluidic. The microfluidic channel was made using the template method. The serpentine mold was prepared with SU-8 photoresist (2075, MicroChem) through photolithography on a silicon wafer. PDMS was homogeneously mixed at 10:1 weight % ratio of base:curing agent and degassed under vacuum for 1 hour. Degassed PDMS was poured onto the patterned SU-8 mold and cured for 1 hour at 90 °C. The cured PDMS microfluidic was peeled from the silicon wafer after cooling down. The inlet and outlet holes were punched out before the molded PDMS was treated with O2 plasma and bonded to the APTES-treated PET substrate.

3.5.6 Flow rate measurements for discrete sweat rate sensing devices

The admittance signals of the sweat rate sensors were acquired using Keysight E4980AL LCR meters, at acquisition frequency of 1kHz with 0.5 V amplitude. Controlled flow rate experiments were carried out using Harvard Apparatus PHD 2000 Syringe Pump.

3.6 References

(1) Baker, L. B. Sweating Rate and Sweat Sodium Concentration in Athletes: A Review of Methodology and Intra/Interindividual Variability. *Sports Med* **2017**, *47* (Suppl 1), 111–128. https://doi.org/10.1007/s40279-017-0691-5.

(2) Baker, L. B.; Ungaro, C. T.; Sopeña, B. C.; Nuccio, R. P.; Reimel, A. J.; Carter, J. M.; Stofan, J. R.; Barnes, K. A. Body Map of Regional vs. Whole Body Sweating Rate and Sweat Electrolyte Concentrations in Men and Women during Moderate Exercise-Heat Stress. *Journal of Applied Physiology* **2018**, *124* (5), 1304–1318. https://doi.org/10.1152/japplphysiol.00867.2017.

(3) Buono, M. J.; Verity, L. S. Cholinergic-Induced Sweat Rate during Hypo- and Hyperglycemia. *Clinical Kinesiology: Journal of the American Kinesiotherapy Association* **2004**, *58* (1), 11–13.

(4) Convertino, V. A. Heart Rate and Sweat Rate Responses Associated with Exercise-Induced Hypervolemia. *Medicine & Science in Sports & Exercise 1983* **1983**, *15* (1), 77–82.

(5) Foster, K. G.; Hey, E. N.; O'Connell, B. Sweat Function in Babies with Defects of Central Nervous System. *Arch Dis Child* **1971**, *46* (248), 444–451.

(6) Nyein, H. Y. Y.; Tai, L.-C.; Ngo, Q. P.; Chao, M.; Zhang, G. B.; Gao, W.; Bariya, M.; Bullock, J.; Kim, H.; Fahad, H. M.; Javey, A. A Wearable Microfluidic Sensing Patch for Dynamic Sweat Secretion Analysis. *ACS Sens.* **2018**, *3* (5), 944–952. https://doi.org/10.1021/acssensors.7b00961.

(7) Bariya, M.; Shahpar, Z.; Park, H.; Sun, J.; Jung, Y.; Gao, W.; Nyein, H. Y. Y.; Liaw, T. S.; Tai, L.-C.; Ngo, Q. P.; Chao, M.; Zhao, Y.; Hettick, M.; Cho, G.; Javey, A. Roll-to-Roll Gravure Printed Electrochemical Sensors for Wearable and Medical Devices. *ACS Nano* **2018**, *12* (7), 6978–6987. https://doi.org/10.1021/acsnano.8b02505.

(8) Bariya, M.; Nyein, H. Y. Y.; Javey, A. Wearable Sweat Sensors. *Nature Electronics* **2018**, *1* (3), 160–171. https://doi.org/10.1038/s41928-018-0043-y.

(9) Organization, W. H. Definition, Diagnosis and Classification of Diabetes Mellitus and Its Complications : Report of a WHO Consultation. Part 1, Diagnosis and Classification of Diabetes Mellitus. **1999**.

(10) Jajack, A.; Brothers, M.; Kasting, G.; Heikenfeld, J. Enhancing Glucose Flux into Sweat by Increasing Paracellular Permeability of the Sweat Gland. *PLoS One* **2018**, *13* (7). https://doi.org/10.1371/journal.pone.0200009.

(11) Gao, W.; Emaminejad, S.; Nyein, H. Y. Y.; Challa, S.; Chen, K.; Peck, A.; Fahad, H. M.; Ota, H.; Shiraki, H.; Kiriya, D.; Lien, D.-H.; Brooks, G. A.; Davis, R. W.; Javey, A. Fully Integrated Wearable Sensor Arrays for Multiplexed *in Situ* Perspiration Analysis. *Nature* **2016**, *529* (7587), nature16521. https://doi.org/10.1038/nature16521.

3.7 Appendix

3.7.1 Figure S1: High Performance liquid chromatography (HPLC) analysis of sweat samples and comparison with sweat sensor response.
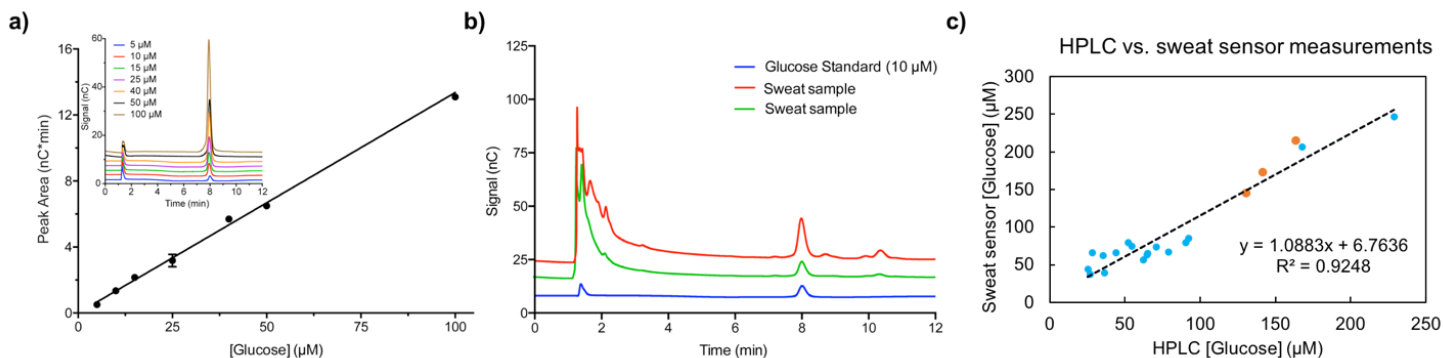

Figure S1. Comparison of sweat glucose sensor response with high performance liquid chromatography (HPLC). a) HPLC glucose standard curve with linear fit $y = 0.113x + 0.020$ and $R^2 = 0.994$. Error bars represent one standard deviation of the mean (n = 3). Inset: HPAEC-PAD chromatograms of glucose standards. Glucose elutes at 8.1 minutes. Chromatograms are vertically offset for clarity. b) Representative HPAEC-PAD chromatograms of sweat samples showing glucose peaks, compared with glucose standard. Chromatograms are offset for clarity. c) Correlation between glucose measured by HPLC and using sweat sensors for 21 sweat samples. Orange points indicate sweat samples spiked with small volume of concentrated glucose stock solution.

3.7.2 Figure S2: Comparison and correlation of blood glucose measured by blood glucose meter, sweat measured by HPLC and the sweat glucose sensors.
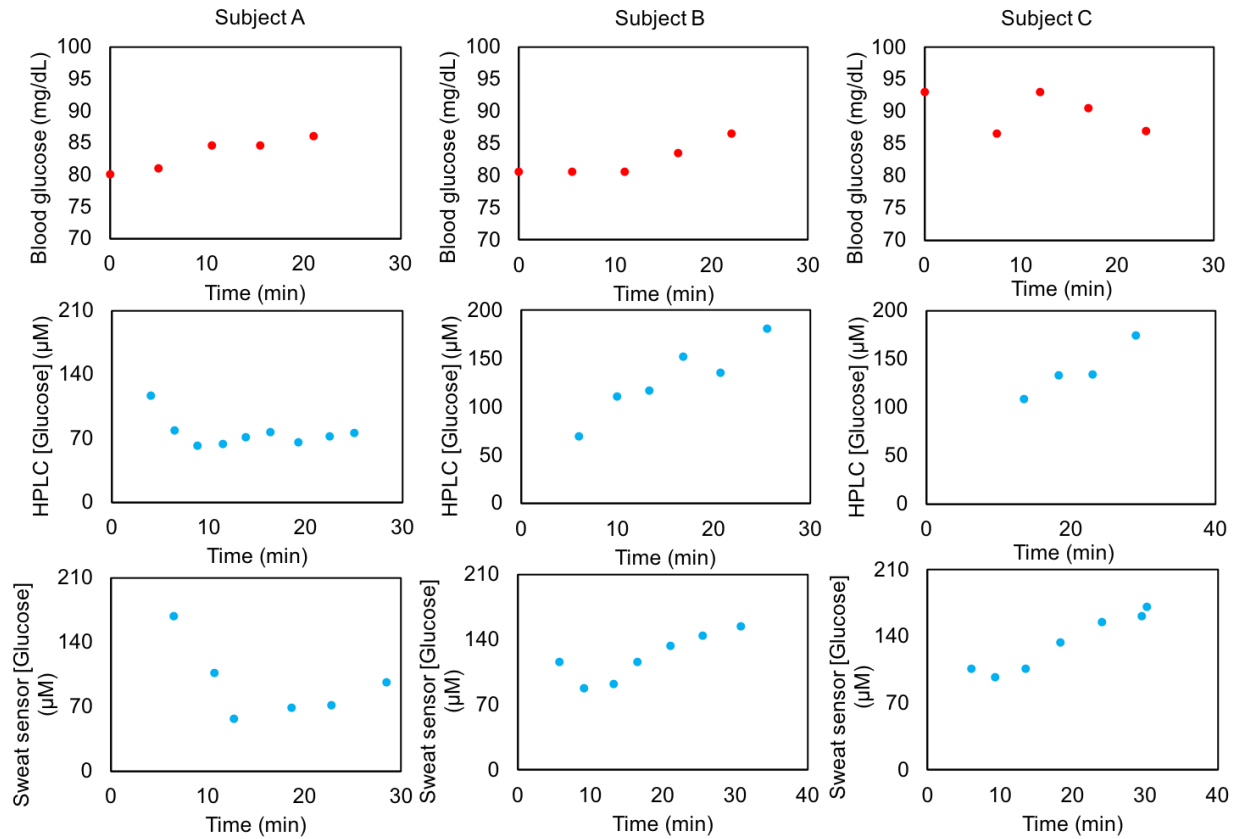

Figure S2. Fasting blood glucose levels and sweat glucose levels measured by HPLC and sweat sensors. Each column corresponds to a distinct subject. The blood glucose levels and HPLC sweat glucose levels were measured in the same trial. Sweat measured with HPLC (second row) comes from a different trial than sweat tested on the sensors (third row). Subject A is the same individual as the subject in Figure 5 (c).

3.7.3 Blood glucose measurements for population studies.

Table S1. Blood glucose measurements for population studies. Because of strip-to-strip variations in glucometer systems, two blood glucose strip measurements (BG 1 and BG 2) are made and averaged (Avg. BG) for each trial or sub-trial reported in the main paper. Healthy and diabetic subjects refer to subjects recorded for Figure 2(d) and (e).

Trial	BG 1	BG 2	Avg. BG
Figure 5(c) trials	85	85	85
	80	82	81
	80	84	82
	83	83	83
	126	132	129
	114	114	114
	108	110	109
	120	112	116
Figure 5(b) trials	119	121	120
	140	120	130
	133	125	129
	127	129	128
Figure 5(a) trials	85	85	85
	78	80	79
	127	143	135
	123	115	119

Trial	BG 1	BG 2	Avg. BG
Healthy subjects	99	103	101
	122	115	118.5
	99	102	100.5
	108	112	110
	87	88	87.5
	142	143	142.5
	80	83	81.5
	115	100	107.5
	93	93	93
	98	96	97
	84	90	87
	97	96	96.5
	86	79	82.5
	90	92	91
	97	101	99
	90	91	90.5
	78	80	79
	91	81	86
	92	95	93.5
	93	95	94
	93	97	95
	90	95	92.5
	88	90	89
	88	90	89
	100	96	98

Trial	BG 1	BG 2	Avg. BG
Diabetic subjects	147	135	141
	115	132	123.5
	87	80	83.5
	212	194	203
	127	119	123
	209	163	186
	104	109	106.5
	108	100	104
	237	208	222.5
	245	226	235.5
	256	251	253.5
	245	239	242
	248	236	242
	140	144	142.5
	150	145	147.5
	167	161	164
	135	162	148.5
	181	176	178.5
	176	165	170.5
	144	142	143
	134	141	137.5
	168	183	175.5
	183	160	171.5
	106	97	101.5
	102	101	101.5
	207	215	211
	215	226	220.5
	155	177	166
	183	199	191
	199	179	189
	106	103	104.5
	103	103	103
	104	106	105
	96	119	107.5
	127	152	139.5

Chapter 4: Glove-based sensors for rapid analysis of sweat at rest

The following chapter has been previously published in a similar format, and is reprinted and/or adapted with permission from the following work:

M. Bariya[*], L. Li[*], R. Ghattamaneni, C. H. Ahn, H. Y. Y. Nyein, L.-C. Tai, A. Javey. Glove-Based Sensors for Multimodal Monitoring of Natural Sweat. *Sci. Adv.* **2020**, *6*(35), eabb8308.

*These authors contributed equally.

4.1 Introduction

In recent years, a variety of sweat sensors have been developed to monitor biomarkers for athletic and health monitoring applications amidst a wider movement to determine what non-invasively and continuously accessible biofluids, including tears and saliva, can indicate about the physiological state of the body (1-15). Common to these platforms is a need for active sweat stimulation, either through exercise, iontophoretic/chemical stimulation, or heat treatment. Outside of a controlled laboratory environment, active stimulation poses practical limitations for widespread and routine sweat sensor use. Not only is it inconvenient to have to exercise or enter a sauna to obtain sensor measurements, this may be physically impossible for certain user groups including patients and the elderly. Local iontophoretic stimulation poses its own challenges, including decreased sweating rates after repeated current application and concerns regarding local skin burning. Practically, sweat sensors must be able to access sweat autonomously without damaging the skin and must be compatible with routine activity, giving physiological insights without impeding user lifestyles. Natural thermoregulatory sweating, or background sweat that individuals continually secrete to micro-regulate body temperature without active stimulation, is a much more promising method for non-invasive and convenient biomarker access (16). Sweat is naturally secreted even during sedentary or routine activities like sleeping, sitting, and walking. Secretion rates are typically relatively low (~0.1 nL/min/gland versus over 1 nL/min/glad for exercise) but involve large-area sweat generation that produces nontrivial volumes of sweat overall (17-19). Further, lower sweat rates reduce dilution of secreted analytes, better preserving equilibrium correlations between biomarkers in the sweat gland and those in surrounding interstitial fluid or blood (18, 20, 21). In this way, natural sweat could potentially provide better insight into the molecular state of the body compared to actively stimulated sweat.

While reducing sensor size (and thereby sample volume requirements) is one way in which sweat analysis can be supported by natural sweating, other methods include targeting body regions with particularly high sweat gland densities and inhibiting evaporation – a particular concern for distributed and low-rate sweat generation. Here we present glove-based sensing platforms to analyze sweat naturally secreted on the hands and fingers during sedentary or routine activity (**Fig. 1A**). The fingertips, palm, and back of hand have some of the highest sweat gland densities on the
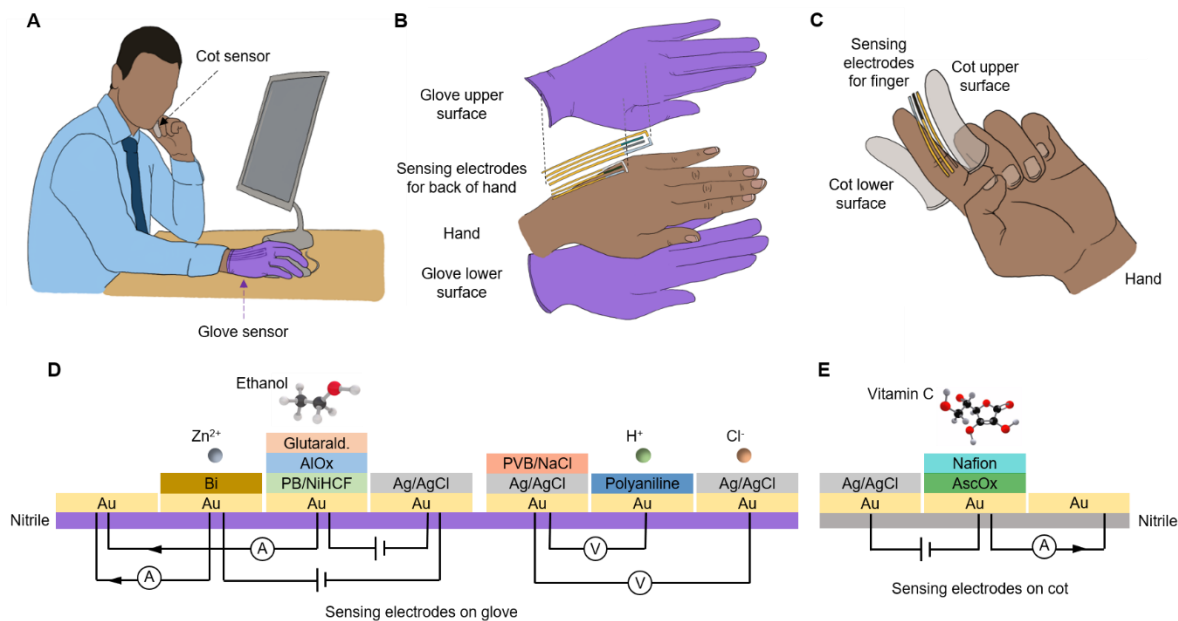
Fig. 1 Glove-based analytics for natural sweat analysis. (**A**) Glove-based sensors including functionalized gloves and cots allow natural sweat analysis during sedentary and routine activity without active sweat stimulation. (**B**) Electrochemical sensors can be fabricated on versatile glove positions such as the back of the hand to target high sweat rate sites. The glove's nitrile material crucially protects against evaporation for rapid sweat accumulation. (**C**) Nitrile cots can be functionalized to target sweat gland-rich fingertips while offering a condensed form factor. (**D**) Cross-sectional schematic of the sensing layers and measurement schemes for zinc, ethanol, pH, and chloride sensors functionalized on a nitrile glove, and (**E**) vitamin C sensor functionalized on a nitrile cot.

body and therefore present attractive sites for accessing natural sweat (22, 23). Gloves made of moisture-impermeable nitrile efficiently accumulate natural sweat by dramatically limiting evaporation (**Fig. S1** in the Appendix of this chapter), enabling 100's of µL to be collected within half an hour while at rest. These large volumes could be harnessed for traditional off-body sweat analysis, already constituting a much more efficient and convenient method of sweat collection compared to exercise or chemical stimulation. Going a step further, sensors can be directly functionalized onto the inner surfaces of nitrile gloves (**Fig. 1B**) and finger cots (**Fig. 1C**) to allow *in situ* natural sweat analysis of analytes including ions, heavy metals, xenobiotics and nutrients (**Fig. 1D-E**), without the need for miniaturized sensors. By taking advantage of a familiar and easy-to-wear form factor, glove-based analytics prioritize user comfort and convenience, providing a promising route to making sweat sensing routine for real-world application.

Electrodes can be fabricated in versatile patterns and locations on the inner surfaces of nitrile gloves and finger cots by simply defining electrode areas using a shadow mask and then evaporating conductive electrode materials. As a demonstration, we pattern gold and bismuth electrodes on the glove surface contacting the back of the hand – a region with particularly high

sweating rates – and functionalize them into electrochemical sensors for sweat alcohol, zinc, chloride, and pH (24). We similarly fabricate a 3-electrode system within nitrile finger cots to be selective for vitamin C. We verify the mechanical robustness of these platforms against the strains of on-body wear, and demonstrate them for representative natural sweat monitoring applications including using a sequence of gloves and cots to compare sweat and blood alcohol dynamics and to conduct multi-day tracking of sweat vitamin C levels following vitamin supplement intake. In this way we extract semi-continuous, dynamic information about sweat xenobiotics that are found to cohere with pre-existing understandings of their metabolism and excretion in sweat, validating that each glove provides a faithful snapshot of sweat composition at that time. Single-point measurements obtained with individual gloves are therefore promising for rapidly gauging the physiological state of the body in applications where the presence of a chemical beyond a threshold level in sweat is noteworthy (such as for determining dangerous heavy metal exposure), or when a sweat analyte has an established correlation with blood (such as when monitoring alcohol levels). As these measurements can be obtained in just 30 min at rest, the functionalized gloves and cots represent a valuable advantage over other sweat sensor systems that rely on exercise or chemical stimulation to access sweat or that demand lengthy accumulation periods at low sweat rates. Overall, the presented sensors are found to be effective platforms for collecting and analyzing natural sweat during resting and routine activities, and relatively comfortable, inexpensive alternatives to the costly and invasive tests associated with traditional hospital-based monitoring of human health and physiological status.

4.2 Characterization of sweat gland densities and resting sweat rates on the hand

High sweat gland densities on the hand make it a promising site for sweat analysis compared to other body locations traditionally used for wearable sweat devices. Sweat gland densities are characterized for 5 subjects (2 females, 3 males) on the index finger pad, palm, back of hand, wrist, forearm, forehead, and back of neck (**Fig. 2A**). Impressions of the glands are obtained using an iodine-soaked paper patch for the latter two regions to accommodate their firm yet curved skin surfaces, while the remaining regions are spotted with bromophenol dye to directly color the sweat glands as discussed in the Methods section (25, 26). Sweat glands are counted from these images for each subject and body site, revealing that the 5 subjects have average sweat gland densities of 441, 318, 290, 212, 171, 208, and 110 glands/cm^2 on the finger, palm, back of hand, wrist, forearm, forehead, and back of neck respectively (**Fig. 2B**). The significantly higher densities on the hand surfaces cohere with previous findings and make them valuable target areas for sweat capture and analysis (22). By creating an enclosed region where secreted sweat is protected against evaporation, gloves and finger cots can capitalize on these high sweat gland density sites to rapidly accumulate sweat for analysis.

To characterize how much natural sweat is obtained for analysis with these platforms, subjects are recruited to wear nitrile gloves and cots during sedentary or routine activity at ambient temperatures. The volume of sweat accumulated after 30 min is identified by weighing the glove before being worn and after the 30 min of wear, and calculating the difference. In addition, to

Fig. 2 Comparative sweat gland densities across body locations. (**A**) Sweat glands are imaged with bromophenol blue on the finger, palm, back of hand, wrist, and forearm. Sweat glands on the forehead and neck are imaged by imprinting onto iodine patches. Blue squares indicate locations of the sampled densities. Sweat gland images share the same scale. (**B**) Sweat gland densities are found by counting glands in the images from (a) across body sites for 5 subjects. A unique color is used for each subject. Photo credit: Mallika Bariya, UC Berkeley.

capture any residual sweat left on the hand surface after glove removal, an absorptive pad is swiped across the hand immediately after glove removal and also weighed, faithfully recovering residual sweat to within a few µL due to the rapid collection time under 1 min. This study is first conducted for the nitrile glove platform (**Fig. 3A**). For 12 subjects (6 females, 6 males) sitting at ambient indoor workplace temperatures between 65 and 70 °F for half an hour, up to several 100 µL of sweat is accumulated (**Fig. 3B**). The males produce an average of 475 µL of sweat on each hand while the females produce an average of 180 µL of sweat on each hand, consistent with known gender-based differences (27). Since the nitrile gloves do not directly laminate the skin to suffocate any sweat glands, and do not produce significant local heating to raise core temperature or overcome the body's natural radiative and insensible evaporation mechanisms of heat loss, these large accumulated volumes are due to the body's natural thermoregulatory sweating process combined with low evaporation through the nitrile material (28, 29). Similar volumetric secretion can be expected even without wearing gloves, but in this case the exposed sweat rapidly evaporates and obscures the high volumes actually produced, leaving insufficient sweat for analysis. Creating an evaporation barrier is therefore a critical aspect of the glove-based sensing platform.

To more closely investigate factors that impact natural sweating rates, the influence of activity level and temperature are probed for a smaller subgroup of subjects. 6 subjects (3 females, 3 males) wear nitrile glove for 30 min at ambient workplace temperature and at different activity levels, including sitting, standing, and light walking at under 75 steps per min (**Fig. 3C**). Sweating rates in general are seen to increase with more strenuous activity, with some subjects nearly doubling their total secreted sweat volumes when standing compared to sitting. Next, activity level is kept fixed while the temperature-dependence of secreted sweat volume is studied for the 6 sitting subjects (**Fig. 3D**). Sweating rates generally increase with temperature, though more dramatically for some subjects than others. The exact relationship between activity, ambient temperature, and accumulated sweat volume will depend on a host of other subject-dependent factors including
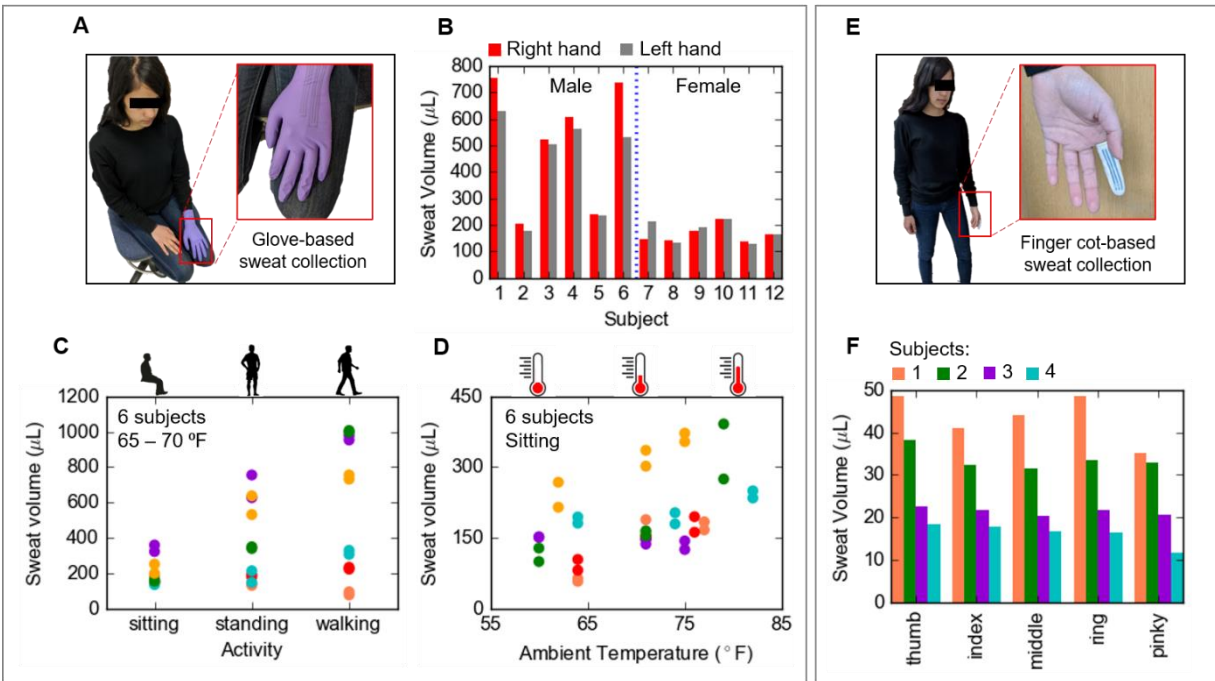
Fig. 3 Sweat volumes accumulated during routine activity. (**A**) Sweat accumulated in glove during 30 min of routine activity for panels b-d. (**B**) Sweat collected from right (red) and left (grey) gloved hands for 12 subjects (6 male, 6 female) while sitting at ambient indoor conditions near 65 °F. (**C**) Sweat accumulated from 6 subjects at different activity levels (3 male, 3 female) shows generally increasing sweat rate with activity level. (**D**) Sweat accumulated from 6 subjects over a range of ambient temperatures while sitting indicates a rough increase in sweat rate with temperature. (**E**) Sweat accumulated in finger cot for 30 min for panel f. (**F**) Finger cots worn on each finger for 4 subjects (2 males and 2 females, each designated a different color) show slightly higher sweat volume accumulated on the thumb and slightly lower volume on the pinky, roughly scaling with finger surface area. Photo credit: Lu Li, UC Berkeley.

body mass, hydration level, metabolic rate, etc., but overall, we find that for most subjects undergoing routine activity at ambient temperatures, large volumes of sweat in excess of 100 µL are available for natural sweat analysis within 30 min of glove-based accumulation (30).

Instead of wearing an entire glove, a nitrile cot worn on a single finger can provide an even less intrusive platform for natural sweat analysis while still accumulating significant volumes of sweat due to the exceptionally high sweat gland densities on the fingers (**Fig. 3E**). To gauge how much sweat can be accumulated on each finger, 4 subjects (2 females, 2 males) wear a cot on each finger for 30 min at ambient indoor temperature near 65 °F while sitting (**Fig. 3F**). Tens of µL are secreted on each finger, with the thumb offering slightly higher volumes due to its larger surface area, and the pinky secreting slightly less. Sweat contributions from the fingers constitute 30-50% of the overall sweat obtained from the hands of these subjects. These volumes are sufficient for sensing at least one biomarker without requiring miniaturized electrodes, and indicate that any finger would be a suitable choice for natural sweat analysis.

4.3 Electrochemical sensor performance on nitrile glove surfaces

Electrodes can be fabricated at diverse sites within the glove due to the simple shadow mask and evaporation-based patterning scheme, and customized to target any analyte of choice. While electrodes can be patterned to access the fingertips, palm, or multiple sites, for demonstration purposes we fabricate sensors on the glove surface contacting the back of the hand (**Fig. 4A**) as this site is particularly immune to bending strains that might arise during hand motions. We create two demonstrative sets of electrochemical sensors – the first set executes xenobiotic sensing of alcohol and zinc using two working electrodes and shared reference and counter electrodes, while the second conducts electrolyte monitoring of sweat chloride and pH using two working electrodes and a shared reference. An alcohol sensor is included in the glove because sweat alcohol has been shown to correlate with blood alcohol concentration (BAC), potentially allowing the glove sensor to inform users of their body's alcohol absorption and warn against overdose (10, 31). Zinc is targeted because heavy metals are commonly excreted in sweat, and while Zn is important for the immune system it can be harmful when body levels are consistently elevated (32, 33). Sweat chloride and pH can together indicate the body's acid/base balance, and are further targeted to demonstrate that the glove sensor can support diverse electrochemical detection schemes (34, 35). The xenobiotic array comprises of four gold electrodes – two are functionalized with alcohol oxidase enzyme and bismuth metal respectively to target alcohol and zinc, one is an exposed gold counter electrode, and the last is developed into an Ag/AgCl reference electrode. The electrolyte array has three gold electrodes – one is coated in Ag/AgCl ink to target chloride ions, the second has electrodeposited polyaniline to measure pH, and the third becomes a PVB reference electrode. Cross-sectional schematics of the functional layers are shown in **Fig. 1D**. The alcohol, Zn, pH, and chloride sensors fabricated on the glove are calibrated in **Fig. 4B-E**. The alcohol sensor is sequentially tested in 1xPBS buffer solutions of 0, 0.25, 0.5, 0.75, 1, 1.5, 2.5, 4.5, and 6.5 mM ethanol (**Fig. 4B**), with calibration curve inset, and shown to have an even wider range of sensitive detection in **Fig. S2** (in the Appendix of this chapter) to accommodate expected sweat alcohol levels (36, 37). The zinc sensor is tested in 0.001 M acetate buffer solutions of 0, 400, 800, 1200, 1600, and 2000 µg/L zinc (**Fig. 4C**), giving a linear calibration curve. Note that the signal magnitudes obtained from the alcohol and zinc sensors scale with working electrode area and are therefore subject to the particular geometry of the patterned electrodes. The pH sensor is sequentially tested in McIlvaine buffer solutions of pH 4, 5, 6, and 7 which encompass the typical pH range of sweat (**Fig. 4D**), giving nearly ideal Nernstian sensitivity at 60.3 mV/pH. The chloride sensor is tested in 1xPBS buffer solutions at 25, 50, 100, and 200 mM NaCl, also giving near-Nernstian sensitivity at an average of 15.9 mV/doubling in chloride concentration or 52.8 mV/decade (**Fig. 4E**). Overall, the performance of these sensors on the glove's soft, nitrile substrate is similar to what has been previously demonstrated by our group and others on more planar, rigid PET (3, 10, 33, 38).

Given the smaller surface area available, a single 3-electrode system for xenobiotic sensing of vitamin C is patterned on the nitrile cot to analyze natural sweat on the fingertips (**Fig. 4F**). The
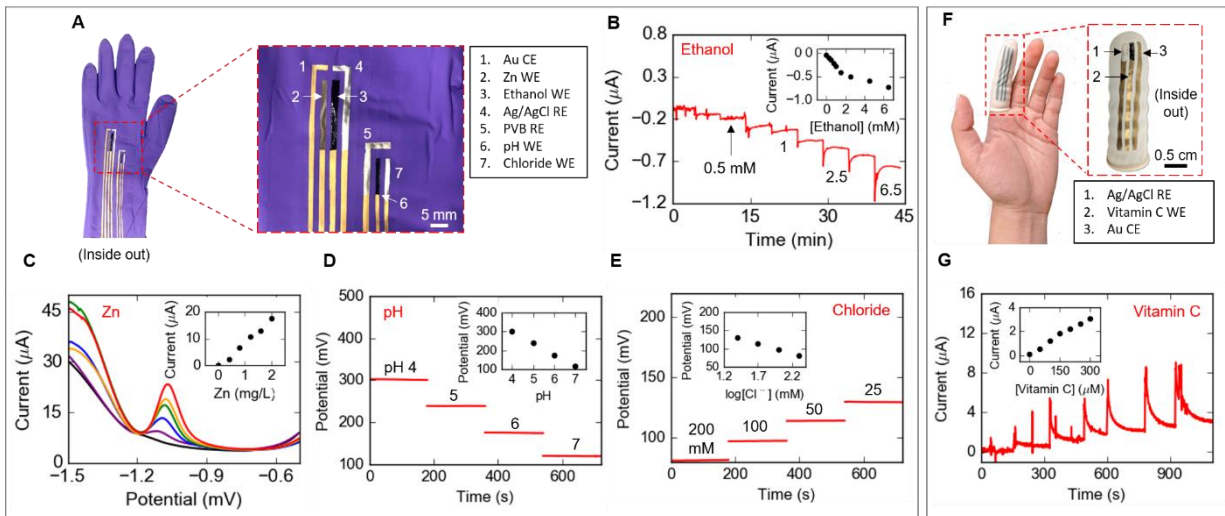
Fig. 4 Electrochemical characterization of glove-based sensors. (A) Gold electrodes are evaporated on the inner glove surface and functionalized with sensing layers to target zinc, ethanol, pH, and chloride ions in sweat. Calibration curves in buffer solutions of different analyte concentrations are shown for **(B)** ethanol, **(C)** Zn, **(D)** pH, and **(E)** chloride. **(F)** 3-electrode system on the inside of a finger cot comprises of evaporated gold functionalized with sensing materials to detect vitamin C. **(G)** Calibration curve of vitamin C sensor in buffer solutions. Photo credit: Lu Li, UC Berkeley.

electrode heads are centered on the finger pad, a location that is relatively immune to strains associated with bending of the fingers. Vitamin C is chosen to target as its presence in sweat could indicate levels of daily intake or vitamin deficiency (39, 40). This array has with three underlying gold electrodes – one is coated in Ag/AgCl ink to be the reference, the second is functionalized with ascorbate oxidase to interact with vitamin C, and the third is left as bare gold to act as the counter electrode. A cross-sectional schematic of the electrode layers is shown in **Fig. 1E**. This system's response to vitamin C concentrations between 0 and 300 µM in increments of 50 µM is linear and highly sensitive (**Fig. 4G**), with similar performance compared to our group's previous demonstrations on PET (41).

4.4 Electro-mechanical robustness of glove-based sensors

As the sensors' electrical signals are relayed through long electrode lines that end at the wrist of the glove or edge of the cot where a measurement system can be connected, it is important that the electrodes are mechanically robust when the glove-based platforms are worn. Specifically, the sensors' underlying electrodes must have recoverable conductivity or resistance values when the platforms are deformed during motion and wear, as deformation is expected to occur along the extended electrode length but not so much at the very head of the electrode where the sensing membranes are located. To characterize this electro-mechanical stability, we pattern an 8 cm long electrode line on the nitrile substrate and calculate its resistance between 0 and 15% strain (**Fig. 5A**), a conservatively broad range given that strains during on-body wear are typically under 2%
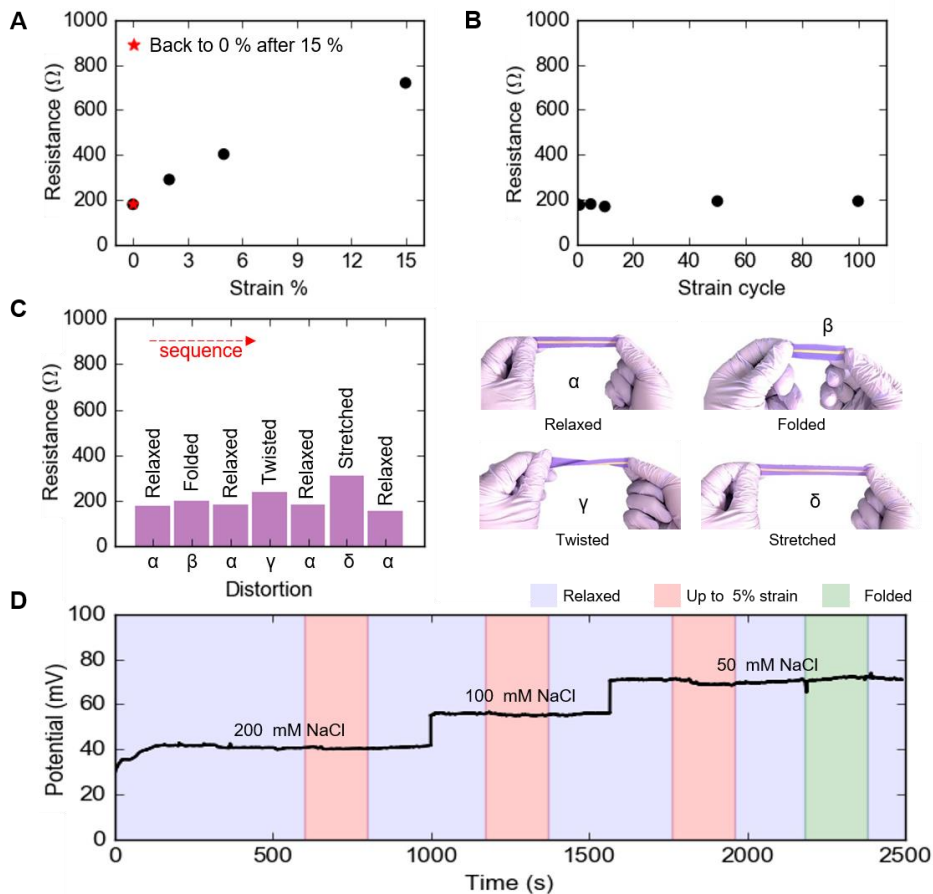
70

Fig. 5 Characterization of electrode robustness under mechanical deformation. (A) Resistance of an 8 cm evaporated Au electrode on the nitrile glove is measured between 0 and 15% strain. Red star shows relaxed electrode resistance once 15 % strain is removed. **(B)** Resistance of the 8 cm electrode is measured at the relaxed state after 0, 1, 5, 10, 20, 50, and 100 cycles of 2 % applied strain, showing the electrode consistently recovers even after multiple distortions. **(C)** The electrode is exposed to a series of distortions including folding, twisting, and stretching (via 2% strain). Stretching/strain has the most pronounced impact on the electrode resistance during the distortion, but the electrode closely recovers to the original resistance of its relaxed state after each deformation. **(D)** A representative chloride sensor on the glove is calibrated while strained and folded. The distortions do not significantly impact the sensor signal. Photo credit: Lu Li, UC Berkeley.

for electrodes contacting the back of the hand (as seen in **Fig. S3** in the Appendix of this chapter) (42). Note that resistance changes associated with deformation during insertion of the hand into the glove is ignored as this is a one-time operation that can be conducted carefully and introduces negligible baseline strains, and any residual resistance changes are accounted for during calibration post-on-body testing. While the electrode deformation produces a change in resistance during strain, the resistance goes back to its original, pre-strained value when relaxed back to 0% strain as indicated by the red star. This highlights the recoverability of the system, indicating that the

electrode does not crack or undergo permanent damage when stretched. This behavior arises because the nitrile glove is originally extended over the sample holder during gold evaporation, forming a percolating network of Au clusters or ligaments, rough surface features that connect over fine cracks to ensure electrical conductivity of the relaxed nitrile as demonstrated previously for other thin metal films on elastomeric substrates (43, 44). This structure is formed due to a large mismatch of thermal expansion coefficients of the elastomer and metal during evaporation. When the substrate is strained, the metal network accommodates by twisting or deflecting out of the plane but remains bonded to the soft substrate, effectively deforming elastically without fatigue and keeping the Au microstructure intact. Once the substrate is relaxed and strain withdrawn, the network of clusters returns to its original state and the original electrical resistance of the electrode is recovered. Overall, contact between the clusters changes but does not sever under strain as the rough gold surface elastically deforms, and recovers back to the original rough contact when the nitrile is relaxed. This explanation is supported by optical microscope images of the gold electrode layer before, during, and after 15 % strain in **Fig. S4** (in the Appendix of this chapter). Note that at rest, conductivity of the approximately 150 nm thick evaporated Au film is measured to be around $8x10^5$ S/m, around two orders lower than that of bulk Au as expected for thin films. Resistance rather than conductivity values are reported for the electrode under deformation in **Fig. 5** since information on the exact change in geometric structure of the electrode under deformation is not available. Further, note that strains and resistance measurements are applied and obtained with the nitrile substrates in their final right-side-out configurations that match the state of functionalized gloves or cots ready for on-body wear, indicating that these platforms are mechanically robust for use.

To ensure that the electrode layer recovers even after numerous deformation cycles, the same electrode is put through 100 cycles of 2% strain with resistance measured during the relaxed state after each cycle (**Fig. 5B**). The measured resistance values after 0, 1, 5, 10, 50, and 100 cycles is 180, 176, 180, 169, 193, and 193 Ω respectively, essentially identical values given variation of around ± 10 Ω with the multimeter measurement system. Extended strain testing with more complex twisting and bending cycles and higher tensile strain bears this robustness out further in **Fig. S5** (in the Appendix of this chapter).

While the electrode does not break under strain and recovers to its original state, the change in resistance during deformation seen in **Fig. 5A** could potentially causing noisy sensor signals when the hands or fingers are moved. To characterize how severe the change in resistance is from different types of deformation, we probe the electrode under relaxed, folded, twisted, and stretched (or 2% strained) states in **Fig. 5C**. The resistance recovers when the electrode is relaxed after each type of deformation, indicating mechanical robustness. Further, strain is seen to affect the electrode resistance the most severely. To gauge whether this change in electrode resistance impacts the final sensor signal, we functionalize the electrode into a representative chloride sensor and calibrate it under relaxed and strained states (**Fig. 5D**), with a potentiometric sensor chosen for testing here since enzymatic sensors with nanotextured mediator layers have sensor signals limited

by the amount and accessibility of enzyme, which quickly stabilizes under strain as studied in previous works (45-47). **Fig. 5D** shows that strains on the order of those expected during routine hand motions (as quantified in **Fig. S3** in the Appendix) do not have a significant impact on the overall sensor response – for example, no noticeable shifts in overall potential occur during transitions from relaxed to strained states. This indicates that signal contributions from the sensing layers' interaction with the target analyte dominate over changes in the electrode wire resistance. Overall, these electro-mechanical tests highlight that the evaporated Au electrodes do not crack under the glove deformations typically undergone during on-body wear, have recoverable characteristics, and do not ultimately constitute a significant source of noise in the glove sensor response.

4.5 On-body sweat analysis during resting and routine activities with glove-based sensors

Having established the electrochemical and electro-mechanical robustness of the glove-based sensing platforms, we next conduct representative human subject trials for sweat alcohol and vitamin C monitoring to demonstrate the flexibility and versatility of glove-based analytics for natural sweat monitoring. In each trial, the subject wears a functionalized glove or cot platform for around 30 min at a time to accumulate sufficient natural sweat during sedentary or routine activity, with on-body measurements made at the end of this period once enough sweat is accumulated on the electrodes. Each glove or cot gives a single measurement that represents the average sweat analyte concentration over that 30 min interval, since sweat is continually accumulated and mixed during that time. By wearing multiple gloves or cots in sequence, the overarching dynamics of the target sweat analyte can be captured through single-glove snapshots of the sweat composition in time, allowing semi real-time tracking of the overarching analyte dynamics. The first demonstrative trial tracks natural sweat ethanol content over 6 hours after a subject introduces alcohol into the body by drinking wine (**Fig. 6A**). A series of 10 gloves are used with around 30 min accumulation time per glove and 10-15 min in between to wipe down the hand and don a new glove. In parallel, a breathalyzer is used to simultaneously track BAC levels for comparison. Based on the alcohol content of the wine, around 45 mL of alcohol are consumed in total over a 15 min period ending at time demarcated 0 min (**Fig. 6B(i)**). Following this intake, BAC level steeply rises to a maximum of 0.13 before slowing dropping over the next 6 hours (**Fig. 6B(ii)**). With a delay of around 30 to 40 min compared to BAC levels, sweat alcohol content elevates to a maximum of 5.6 mM before tapering down to 2.1 mM at the end of this measurement period (**Fig. 6B(iii)**). Integrity of these measurements is established via comparison of a subset of on-body and off-body sensor measurements in **Table S1** in the Appendix. Note that each glove's sweat measurement marked by a red point in **Fig. 6B(iii)** is centered in the middle of the 30 min period of wear, since the measurement reflects the average sweat composition over that period. Based on the overarching trend, the sweat alcohol content is expected to keep decreasing towards the pre-intake level denoted by the first glove/red point. This sweat trend is similar to what has previously been reported, underscoring the effectiveness of the glove-based sensor for dynamic monitoring (7).
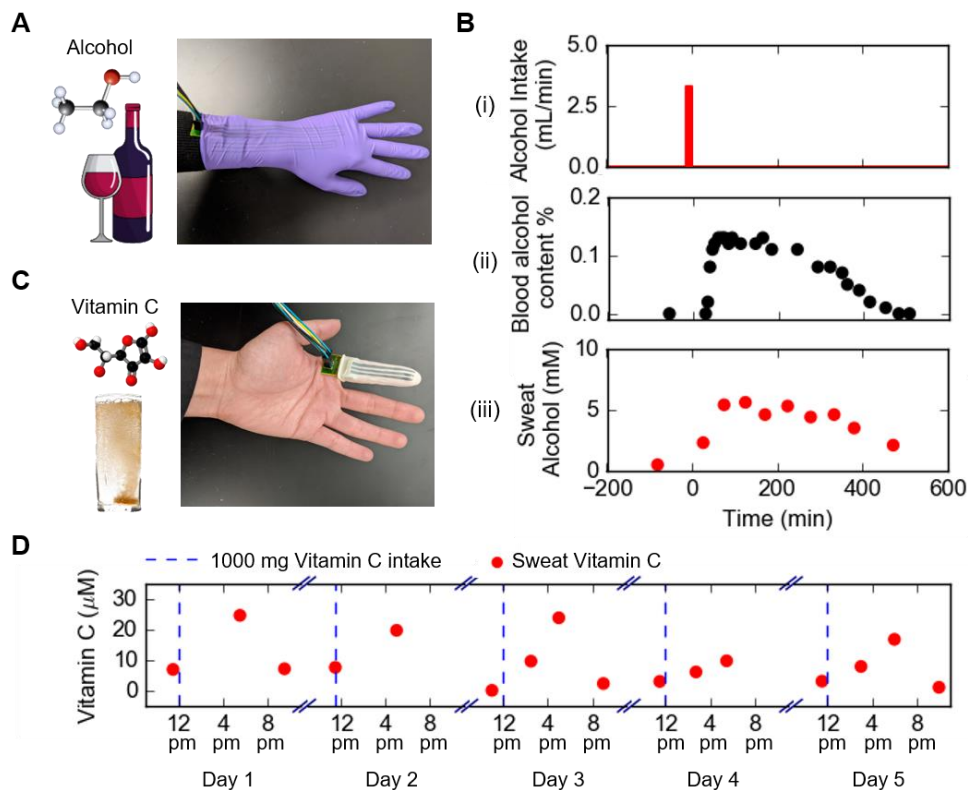
Fig. 6 On-body multi-glove study of natural sweat analyte dynamics. (A) Subject introduces alcohol into the body by drinking wine, and subsequent excretion of alcohol in natural sweat is studies using the glove-based sensing platform. **(B)** Time 0 indicates when alcohol consumption is finished. (i) Alcohol intake versus time. (ii) Blood alcohol concentration (BAC) as measured by a breathalyzer. (iii) Natural sweat alcohol concentration is tracked over a 6-hour period using 10 gloves, with each glove providing an average alcohol concentration measurement for the 30 min time period over which it was worn. Each glove's measurement is indicated by a red point at the end of the 30 min interval. **(C)** Subject consumes 1000 mg vitamin C dissolved in water each day for 5 days, and the resulting vitamin C that emerges in natural sweat is tracked using functionalized finger cots. **(D)** Natural sweat vitamin C concentration is plotted with red dots (each representing a measurement by one finger cot 30 min of accumulated sweat) over 5 days. Daily peaking behavior demonstrates the competing adsorption and metabolism mechanisms typical of xenobiotics in the body. Dashed blue lines indicate time of vitamin C intake. Photo credit: Lu Li, UC Berkeley.

A second trial explores how natural sweat can provide insight into the body's adsorption and metabolism of vitamin C following supplement intake. A subject consumes 1000 mg vitamin C dissolved in water at 12 pm each day for 5 days, and vitamin C concentration in subsequent naturally secreted sweat is measured using the functionalized finger cot platform (**Fig. 6C**). Each day, two to four finger cots are worn for 30 min at different time points, with the sweat measurement from each glove marked by a red point centered within its corresponding 30 min interval in **Fig. 6D**. As seen in **Fig. 6D**, sweat vitamin C content is lowest (less than 10 µM) right

before intake (denoted by a vertical dashed blue line) and is elevated 4 to 5 hours later before dropping down overnight. This peaking trend is common of xenobiotics in the body, where concentrations originally rise as the chemical is absorbed before lowering as is it metabolized and removed from the system (40, 48-50). Integrity of the on-body vitamin C measurements is borne out by comparing a set of on-body and off-body sample measurements in **Table S1**. Note that more frequent finger cot application could be used to capture the exact vitamin C peaking point in sweat. Further, note that sweat vitamin C levels seem to vary day-to-day, which could be due to variation in the subject's daily diet and hydration status amidst other factors that impact physiological status.

While the alcohol and vitamin C trials demonstrate that glove-based analytics for dynamic monitoring of natural sweat biomarkers are an effective alternative to conventional hospital or home healthcare devices, these trials primarily validate the accuracy and reliability of this platform. The true advantage of glove-based sensors over other sweat sensing systems is how conveniently and rapidly they can be used for individual biomarker measurements. Rapid single-point assessment of physiological status could be done using just one glove or cot, as demonstrated by measuring the sweat pH and chloride levels of 3 subjects to gauge their acid/base balance in **Fig. S6** in the Appendix. Overall, the glove-based sensing platforms are effective and versatile for natural sweat analysis, with simple electrode fabrication schemes that allow custom, application-specific sensors to be patterned and functionalized. To make electrode fabrication repeatable and scalable, stencils or laser-cut tape can be used in future to identically pattern electrodes on multiple gloves. Paper fluidics can be developed and incorporated in the gloves to gauge total secreted sweat volume and approximate sweat rate. Custom PCBs or ASIC units can be developed to attach to the electrode stems near the wrist of the glove or base of the cot, enabling autonomous signal extraction that would further promote this platform for routine sweat analysis. Going forward, glove-based analytics represents a valuable tool for performing physiological and correlation studies on natural sweat to better understand how sweat analysis can be used to probe the health and state of the body.

4.6 Conclusion

We present wearable sweat sensors with convenient glove-based form factors for rapid accumulation of natural thermoregulatory sweat without active sweat stimulation. This platform enables sweat sensing under routine and even sedentary activity towards making sweat-based biomarker monitoring practical for daily life. By targeting high sweat gland densities on the hand and inhibiting evaporation, glove and finger cot sensors allows accumulation of 100's of μL of natural sweat under an hour of wear, eliminating the need for highly miniaturized sensors to access natural sweat. We functionalize representative electrochemical sensor on the inner glove surface and conduct on-body measurements to demonstrate the ease and simplicity of glove-based analytics for tracking xenobiotic dynamics in sweat. Functionalized gloves and cots support versatile electrode placement and are electro-mechanically robust under the strains of on-body wear, retains the high level of performance typically associated with more rigid and planar substrates. Overall, the presented glove-based sensing platforms are an accessible, user-oriented

approach to natural sweat analysis and can be adapted for versatile health and physiological monitoring applications.

4.7 Methods

4.7.1 Fabrication of functionalized electrodes on the glove

A simple shadow mask is built and applied onto the glove's inside surface, keeping electrode areas open and covering the rest of the glove. E-beam evaporation is used to deposit 150 nm of Au, followed by a similar taping and evaporation procedure to deposit 300 nm Bi on the head of the zinc working electrode. For the alcohol sensor, electrodeposition of Au nanodendrites is followed by cyclic voltammetry to deposit 2 interdigitated layers each of Prussian Blue mediator and NiHCF stabilizer as demonstrated in previous work (4, 51). For a working electrode area of approximately 8 mm^2, 6 µL of alcohol oxidase enzyme solution (6.5 parts BSA to 13.5 parts AlOx) is drop-cast followed by 3 µL of 0.02% glutaraldehyde solution and allowed to dry overnight (solutions volumes are scaled with electrode area). The chloride sensor and Ag/AgCl reference electrode are fabricated by depositing Ag/AgCl conductive ink over the Au electrode heads, while the PVB reference involves deposition of a thick layer of PVB solution (saturated with NaCl) over Ag/AgCl ink as demonstrated in our previous work (3). The pH sensor is fabricated by electrodepositing polyaniline similar to our previous work (38). Vitamin C working electrode is functionalized by electrodepositing a solution of 0.02 M EDOT and 0.02 M LiClO$_4$ for 1 min at 1.1 V vs. Ag/AgCl reference. For a roughly 8 mm^2 electrode area, 5 µL of 2.5 mg mL^{-1} ascorbate oxidase dissolved in 1x PBS buffer was dropcast onto the electrode surface followed by 4 µL of 0.5% Nafion solution as demonstrated in our previous work (41). After electrochemical functionalization is complete, the glove or finger cot is turned right-side out before it is calibrated or used for on-body measurement. Note that this inverting process produces negligible change in the resistances of each electrode as indicated in Table S2.

4.7.2 Imaging sweat glands and characterizing their densities

Two methods were used to image sweat glands using bromophenol dye and iodine patches respectively as demonstrated in previous work (25, 26). Bromophenol blue was dissolved in pure acetone in a 5% w/v solution and then mixed with silicone in 1:1 volumetric ratio. The mixture was magnetically stirred at 25 °C until the acetone evaporated away and an orange solution was formed. The skin surface was washed and totally dried before the bromophenol dye was spread in a thin layer and allowed to react with moisture from the sweat gland, turning the orange dye blue in the sweat gland region within a few minutes. A photograph of the skin surface with a nearby ruler (for size calibration) was then captured for software analysis. The second method involved placing pads of paper in a sealed container (of roughly 1 L volume) with < 2 mg of solid iodine for 2 days, such that the paper was impregnated with iodine vapor. The pads were directly forced against the washed and dried skin surface for 5 seconds, transferring images of the sweat glands to the paper. A photograph of the iodine pad was then captured. Sweat gland density measurements were made by using ImageJ for both methods. An FFT bandpass filter followed by thresholding

was applied to each image to capture both small and large sweat glands in the analyzed area. The number of sweat glands was divided by the measurement area to give the sweat gland density. This process was repeated 3 times for each image and averaged to estimate the sweat gland density per body site.

4.7.3 Characterization of glove sensor response

Sensors fabricated on the glove electrodes were calibrated off-body using a sequence of buffer solutions prepared with known concentration. For chloride and pH sensor calibration, the sensors were conditioned in high concentration analyte solution (200 mM NaCl and McIlvaine buffer of pH 4 respectively) for 10 min before beginning calibration via open-circuit voltage measurement, and 1 min of stabilization time was used between solutions. Alcohol and vitamin C sensor calibrations were conducted via chronoamperometry at an applied potential of 0 V and 0.2 V respectively. For Zn heavy metal sensing, square wave anodic stripping voltammetry was used with 30 second pre-concentration at -1.5 V followed by stripping from -1.5 to -0.5 V.

4.7.4 On-body sweat analysis using the glove sensor

On-body human trials were carried out at the University of California, Berkeley in compliance with the human research protocol (CPHS 2014-08- 6636) approved by the Berkeley Institutional Review Board (IRB). Subjects washed their hands with soap and water and allowed them to totally dry before donning the glove sensors or finger cots. Glove sizes were chosen to comfortably fit the subjects' hands with a reasonable but not too tight seal near the wrist while ensuring a snug fit with good glove-to-skin contact. A paper pad was placed over the electrode heads to retain sweat cumulatively over the duration of wear and to electrochemically connect the working, reference, and counter systems without electrically contacting the skin. A protective barrier layer (Kapton or a 0.0005" thick PET insert) was used to cover the long electrode lines to prevent shorting and direct skin contact. The ends of the electrodes near the wrist portion of the glove or base of the finger cots were connected to a Gamry and/or CHI potentiostat for signal extraction. Sensor measurements were made once the glove had been worn for roughly 30 min to ensure accumulation of enough sweat to obtain reliable measurements. The sensors were calibrated before and after on-body data collection for accurate conversion of raw signals to concentration estimates. In future, calibration can be made more user friendly by introducing manually activated valves to release calibration solution, or by moving to automated fabrication to reduce inter-sensor variability.

4.8 References

1. J. Heikenfeld, A. Jajack, B. Feldman, S. W. Granger, S. Gaitonde, G. Begtrup, B. A. Katchman, Accessing analytes in biofluids for peripheral biochemical monitoring. *Nat. Biotechnol.* **37**, 407–419 (2019).
2. H. Lee, C. Song, Y. S. Hong, M. S. Kim, H. R. Cho, T. Kang, K. Shin, S. H. Choi, T. Hyeon, D. H. Kim, Wearable/disposable sweat-based glucose monitoring device with multistage transdermal drug delivery module. *Sci. Adv.* **3**, e1601314 (2017).

3. W. Gao, S. Emaminejad, H. Y. Y. Nyein, S. Challa, K. Chen, A. Peck, H. M. Fahad, H. Ota, H. Shiraki, D. Kiriya, D.-H. Lien, G. A. Brooks, R. W. Davis, A. Javey, Fully integrated wearable sensor arrays for multiplexed *in situ* perspiration analysis. *Nature* **529**, 509–514 (2016).

4. H. Y. Y. Nyein, M. Bariya, L. Kivimäki, S. Uusitalo, T. S. Liaw, E. Jansson, C. H. Ahn, J. A. Hangasky, J. Zhao, Y. Lin, T. Happonen, M. Chao, C. Liedert, Y. Zhao, L.-C. Tai, J. Hiltunen, A. Javey, Regional and correlative sweat analysis using high-throughput microfluidic sensing patches toward decoding sweat. *Sci. Adv.* **5**, eaaw9906 (2019).

5. M. Bariya, H. Y. Y. Nyein, A. Javey, Wearable sweat sensors. *Nat. Electron.* **1**, 160–171 (2018).

6. A. Koh, D. Kang, Y. Xue, S. Lee, R. M. Pielak, J. Kim, T. Hwang, S. Min, A. Banks, P. Bastien, M. C. Manco, L. Wang, K. R. Ammann, K.-I. Jang, P. Won, S. Han, R. Ghaffari, U. Paik, M. J. Slepian, G. Balooch, Y. Huang, J. A. Rogers, A soft, wearable microfluidic device for the capture, storage, and colorimetric sensing of sweat. *Sci. Transl. Med.* **8**, 366ra165 (2016).

7. J. Kim, I. Jeerapan, S. Imani, T. N. Cho, A. Bandodkar, S. Cinti, P. P. Mercier, J. Wang, Noninvasive Alcohol Monitoring Using a Wearable Tattoo-Based Iontophoretic-Biosensing System. *ACS Sens.* **1**, 1011-1019 (2016).

8. Z. Sonner, E. Wilder, T. Gaillard, G. Kasting, J. Heikenfeld, Integrated sudomotor axon reflex sweat stimulation for continuous sweat analyte analysis with individuals at rest. *Lab. Chip* **17**, 2550–2560 (2017).

9. Y. Yang, Y.Song, X. Bo, J. Min, O. S. Pak, L. Zhu, M. Wang, J. Tu, A. Kogan, H. Zhang, T. K. Hsiai, L. Zhaoping, W. Gao, A laser-engraved wearable sensor for sensitive detection of uric acid and tyrosine in sweat. *Nat. Biotechnol.* **38**, 217–224 (2020).

10. A. Hauke, P. Simmers, Y. R. Ojha, B. D. Cameron, R. Ballweg, T. Zhang, N. Twine, M. Brothers, E. Gomez, J. Heikenfeld, Complete validation of a continuous and blood-correlated sweat biosensing device with integrated sweat stimulation. *Lab. Chip* **18**, 3750–3759 (2018).

11. P. Simmers, S. K. Li, G. Kasting, J. Heikenfeld, Prolonged and localized sweat stimulation by iontophoretic delivery of the slowly-metabolized cholinergic agent carbachol. *J. Dermatol. Sci.* **89**, 40–51 (2018).

12. A. Martín, J. Kim, J. F. Kurniawan, J. R. Sempionatto, J. R. Moreto, G. Tang, A. S. Campbell, A. Shin, M. Y. Lee, X. Liu, J. Wang, Epidermal Microfluidic Electrochemical Detection System: Enhanced Sweat Sampling and Metabolite Detection. *ACS Sens.* **2**, 1860–1868 (2017).

13. A. Alizadeh, A.Burns, R. Lenigk, R. Gettings, J. Ashe, A. Porter, M. McCaul, R. Barrett, D. Diamond, P. White, P. Skeath, A wearable patch for continuous monitoring of sweat electrolytes during exertion. *Lab. Chip* **18**, 2632–2641 (2018).

14. Y. Zhang, H. Guo, S. B. Kim, Y. Wu, D. Ostojich, S. H. Park, X. Wang, Z. Weng, R. Li, A. J. Bandodkar, Y. Sekine, J. Choi, S. Quaggin, R. Ghaffari, J. A. Rogers, Passive sweat collection and colorimetric analysis of biomarkers relevant to kidney disorders using a soft microfluidic system. *Lab. Chip* **19**, 1545–1555 (2019).

15. A. J. Bandodkar, P. Gutruf, J. Choi, K. Lee, Y. Sekine, J. T. Reeder, W. J. Jeang, A. J. Aranyosi, S. P. Lee, J. B. Model, R. Ghaffari, C.-J. Su, J. P. Leshock, T. Ray, A. Verrillo, K. Thomas, V. Krishnamurthi, S. Han, J. Kim, S. Krishnan, T. Hang, J. A. Rogers, Battery-free, skin-interfaced microfluidic/electronic systems for simultaneous electrochemical, colorimetric, and volumetric analysis of sweat. *Sci. Adv.* **5,** eaav3294 (2019).

16. Y. Hu, C. Converse, M. C. Lyons, W. H. Hsu, Neural control of sweat secretion: a review. *Br. J. Dermatol.* **178**, 1246–1256 (2018).

17. S. Emaminejad, W. Gao, E. Wu, Z. A. Davies, H. Y. Y. Nyein, S. Challa, S. P. Ryan, H. M. Fahad, K. Chen, Z. Shahpar, S. Talebi, C. Milla, A. Javey, R. W. Davis, Autonomous sweat

extraction and analysis applied to cystic fibrosis and glucose monitoring using a fully integrated wearable platform. *Proc. Natl. Acad. Sci.* **114**, 4625–4630 (2017).

18. Z. Sonner, E. Wilder, J. Heikenfeld, G. Kasting, F. Beyette, D. Swaile, F. Sherman, J. Joyce, J. Hagen, N. Kelley-Loughnane, R. Naik, The microfluidics of the eccrine sweat gland, including biomarker partitioning, transport, and biosensing implications. *Biomicrofluidics 9,* 031301 (2015).

19. S. Lin, B. Wang, Y. Zhao, R. Shih, X. Cheng, W. Yu, H. Hojaiji, H. Lin, C. Hoffman, D. Ly, J. Tan, Y. Chen, D. D. Carlo, C. Milla, S. Emaminejad, Natural Perspiration Sampling and in Situ Electrochemical Analysis with Hydrogel Micropatches for User-Identifiable and Wireless Chemo/Biosensing. *ACS Sens.* **5**, 93–102 (2020).

20. J. Kim, A. S. Campbell, B. E.-F. de Ávila, J. Wang, Wearable biosensors for healthcare monitoring. *Nat. Biotechnol.* **37**, 389–406 (2019).

21. A. Jajack, M. Brothers, G. Kasting, J. Heikenfeld, Enhancing glucose flux into sweat by increasing paracellular permeability of the sweat gland. *PLoS One, 13,* e0200009 (2018).

22. N. A. Taylor, C. A. Machado-Moreira, Regional variations in transepidermal water loss, eccrine sweat gland density, sweat secretion rates and electrolyte composition in resting and exercising humans. *Extreme Physiol. Med.* **2**, 4 (2013).

23. K. J. Collins, F. Sargent, J. S. Weiner, Excitation and depression of eccrine sweat glands by acetylcholine, acetyl-β-methylcholine and adrenaline. *J. Physiol.* **148**, 592–614 (1959).

24. J. S. Weiner, The regional distribution of sweating. *J. Physiol.* **104**, 32–40 (1945).

25. G. Tashiro, M. Wada, M. Sakurai, A Bromphenol Blue Method for Visualizing Sweat at the Openings of the Sweat Ducts**From the Physiological Laboratory, Tohoku University School of Medicine, Sendai, Japan. *J. Invest. Dermatol.* **36**, 3–4 (1961).

26. D. Gagnon, M. S. Ganio, R. A. I. Lucas, J. Pearson, C. G. Crandall, G. P. Kenny, Modified iodine-paper technique for the standardized determination of sweat gland activation. *J. Appl. Physiol.* **112**, 1419–1425 (2012).

27. P. U. Giacomoni, T. Mammone, M. Teri, Gender-linked differences in human skin. *J. Dermatol. Sci.* **55**, 144–149 (2009).

28. E. A. Arens, H. Zhang, The skin's role in human thermoregulation and comfort. (2006).

29. D. B. Frewin, J. A. Downey, Sweating-physiology and pathophysiology. *Aust. J. Dermatol.* **17**, 82-86 (1976).

30. E. H. Wissler, 'Sweating', in *Human Temperature Control: A Quantitative Approach* (ed. Wissler, E. H.) 197–237 (Springer, 2018).

31. M. J. Buono, Sweat ethanol concentrations are highly correlated with co-existing blood values in humans. *Exp. Physiol.* **84**, 401–404 (1999).

32. J. R. Cohn, E. A. Emmett, The excretion of trace metals in human sweat. *Ann. Clin. Lab. Sci.* **8**, 270–275 (1978).

33. W. Gao, H. Y. Y. Nyein, Z. Shahpar, H. M. Fahad, K. Chen, S. Emaminejad, Y. Gao, L.-C.Tai, H. Ota, E. Wu, J. Bullock, Y. Zeng, D.-H. Lien, A. Javey, Wearable Microsensor Array for Multiplexed Heavy Metal Monitoring of Body Fluids. *ACS Sens. 1,* 866-874 (2016).

34. E. H. Fishberg, W. Bierman, Acid-Base Balance in Sweat. *J. Biol. Chem.* **97**, 433–441 (1932).

35. M. J. Patterson, S. D. R. Galloway, M. A. Nimmo, Effect of induced metabolic alkalosis on sweat composition in men. *Acta Physiol. Scand.* **174**, 41–46 (2002).

36. A. Bhide, S. Muthukumar, A. Saini, S. Prasad, Simultaneous lancet-free monitoring of alcohol and glucose from low-volumes of perspired human sweat. *Scientific reports* **8**, 1-11 (2018).

37. M. Gamella, S. Campuzano, J. Manso, G. González de Rivera, F. López-Colino, A. J. Reviejo, J. M. Pingarrón, A novel non-invasive electrochemical biosensing device for in situ determination of the alcohol content in blood by monitoring ethanol in sweat. *Anal. Chim. Acta* **806**, 1-7 (2014).

38. H. Y. Y. Nyein, W. Gao, Z. Shahpar, S. Emaminejad, S. Challa, K. Chen, H. M. Fahad, L.-C. Tai, H. Ota, R. W. Davis, A. Javey, A Wearable Electrochemical Platform for Noninvasive Simultaneous Monitoring of Ca^{2+} and pH. *ACS Nano* **10**, 7216-7224 (2016).

39. J. B. Shields, B. C. Johnson, T. S. Hamilton, H. H. Mitchell, The excretion of ascorbic acid and dehydroascorbic acid in sweat and urine under different environmental conditions. *J. Biol. Chem.* **161**, 351–356 (1945).

40. S. J. Padayatty, H. Sun, Y. Wang, H. D. Riordan, S. M. Hewitt, A. Katz, R. A. Wesley, M. Levine, Vitamin C Pharmacokinetics: Implications for Oral and Intravenous Use. *Ann. Intern. Med.* **140**, 533-537 (2004).

41. J. Zhao, H. Y. Y. Nyein, L. Hou, Y. Lin, M. Bariya, C. H. Ahn, W. Ji, A. Javey, Wearable Nutrition Tracker. Manuscript submitted for publication.

42. M. D. Fisher, V. R. Reddy, F. M. Williams, K. Y. Lin, J. G. Thacker, R. F. Edlich, Biomechanical performance of powder-free examination gloves. *J. Emerg. Med.* **17**, 1011–1018 (1999).

43. S. P. Lacour, D. Chan, S. Wagner, T. Li, Z. Suo, Mechanisms of reversible stretchability of thin metal films on elastomeric substrates. *Appl. Phys. Lett.* **88**, 204103 (2006).

44. T. Adrega, S. P. Lacour, Stretchable gold conductors embedded in PDMS and patterned by photolithography: fabrication and electromechanical characterization. *J Micromech Microeng* **20**, 055025 (2010).

45. J. R. Windmiller, J. Wang, Wearable electrochemical sensors and biosensors: a review. *Electroanalysis* **25**, 29-46 (2013).

46. M.-C. Chuang, Y.-L. Yang, T.-F. Tseng, T. Chou, S.-L. Lou, J. Wang, Flexible thick-film glucose biosensor: influence of mechanical bending on the performance. *Talanta* **81**, 15-19 (2010).

47. J. Cai, K. Cizek, B. Long, K. McAferty, C. G. Campbell, D. R. Allee, B. D. Vogt, J. L. Belle, J. Wang, Flexible thick-film electrochemical sensors: impact of mechanical bending and stress on the electrochemical behavior. *Sensor Actuat B-Chem* **137**, 379-385 (2009).

48. L. Z. Benet, D. Kroetz, L. Sheiner, J. Hardman, L. Limbird, Pharmacokinetics: the dynamics of drug absorption, distribution, metabolism, and elimination. *Goodman and Gilman's the pharmacological basis of therapeutics*, 3-27 (1996).

49. L.-C. Tai, W. Gao, M. Chao, M. Bariya, Q. P. Ngo, Z. Shahpar, H. Y. Y. Nyein, H. Park, J. Sun, Y. Jung, E. Wu, H. M. Fahad, D.-H. Lien, H. Ota, G. Cho, A. Javey, Methylxanthine Drug Monitoring with Wearable Sweat Sensors. *Adv. Mater.* **30**, 1707442 (2018).

50. L.-C. Tai, T. S. Liaw, Y. Lin, H. Y. Y. Nyein, M. Bariya, W. Ji, M. Hettick, C. Zhao, J. Zhao, L. Hou, Z. Yuan, Z. Fan, A. Javey, Wearable Sweat Band for Noninvasive Levodopa Monitoring. *Nano Lett.* **19**, 6346–6351 (2019).

51. Y. Lin, M. Bariya, H. Y. Y. Nyein, L. Kivimäki, S. Uusitalo, E. Jansson, W. Ji, Z. Yuan, T. Happonen, C. Liedert, J. Hiltunen, Z. Fan, A. Javey, Porous Enzymatic Membrane for Nanotextured Glucose Sweat Sensors with High Stability toward Reliable Noninvasive Health Monitoring. *Adv. Funct. Mater.* **29**, 1902521 (2019).

4.9 Appendix

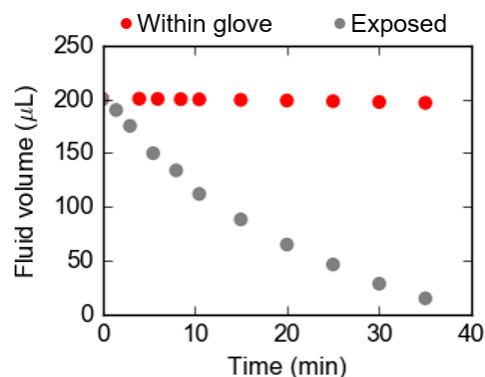### 4.9.1 Fig. S1: Comparative evaporation of exposed and gloved fluid.

Fig. S1. Comparative evaporation of exposed and gloved fluid. Nitrile gloves inhibit evaporation from the hand surface, as demonstrated by comparing the remaining fluid volume on two pads soaked with 200 µL PBS buffer, one within the glove (red) and one exposed (grey) at ambient conditions of 46% relative humidity and 71°F.

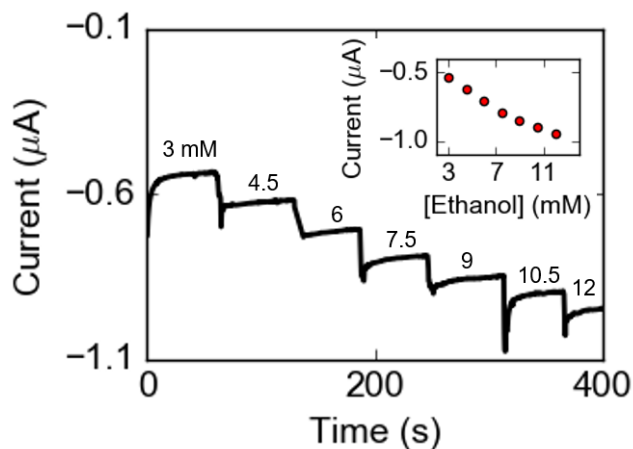### 4.9.2 Fig. S2: Extended calibration of the alcohol sensor beyond the linear range.

Fig. S2. Extended calibration of the alcohol sensor beyond the linear range shown in Fig.4B. The sensor is sequentially tested in PBS buffer solutions with ethanol concentrations of 3, 4.5, 6, 7.5, 9, 10.5, and 12 mM and returns a sensitive current change in response.

4.9.3 Fig. S3: Maximum strain on back-of-hand comparing relaxed and fisted gloves.

A

B

line length:
5.1 mm

line length:
5.2 mm

Relaxed hand

Fisted hand
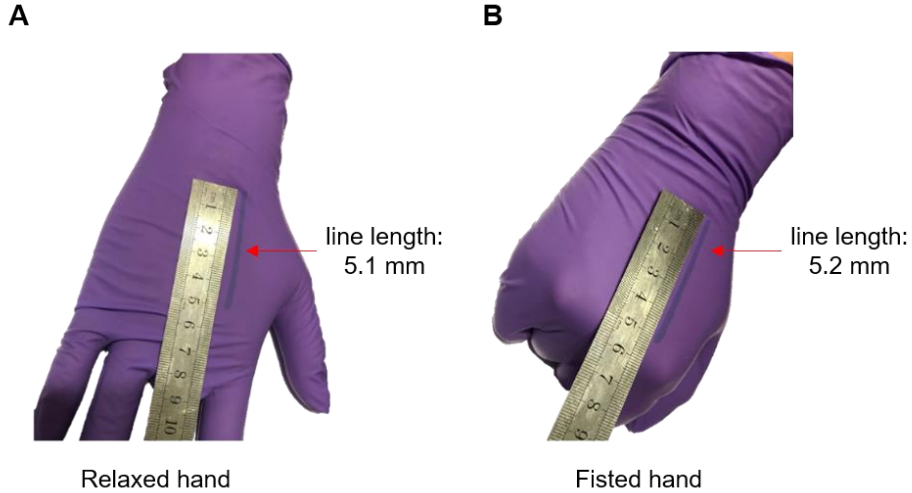
Fig. S3. To determine the maximum strains incurred by electrodes positioned on the back of the hand during routine on-body motions, a line is drawn on the glove and its length compared during extreme cases **(A)** when the hand and glove are relaxed, and **(B)** when the hand is fisted, a motion that produces the most extreme stretching of the glove at the back of the hand. The line length changes from 5.1 mm to 5.2 mm, translating to 2.0 % strain. Photo credit: Lu Li, UC Berkeley.

4.9.4 Fig. S4: Optical characterization of gold electrode under strain.

(a)

(b)

(c)

300 µm

300 µm

300 µm
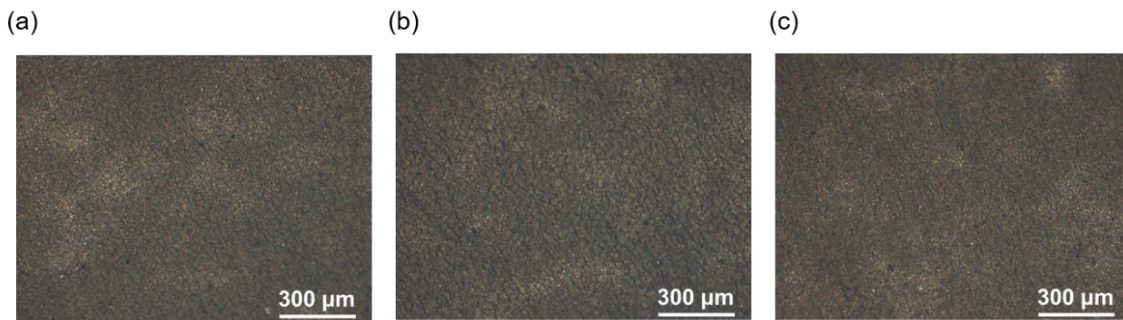
Fig. S4. Optical characterization of gold electrode under strain. Light microscope image of a representative surface section of the gold electrode evaporated on the glove at **(a)** 0% strain before stretching, **(b)** 15% strain while stretched, and **(c)** 0% strain when relaxed back. The gold electrode does not crack under this extreme stretching, demonstrating the robustness of the patterned electrode/glove system for on-body wear.
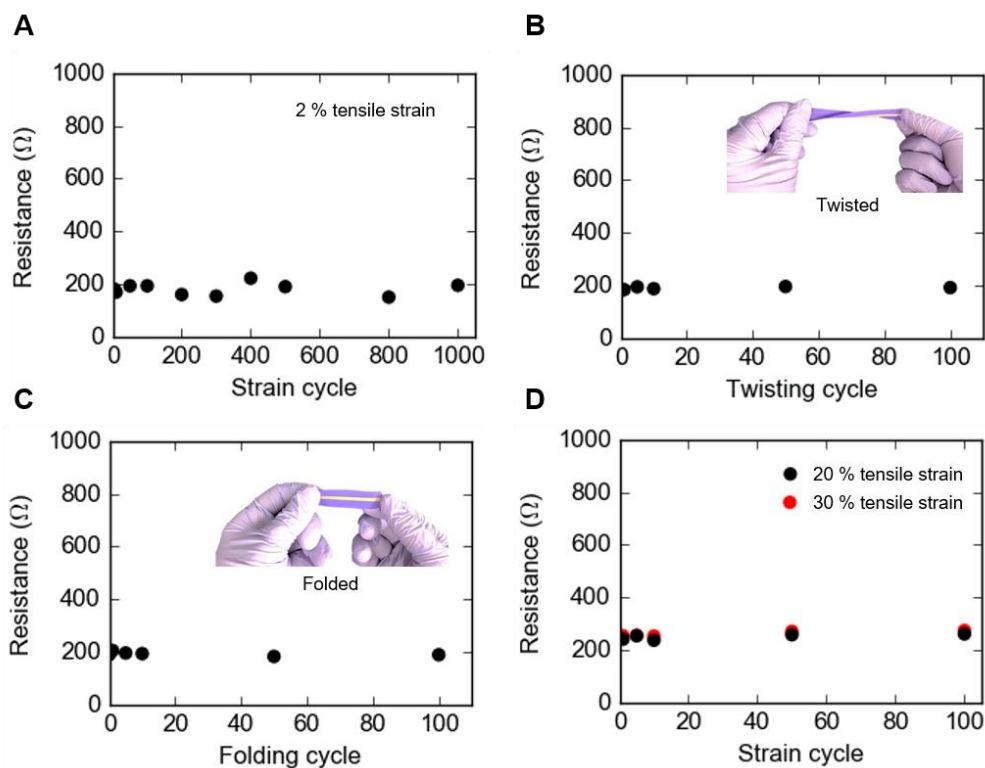
Fig. S5. Resistance of an 8 cm electrode patterned onto the nitrile glove is measured at the relaxed state over **(A)** 1000 cycles of stretching at 2 % strain, **(B)** 100 cycles of twisting, **(C)** 100 cycles of folding, and **(D)** 100 cycles of stretching at 20 % (black) and 30 % (red) tensile strain. For each type of distortion, the resistance returns to its original level, indicating the absence of permanent damage to the electrode during mechanical wear. Photo credit: Lu Li, UC Berkeley.

4.9.6 Fig. S6: Glove-based characterization of sweat pH and electrolyte content.
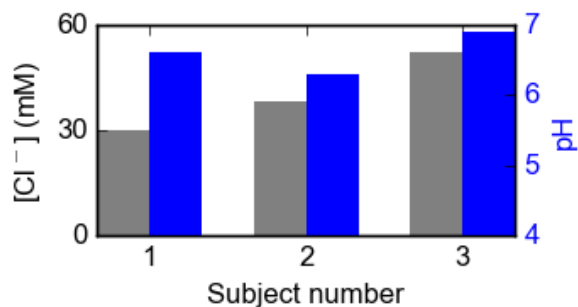
Fig. S6. Glove sensor worn for 30 min by 3 subjects to measure chloride and pH levels. Abnormal electrolyte or pH levels could indicate acid/base imbalances in the body that indicate a deeper health condition. Here, all three subjects have biomarker concentrations within the acceptable range for healthy subjects.

4.9.7 Table S1: Off-body verification of on-body alcohol and vitamin C measurements.

Ethanol		Vitamin C	
On-Body Measurement (mM)	Off-Body Measurement (mM)	On-Body Measurement (µM)	Off-Body Measurement (µM)
2.3	2.4	45.7	43.5
5.3	5.2	1.3	1.6
3.5	3.1	5.3	4.8

Table S1. To verify the integrity of on-body measurements by the alcohol and vitamin C sensors, three sweat samples are collected from the glove and tested off-body in parallel with on-body measurement. The concentration measurements are sufficiently close for all samples.

4.9.8 Table S2: Electrode resistances before and after glove is inverted for on-body use.

Electrode number	Resistance before inversion (Ω)	Resistance after inversion (Ω)
1	260	268
2	201	198
3	192	199
4	207	201
5	170	173
6	168	164
7	174	171

Table S2. Resistances of 7 sample electrodes measured when the glove is inside-out right after fabrication and then after the glove is inverted to its right-side-out, ready-to-wear state. The inversion process causes minimal baseline change in resistance.

Chapter 5: Microfluidic patch for continuous analysis of sweat at rest

The following chapter has been previously published in a similar format, and is reprinted and/or adapted with permission from the following works:

H. Y. Y. Nyein[*], M. Bariya[*], B. Tran, C. H. Ahn, B. J. Brown, W. Ji, N. Davis, A. Javey. A Wearable Patch for Continuous Analysis of Thermoregulatory Sweat at Rest. *Nat. Commun.* **2021**, *12*(1), 1-13.

* These authors contributed equally.

5.1 Introduction

The previous chapter presented glove-based platforms for rapid accumulation of sweat at rest, with each glove or finger cot providing a single measurement of a target analyte over the 30-minute duration of wear. While several gloves can be strung together in series to uncover analyte dynamics, an alternate approach is to use microfluidics to control sweat flow through the sensor so that electrochemical sensors interact with fresh sweat as older sweat is pushed away. This enables continuous measurement of dynamic analyte levels without needing to replace the sensor. An additional advantage of incorporating microfluidics is that it enables simultaneous sweat rate measurement. Near- or at-rest sweat may provide unique insight into body physiology compared to exercise, thermal, or chemically induced sweat. Specifically, the rate of resting sweat secretion can reflect sympathetic nervous system activity stemming from underlying health conditions. For example, resting sweating rate is related to defects in the central nervous system of infants,[1,2] to the severity of paresis in patients with brain infarction,[3,4] and to physiological habituation of soldiers.[5] Elevated or inhibited sweating at rest can further indicate autonomic dysfunctions, diabetes, cerebrovascular diseases, and Parkinson's disease, as well as chronic psychological stress, anxiety, or pain. [6–8] Resting sweat is uniquely poised to give insight into these conditions by ensuring that endogenous sweating rates associated with stress, injury, or illness aren't overwhelmed or confounded by the vastly higher rates associated with exercise or other external sweat triggers. In addition, low secretion rates may better preserve diffusive equilibria of biomarkers between sweat and blood, potentially making resting sweat composition more reflective of blood chemistry than other types of sweat. Finally, resting sweat is continuously generated, unlike the discrete or short-term generation of exercise or chemically-induced sweat, creating opportunities for long-term monitoring of evolving body state even for impacted populations including patients or the elderly. Continuous measurement of at-rest thermoregulatory sweat rate and composition with wearable sensors can therefore be a powerful route for non-invasive health monitoring.

Accessing resting sweat remains an outstanding challenge, as low secretion rates and rapid evaporation limit the amount of biofluid volume available to be collected in a sensor for analysis. For this reason, most wearable sweat sensors have focused on exercise, thermal, or chemically-

stimulated sweat produced at rates of 10's or 100's of nL min^{-1} cm^{-2} or higher.[9–22] They are unable to draw low volumes of resting sweat rapidly into the device, limiting real-time assessment. A few platforms have targeted low nL min^{-1} cm^{-2} rates, but have failed to enable continuous analysis and, critically, accurate measurement of resting sweat rate.[23,24] Even historically, at-rest thermoregulatory sweat rate monitoring in clinical environments has required bulky instrumentation such as ventilated humidity measurement chambers, or 24-hour collection periods for single-point analyte measurement.[25] Convenient, wearable devices for continuous resting sweat monitoring remain a gap in the field. This is a key outstanding challenge that must be overcome to make sweat a viable mode of health monitoring across activities, whether active or sedentary, and across user groups, whether young or old, healthy or ill.

In this chapter, we present a wearable patch for continuous measurement of at-rest thermoregulatory sweat composition and rate, overcoming evaporation by entrapment of sweat within a microfluidic sensing channel. Rapid uptake at low secretion rates is achieved via incorporation of a hydrophilic filler in the sweat collection well to reduce the volume of sweat that must be accumulated before it is pushed into the channel for measurement. Combining a rigid, hydrophilic insert with an overlaying hydrogel prevents sweat leakage for rapid uptake while also ensuring mechanical integrity. In addition, channel dimensions are tailored to minimize hydraulic pressure losses so that sweat gland secretory pressure is sufficient to push resting sweat into the device, while also ensuring fast movement of entrapped sweat within the channel and over embedded sweat rate sensing electrodes. These electrodes have interdigitated spokes – as the advancing sweat front meets a new spoke, a jump in admittance is detected that allows for selective flow measurement without interference from varying ionic concentration. Additionally, the patch has a small footprint that allows versatile body placement even at small-area regions like the fingertips. Along with the electrical sensor for sweat rate monitoring, we integrate electrodes that can be functionalized into versatile electrochemical sensors, such as for pH, Cl$^-$, and levodopa detection. These analytes are chosen to demonstrate the patch's capabilities for ion and enzymatic sensing. In this chapter, we characterize the sensor performance for resting sweat rate and composition tracking, and present case studies for using resting sweat rate as a biomarker for identifying stress and diabetes-related metabolic events. Overall, this platform can advance sweat investigations beyond what current wearable sweat sensors can provide by promoting a fundamental understanding of at-rest sweat secretion and its relation to diverse health conditions.

5.2 Microfluidic sensing patch design and structure

Our microfluidic device shown in **Figure 1** is designed to enable effective small volume collection and analysis of resting sweat. The device includes three major components: a microfluidic layer, electrochemical and electrical sweat sensing electrodes, and a laminated hydrophilic filler. As displayed in **Figure 1a**, the polydimethylsiloxane (PDMS)-based microfluidic layer contains a collection well and a microfluidic channel. The collection well interfaces the skin and its area can be modulated to acquire varying amounts of sweat. The microfluidic channel contains two intertwined spirals, and the channel connects the collection well
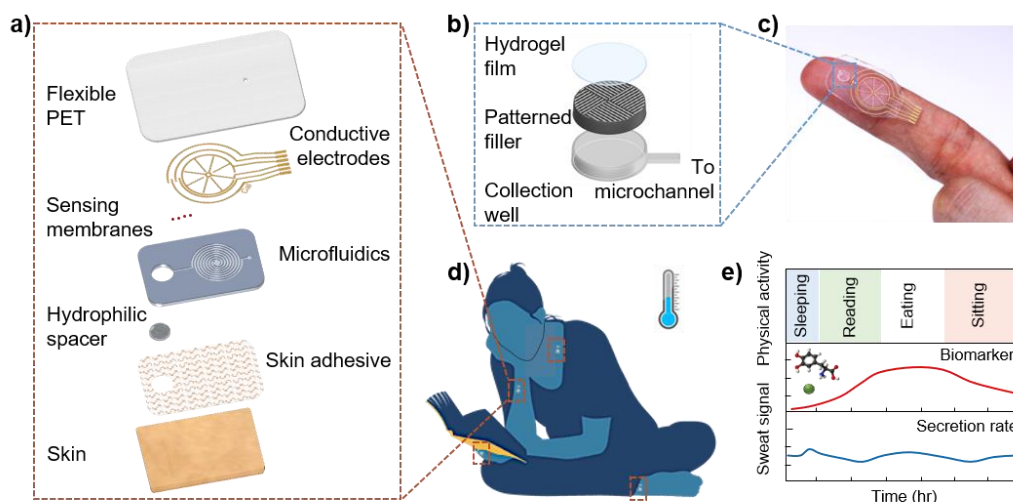
Figure 1. A schematic of the design, structure, and usage of the microfluidic sweat analysis patch. a) The patch contains multiple layers. It interfaces the skin via a skin adhesive, and sweat is collected by assistance of hydrophilic filler into the microfluidics and eventually measured using sensing electrodes fabricated on a thin PET. b) The hydrophilic filler includes a patterned SU8 mold covered with PVA film and AG-GLY hydrogel and is embedded inside the collection well. The filler enhances sweat collection by lowering sweat secretion pressure and taking up volume of the well otherwise will need to be filled. c) An optical image of the sweat patch on a user's finger is displayed. d) The patch can be worn on various locations and is used to monitor sweat dynamics without interrupting routine activities. e) It can continuously monitor both sweat secretion rate and compositions for long-term without external sweat stimulation, as schematically shown using model trends.

and the outlet. The microfluidic layer is aligned and bonded together with the sweat sensing electrodes. The sensing electrodes contain four outer semi-circles surrounding two interdigitated wheel-shaped electrodes. The electrochemical sensors such as pH, Cl⁻, and levodopa are functionalized on the semi-circles, and the central interdigitated wheel acts as an impedance-based sweat rate sensor. Finally, the collection well is filled with a patterned SU8 filler coated with a thin saturated hydrogel layer that contacts skin for sweat uptake (**Figure 1b**). The patch can be worn on areas such as the finger and wrist without interrupting human activities as pictured in **Figure 1c** and **1d**.

Humans' sweat secretion rates at rest vary across different body locations on average. For instance, sweat secretion rates can be lower than 10 nL min⁻¹ cm⁻² at low secretion sites such as arm and leg, and can reach on the order of 100 nL min⁻¹ cm⁻² at high secretion areas like the palm and foot.[26,27] Such secretion rates are small compared to typical sweat rates obtained by active sweat stimulation, which can be higher by an order.[26,28] To enable low resting sweat rate measurement inside the microchannel, the channel cross-section needs to be as small as possible such that temporal variations in secretion rate can be resolved by allowing fast speeds of the

moving sweat front. At the same time, the channel resistance cannot be so high as to limit flow in the channel and potentially suffocate sweat gland secretion, so the channel cross section cannot be too narrow. Finally, the channel length needs to be long enough for the device to have sufficient volumetric holding capacity to enable long-term measurement on desired body locations. Here, we aim to develop a microfluidic device that can contain ~ 750 nL or greater such that sweat analysis can be done longer than an hour at the lowest sweat rate regions. Toward this goal, we estimated secretory pressures of the sweat gland spanning a broad range of resting sweat secretion rates from 3 nL min^{-1} cm^{-2} to 1 µL min^{-1} cm^{-2}. We established that the channel contributes to most of the device hydraulic resistance compared to the collection well. For various square cross-sectional areas and associated channel lengths that give close to 750 nL holding capacity, we calculated hydraulic pressure losses and compared these to the secretory pressure of the grand. From this, we established that a channel cross section of 70 µm x 70 µm with ~ 15 cm length has low enough resistance to support sweat flow across low to high secretory rates. Detailed calculations of this procedure are reported in the Appendix of this chapter. Based on these results, we chose two cross-sectional areas of the spiraling microfluidic portion for sweat rate measurement, 70 µm x 70 µm (design 1) and 200 µm x 70 µm (design 2) as depicted in **Figure S1** of the Appendix, with lengths shorter than 15 cm to monitor sweat rates in low and high secretion regions respectively. Note that channels on the order of 10's of microns wide have been previously demonstrated for wicking nanoliters of sweat off the skin surface and onto the sensor.[25] In contrast, the spiraling channel design used here is crucial not only for capturing low sweat volumes, but for efficiently drawing it over interdigitated electrode spokes for selective, continuous sweat rate measurement within a consolidated sensor footprint.

It is ideally beneficial for microfluidic collection area to be large to maximize the accessible sweat glands. However, a large collection area creates a dead volume, in which sweat firstly needs to be filled before flowing into the microchannel. This creates a lag time in sensor's response. To address this problem, we incorporated a hydrophilic filler, containing a patterned SU8 mold and hydrogels, to occupy the dead volume and to draw sweat readily into the channel as soon as it secretes. Hydrogels have been used extensively in the wearable electronics community to create soft interfaces and to absorb and hold biofluids onto sensor surfaces, but deploying gels to enhance sweat replacement times and minimize accumulation volumes and lag times represents a key advantage in this work.[29–31] This structure overall comprises of a PVA-coated rigid SU8 component that is first inserted into the well and overlaid with an agarose-glycerol hydrogel that directly contacts skin for sweat uptake (**Figure S2** in the Appendix). Optical images of the filler and the assembled microfluidic are shown in **Figure S3** in the Appendix. We did not use hydrogel alone as a filler because it can dilute sweat compositions and hence put a challenge on the detection limit and sensitivity of electrochemical sensors, so we instead use only a thin hydrogel layer and occupy the remaining dead space with the rigid filler. The ameliorating effects of this combination on mixing and analyte dispersion are detailed in the Appendix. The filler further contributes to mechanical integrity, inhibiting collapse of the collection well under pressures which could otherwise artificially force fluid into the channel and create artefacts in measured sweat rate. The

SU8 filler is patterned with grooves to alternate closed-off regions that diminish well volume with open regions roughly 100 µm-wide that allow sweat to pass through and into the device. The hydrophilic film contains two layers: a polyvinyl alcohol (PVA) and an agarose-glycerol (AG-GLY) film. The thin PVA film covers the entire SU8 filler. A single PVA layer is brittle and can easily expose the hydrophobic pathway along the cracks. This will introduce pressure against sweat secretion due to surface tension and can prevent effective transport of sweat from the skin surface into the channel. By addition of the deformable AG-GLY gel[32] with high hydrophilicity, sweat from the collection area can be drawn into the gel and transported to the microchannel more effectively. Therefore, the AG-GLY film covers the top surface of the filler and is directly in contact with the skin. Without the hydrophilic filler, volumetric calculations show that a collection well with a 5 mm diameter and a 400 µm thickness will require more than 2 hours to fill the well if sweat secretes at 300 nL min^{-1} cm^{-2} while taking over 30 min and 200 hours for extreme rates of 1 µL min^{-1} cm^{-2} and 3 nL min^{-1} cm^{-2} respectively. The integration of the hydrophilic filler enhances the collection and transports fluid into the channel within a few minutes. For a 5 mm diameter collection area, the film can hold a liquid volume of nearly 200 nL in the well. For 300 nL min^{-1} cm^{-2}, it takes approximately 3 mins to fill the well and initiate the sweat analysis. Similarly, it takes under a minute for a rate of 1 µL min^{-1} cm^{-2} near the upper range of resting sweat secretion or around 30 min for rates towards the 3 nL min^{-1} cm^{-2} lower end when appropriately sized collection wells are used. The experimental result using a syringe pump supports this conclusion as shown in **Figure S4a** (See the Appendix). For typical resting sweat rates ~ < 30 nL min^{-1} cm^{-2},[26] the difference in lag time is more apparent (~ 30 mins instead of ~ a day), and sweat measurement is almost impractical for a hollow PDMS well. Note that due to its small footprint and the fact that the sensing patch is held tightly against skin via medical adhesives, the hydrogel cannot swell so much that it pushes off from the skin surface and delaminates the patch. Instead, as the hydrogel uptakes sweat, the tight seal against skin forces the hydrogel to expel this sweat into the channel. This supports rapid and leak-proof collection of resting sweat in the channel. With further investigation of the hydrophilic film and device design, it is possible to enhance the time required to initiate thermoregulatory sweat analysis at rest. Unlike prior devices which utilize hydrophilic material that has direct contact with the sensor and the skin for compositional analysis of stimulated sweat,[21,24,33] our device separates the hydrophilic filler from the sensing channel such that the sensor surface is not impacted by fluid and pressure variations in the film, and to control and fix the amount of fluid in the sensing channel for consistent sensor signals. Using the device, we also enable detection of flow rate as low as 2 nL min^{-1} as presented in **Figure S4b** (See the Appendix of this chapter).

Due to low resting sweating rates and the dimensions of the well and channel, we expect some diffusion and Taylor dispersion of analyte concentrations between when sweat is secreted on the skin surface and when it arrives at the electrochemical sensors near the entry of the channel. We perform a careful study of the time lags associated with this spread of analyte profiles in the Appendix. Regions like the fingertips and hands are established to have relatively higher resting sweating rates, for which our simulations indicate a time lag of around 3 minutes.[27] This lag

presents a limit on how updated the continuously made measurements are, but is well below the time scale over which physiological changes are expected to be manifested in sweat. At lower rates, sweat intrinsically moves more slowly through the device and takes longer to arrive at the sensos, allowing more time for dispersion effects. In contrast, because sweat rate is measured simply by the rate of fluid front movement, continuous and updated sweat rate measurements can be made with negligible time lag once sweat enters the channel.

5.3 Data integrity considerations for sweat collection at rest

There are a few factors that may induce uncertainty in measured sweat rates values. They include possible sweat migration into the collection area from other parts underneath the patch. Additionally, there is a possibility of higher sweat rate in the collection area to make up for the perspiration that may be hampered in the rest part of the device. These factors can result in overestimation of the measured sweat rates; however, the relative sweat rates will not differ. To investigate the first concern, we spot colored dye on the underside of the patch. After device removal, we observe that skin is dyed just in the region of the collection well and not in surrounding regions, confirming that there is no lateral sweat leakage or transfer from the collection well, and all sweat produced in that area is forced into the device for measurement. The dyed sweat can be visually monitored as it flows in the channel to optically validate electrical sweat rate measurements or as an independent visual measurement scheme enabled by this patch. This scheme for optical sweat rate tracking is realized via discrete photographs of sweat progression within the channel described in **Figure S5** in the Appendix of this chapter.

As for the second factor that could impact sweat rate accuracy, namely compensatory sweating effects, all devices covering sweat glands can induce the same effect, and this requires careful studies in the future. Local heat generation due to on-body attachment of the patch must also be considered as it could potentially elevate sweating rates[17], but negligible local heating is observed as demonstrated in **Figure S6** in the Appendix of this chapter, due to the small patch size and at or near rest conditions. We compared the measured sweat rates from the patches with more traditional gravimetric analysis. For the latter, an absorbent pad is held against skin for sweat accumulation and weighed before and after each sweat collection that lasts approximately $20 - 30$ mins. The pad is placed in a shallow 0.5 cm^2 chamber to minimize evaporation during sweat collection. A new patch was used in each sweat collection. The patch and the pad were placed on ring and pinky fingers to simultaneously collect sweat. Results are displayed in **Figure S7** of the Appendix, which shows that the patch collects ~ 2 times larger sweat amount per unit area than the pad. It is important to note that evaporation of the absorbent pad during removal from the skin surface and weighing can have significant effect on the measured amount of sweat. We discovered that the evaporation rate from the pad can be $200 - 400$ nLmin^{-1} cm^{-2}, which is the same order of measured sweat rates. Hence, gravimetric measurement error can be on the order of 100 %. This can lead to a lower sweat rate measured by gravimetric method. This shows a key advantage of our device as it minimizes the uncertainty arisen from the evaporation. When dealing with low volumes and rates associated with at-rest sweat, our device encapsulates sweat immediately and
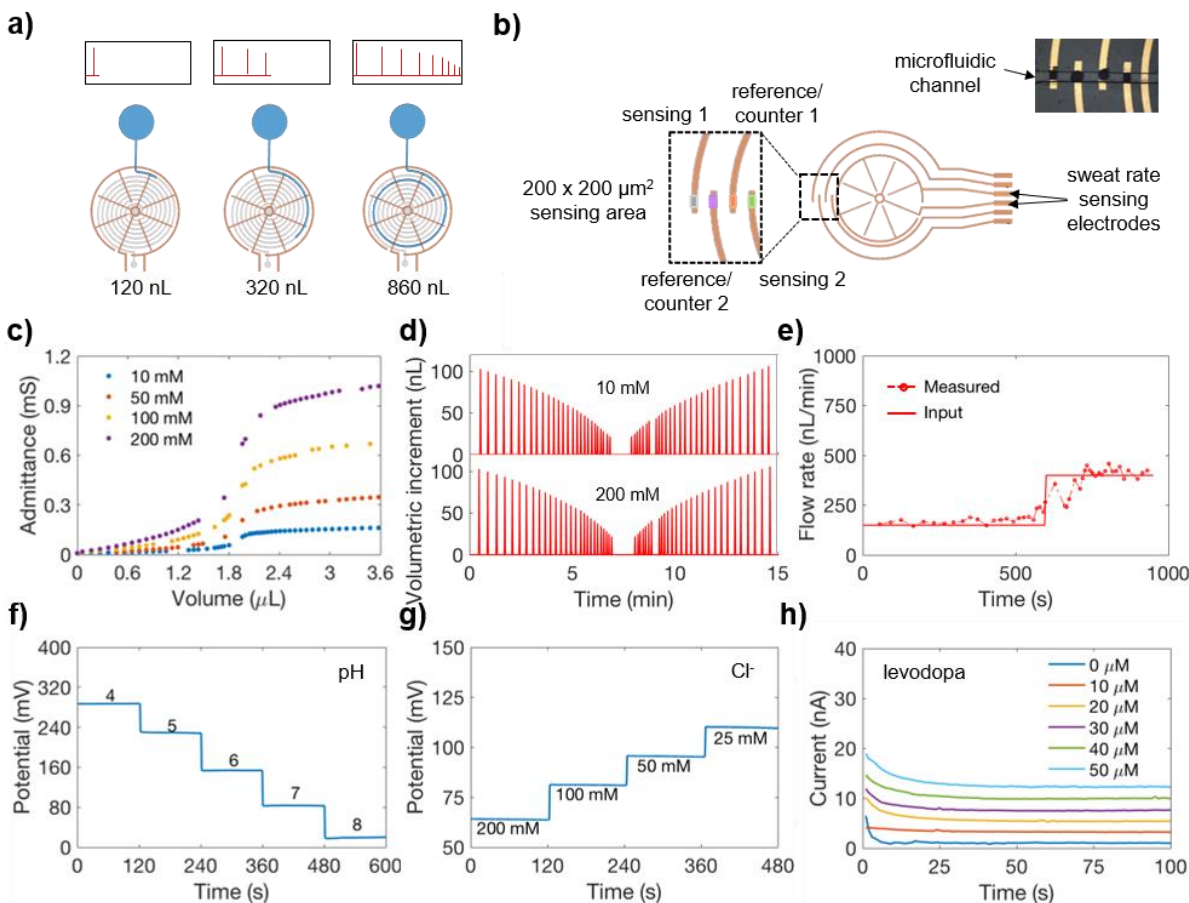
Figure 2. Sweat sensor characterization. a) An impedimetric sweat rate sensing electrodes for detection of secretion rate is illustrated. An admittance (reciprocal of impedance) pulse is measured upon fluid contacting each of the radial electrode. b) Electrochemical sensors for compositional analysis are functionalized near the tip of the four semicircles. These sensors are embedded inside the microchannel. c) Admittance responses to solution containing NaCl concentrations of 10, 50, 100, and 200 mM. d) Incremental volume filled inside the microchannel with respect to time is plotted when 10 and 200 mM NaCl solutions are flowed at a constant rate of 250 nL/min. The incremental volume corresponds to additional fluid filled between two adjacent radial electrodes. e) Input flow rate from syringe pump and measured flow rate from sweat rate sensor are compared. Performance of f) pH, g) Cl⁻, and h) levodopa sensors are presented.

uses a narrow channel to create rapid movement of the sweat front, translating into frequent and updated sweat rate measurements that overcome the evaporation and errors of gravimetric analysis. With these considerations, it is reasonable to assume that sweat under the collection area faithfully contributes to the measured sweat rate from the patch.

5.4 Sensor characterization

In order to utilize the microfluidic patch for electrical measurement, electrical sensing electrodes are incorporated into the microfluidic. As shown in **Figure 2a**, two interdigitated wheel shape

electrodes are aligned with the microfluidic and act as a sweat rate sensor. The electrodes contain a total of 8 to 24 radial electrodes. At the initial contact, a sudden change in admittance indicates fluid entering the channel. As fluid is transported through the channel, it contacts an increasing area of the radial electrodes. With each contact by fluid, the impedance decreases because of a decrease in the resistance between the two electrodes, and a pulse indicating a change in admittance (inversely proportional to impedance) is observed. By counting the number of pulses and time interval between each pulse, the volume contained in the channel and sweat rate can be computed. In other words, as the spacing between the spokes is known and the channel cross section is fixed, each time the sensor signal undergoes a discrete step change we can know how much additional volume of fluid was added to the channel. This allows an estimate of volumetric increment versus time, where the time points correspond to the time of the admittance step changes, as shown schematically by the signals **in Figure 2a**. Note that the spacing between spokes decreases as the channel spirals inwards and increases once it starts spiraling outwards. This causes the volume increment to decrease as the fluid front moves towards the center of the spiral, and to increase as it continues to move outwards.

A larger number of radial electrodes allows for higher temporal resolution of sweat rate measurements. Electrochemical sensors located at the end of the semicircular electrodes are aligned with the microchannel as shown in **Figure 2b**. This allows electrochemical analysis as soon as sweat secretes into the channel. Depending on the sensing mechanism, either electrical current or potential is monitored.

The sweat rate sensor (200 μm x 70 μm) was first characterized by measuring admittance in different concentrations of NaCl solutions at an operating frequency of 100 kHz. This frequency was chosen to minimize the capacitance contribution of the impedance and to maximize the resistive part of the impedance measurement. **Figure 2c** demonstrates the relationship between admittance and fluid volume in the channel for NaCl concentrations of 10, 50, 100, and 200 mM. It can be seen that at higher NaCl concentrations, the admittance between the electrodes increases due to the higher conductivity of increasing ion concentrations. Additionally, increasing fluid volume in the channel gives rise to higher admittance as more ionic solution is in contact with a larger area of the electrodes, decreasing the resistance between the electrodes. To demonstrate the reliability and reproducibility of the sweat rate sensors, it is also necessary to show that the time interval between admittance pulses is the same for a given flow rate in the channel and for fluid volume between the two contacts regardless of ions concentration. Using a commercial syringe pump, 10 and 200 mM NaCl solutions were flowed at a constant rate of 250 nL min^{-1} into the sweat rate sensor. The volumetric increments between consecutive contacts is plotted as a function of time in **Figure 2d**. In comparing the 10 mM and 200 mM plots, it can be seen that the pulses occur at the same time, indicating a reproducible calculation of sweat rate. It is also important to note that the time interval spacing between each pulse is not the same for a constant flow rate in the channel because the fluid volume between consecutive contacts decreases as fluid travels towards the center and increases as fluid travels outwards from the center towards the outlet. For

a 24-electrodes with 200 μm x 70 μm channel, the time resolution is between ~ 4-20 sec for 50 nL min^{-1} and can reach 2-9 min for 2 nL min^{-1}. For a 24-electrodes with 70 μm x 70 μm channel design, the resolution is further enhanced. Lastly, to verify that our sweat rate device accurately returns the correct flow rate, the measured flow rate calculated from our sweat rate sensor was compared against the known input pump rate of a commercial syringe pump system. The syringe pump was used to flow 200 mM NaCl inside the microfluidic channel at an input rate of 150 nL min^{-1} and 400 nL min^{-1} as shown in **Figure 2e**. It can be seen that the input pump rate is in agreement with the measured flow rate from the device, which is also evident in **Figure S4b** (See the Appendix) for lower flow rates. Note that an injection pump is used to conduct this benchtop analysis, and variation in how smoothly and consistently the pump injects at the pre-set rate causes fluctuations in the measured signal. This can be treated and potentially filtered as noise.

To demonstrate the patch's suitability for simultaneous composition measurement, we functionalize and characterize the electrochemical sensors which have a sensing area of 200 μm by 200 μm each, given the 200 μm width of the functionalized electrode tips and the 200 μm width of the microfluidic channel in between the collection well and spiraling portion (as depicted in **Figure S1** of the Appendix). As shown in **Figure 2b**, two electrodes serve as reference/counter electrode, and two electrodes are functionalized to detect target analytes. Detailed fabrication steps are outlined in the Methods. **Figure 2f** and **2g** shows the performance of a pH sensor in pH 4 to 8 McIlvaine's buffer and a Cl$^-$ sensor in solution containing 25 to 200 mM NaCl. Their sensitivities are measured to be 60 mV/pH and 55 mV/decade, which are close to Nernstian behavior. **Figure 2h** presents the performance of a levodopa sensor with a sensitivity of 0.2 nA μM^{-1}, an improvement in sensitivity per area compared to our previous work[34] due to an increased active surface area arising from modified fabrication detailed in the Methods section. All sensors show high sensitivity within the physiological range, with linear calibration curves shown in **Figure S8** as well as reproducibility, stability, and bending tests shown in **Figure S9** and **Figure S10**.[13,34,35] These tests demonstate that the electrochemical sensors in this patch perform similar to those reported in previous works by us and others in the field. However, for the purposes of this chapter, we will focus primarily on the physiological information that can be obtained from resting sweat rate measurements in the following sections. Specifically, two case studies in particular are highlighted below focusing on the significance of sweat rate monitoring for detecting stress events and hypoglycemia.

5.5 24-hour resting sweat analysis for stress monitoring

The patch was worn on the fingertip of a healthy volunteer during two trials, 24 hours each, with routine activity including eating, walking, and sleeping, while heart rate and ambient temperature were monitored simultaneously. The subject was mostly sedentary and performed intervals of public speaking including giving a presentation and answering questions in a live streamed conference in Trial 1 (**Figure 3a**), and teaching a virtual class in Trial 2 (**Figure 3b**). These events generated a stress response in the body due to a combination of anticipation and public speaking that is reminiscent of the clinical standard Trier Social Stress Test[36]. Heart rate
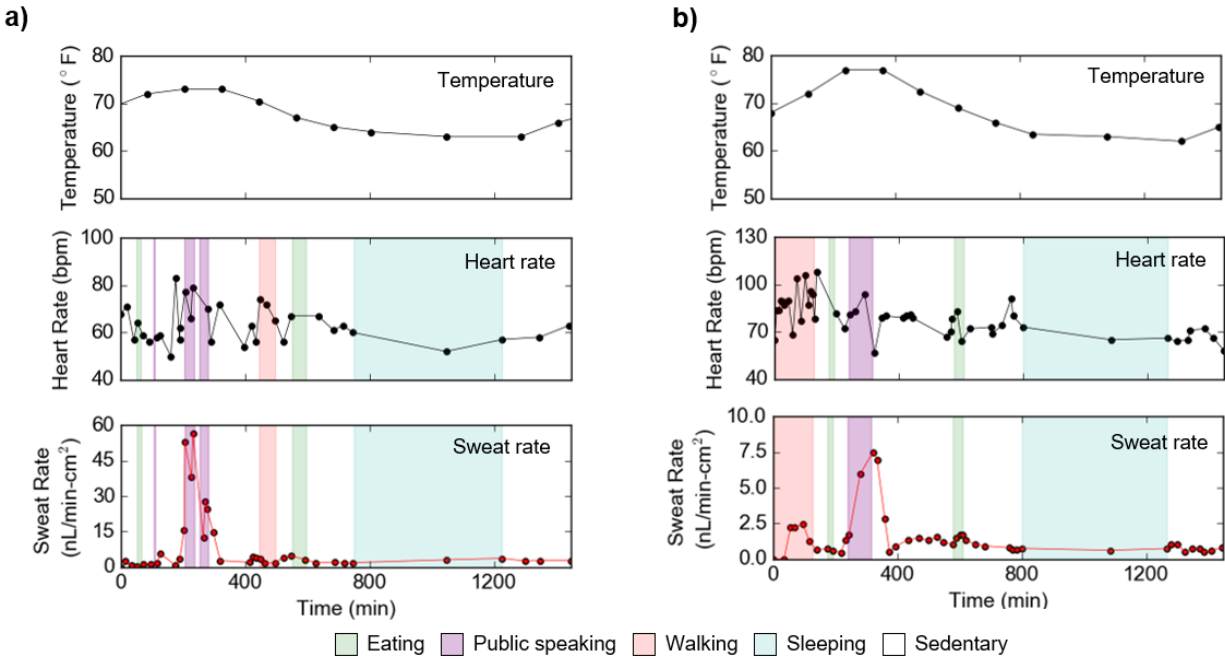
Figure 3. 24-hour in-situ sweat analysis to identify stress events among routine activities. Sweat is monitored on the fingertip of a healthy volunteer along with heart rate and ambient temperature as the mostly sedentary subject performed intervals of public speaking a) during a live-streamed academic conference in Trial 1, and b) while teaching a class in Trial 2. The stress-inducing intervals of public speaking are associated with elevated heart rate and a sharp increase in sweat rate.

generally elevated in anticipation of and during the stress events in both trials, increasing a total of 28 bpm for the presentation in Trial 1 and 21 bpm while teaching in Trial 2. In Trial 1, baseline sweat rates during routine activities hovered around 2.8 nL min^{-1} cm^{-2} but elevated up to nearly 57 nL min^{-1} cm^{-2} during the presentation. Similarly, in Trial 2, baseline sweating rates were typically under 2.5 nL min^{-1} cm^{-2} but elevated to over 7.5 nL min^{-1} cm^{-2} while teaching. These trials demonstrate the capability of these patches to detect monitor the body's normal sweating response during routine activities over extended and full-day time periods, and from this identify when the body moves into physiologically deviating states such as those produced during stress. Many clinical tests of stress rely on self-reported and largely qualitative measures, but this work creates potential opportunities for continuous and quantitative stress testing through resting sweat rate.

5.6 Resting sweat analysis for hypoglycemia detection

The patch was further utilized to investigate hypoglycemia-induced sweat secretion. In diabetic patients, injection of insulin gives rise to hyperhidrosis due to hypoglycemia.[37,38] They can also be vulnerable to irregular heartbeat, which can be life-threatening.[39] Understanding sweating and heart complications in diabetic patients, hence, can facilitate diabetes management. Toward this aim, we performed simultaneous monitoring of heart rate, sweat rate, and interstitial
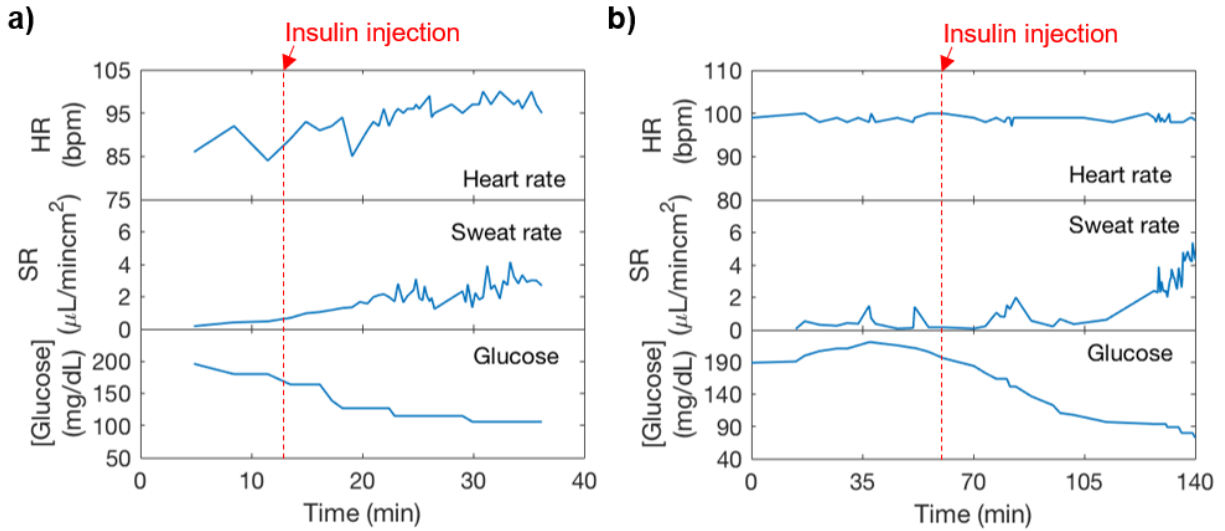
Figure 4. *In-situ* sweat analysis for hypoglycemia-induced sweat analysis. Sweat secretion rate was measured along with heart rate and ISF glucose levels of a diabetic subject. Subject had insulin injection to lower glucose levels in a) trial 1 and b) trial 2.

fluid (ISF) glucose levels to explore heart and sweat complications during large glucose variation. A diabetic subject wore the microfluidic patch on the finger along with a pulse oximeter. The measurement was done without interrupting the routine insulin injection procedures of the diabetic patient. During the measurement duration, the subject was asked to remain sitting without vigorous movements. ISF glucose data was recorded via Dexcom G6 continuous glucose monitor. **Figure 4a and 4b** show measurements obtained from the two trials on the diabetic subject. In both trials, glucose was initially high when the measurement began, and the sweat rate remained relatively low between 0.5 and 1 μL min^{-1} cm^{-2}. After insulin was injected, glucose started to decrease rapidly. In the meantime, an increase in sweat rate was observed. When glucose further decreased lower than 90 mg/dL in **Figure 4b**, there was a dramatic increase in sweat rate up to 5 μL min^{-1} cm^{-2}. Heart rate remained relatively unchanged during low glucose level. Based on our results, significant decrease in glucose level is accompanied by a rise in sweat rate while no clear heart rate irregularity is observed. To develop this qualitative relation further, larger population studies must be conducted in future to quantitatively relate low glucose events and elevated sweating at rest.

In summary, we present a wearable device for rapid uptake of nL min^{-1} cm^{-2} rates of thermoregulatory sweat at rest, enabling near-real-time sweat rate and composition analysis at rest. This represents a crucial advancement for detecting sweat rates associated with underlying physiological conditions, as demonstrated in subject studies exploring the relation between at-rest sweating and metabolic and stress conditions. Expanding on these preliminary trials, this patch can be deployed for patients or applications where deregulated sweating is *a priori* known to indicate underlying health conditions, or can be used in exploratory subject studies to decode how sweating patterns relate to broader physiology. For example, hypoglycemia is known to qualitatively

increase sweating rates as the body seeks to lower core temperature to conserve energy.[40] The presented patch can be used to more quantitatively study this phenomenon by simultaneously accumulating data on resting sweating rates and blood glucose levels, both for an individual over time and across a population of subjects. Personalized and universal correlations could then be built that enable resting sweat rate to serve as a non-invasive predictor of hypoglycemia. Similarly, excessive sweating is qualitatively known to indicate psychological duress, but more quantitative correlation studies can be performed between resting sweating rate and traditional, invasively-obtained or discrete measures of mental state such as cortisol hormone levels.[41] Based on these correlations, at-rest sweat rate could then be used to continuously and non-invasively estimate stress, with applications in assessing and improving the welfare of infants, soldiers, and stroke patients, and more generally of individuals going about everyday activities. More generally, the presented patch can be used to study correlations between sweat rates and composition, helping to better understand analyte secretion mechanisms and guide how measured concentrations should be interpreted. By allowing these studies to be performed in a way that is compatible with daily routines, this work creates fresh opportunities for decoding how non-invasive parameters relate to deeper body health and for establishing the physiological utility of sweat sensing as a whole.

5.7 Methods

5.7.1 Sensor fabrication

Conductive Au electrodes were fabricated by standard photolithography and evaporation methods as detailed in our prior work.[35] Electrochemical depositions required for sensor functionalization were performed on PCI4G300 (Gamry Instruments, USA). pH sensor was prepared by growing Au microstructures at 0 V for 30 s to roughen the surface as demonstrated in previous works[42], and then electrochemically depositing aniline solution (1 M HCl, 0.1 M aniline) by performing cyclic voltammetry from -0.2 to 1 V vs. Ag/AgCl at 100 mV/s for 25 cycles. Cl^- sensor was prepared by dropcasting silver ink and cured at 90 °C for 30 mins. The electrode was subsequently treated with 0.1 M $FeCl_3$ for 1 min. The reference electrode for pH and Cl^- sensors was prepared by dropcasting a thin layer of silver ink onto the Au electrode. After drying, a solution containing 79.1 mg PVB and 50 mg NaCl in 1 mL methanol was dropcasted (10 μL/mm^2). Levodopa sensor was prepared by initially growing Au nanodendrites using pulsed voltage from -1 to 1 V at a signal frequency of 50 Hz, 50 % duty cycle, and 1500 cycles, creating high surface area structures as imaged in our previous work[43]. Thionine acetate salt solution (0.25 mM) was deposited by applying 1 Hz signal frequency, pulsed voltage from -0.6 to 0 V, 90 % duty cycle, and 660 cycles. Next, 0.2 μL of Tyrosinase solution containing 99 μL of 1 % BSA, 1 μL of 2.5 % glutaraldehyde, and 0.25 μL of 1 mg/mL tyrosinase was dropcasted and dried. The membrane was additionally coated with 0.2 μL of Nafion-TBAB solution which was prepared as reported in literature.[44] The levodopa sensors could be used after drying for an hour at room temperature. For long-term storage, levodopa sensors were kept at 4°C. The shared reference/counter electrode for levodopa sensor was prepared by dropcasting silver ink and letting it dry before usage.

5.7.2 Microfluidic device fabrication

Microfluidic was fabricated using standard photolithography process. SU8 photoresist was used to pattern microfluidics on a Si wafer. PDMS (base to curing agent ratio of 10:1) was poured onto the SU8 mold and cured at 60 °C for 4 to 5 hours. The cured PDMS was peeled off and put under O_2 plasma, along with the PET patterned with sensing electrodes at a power of 90 W, 0.2 mtorr for 1 min. 1 % APTES solution was dropcasted on entire surface of the PET for 2 min. The PET was cleaned with DI water and quickly dry with N_2. The PET was then bonded with PDMS and left it for at least an hour before usage. PDMS is soaked in DI water for 5 hr prior to utilization to saturate PDMS[45] such that permeation-driven flow is minimized.[46] Oversaturation can also be achieved through longer pre-soak time at high temperature. By pre-soaking, sweat-containing microfluidic channel evaporated/diffused through the PDMS at 0.01 nL min^{-1} cm^{-2} when the device was tested for 8 hours at 21-23 °C and relative humidity of 39-42 %.

5.7.3 Hydrophilic filler fabrication

The patterned SU8 filler was prepared to a thickness of 200 μm on a flexible PET using standard procedures. The filler was carefully peeled off from the PET and put under O_2 plasma. A solution containing 0.5 % PVA in DI water was then drop-casted onto the filler (0.5 $μL/mm^2$), ensuring a complete coverage on the entire filler (including side and back walls), and was quickly heated on a hotplate at 80 °C. The PVA film was approximately 10 μm in thickness. Once PVA dried, an AG-GLY film was placed on top of the filler. AG-GLY film was prepared by stirring and dissolving 2 % agarose and 50 % glycerol in DI water at 120 °C for 5 mins. Once everything dissolved, ~ 3 mL of the solution was quickly poured into a 100 mm hydrophilic glass dish and waited until the solution dried to become a gel-like film. The AG-GLY solution is viscous and dries easily; hence, rapid pour on a hydrophilic dish is necessary for a thin and uniform thickness. Here the AG-GLY film was not directly drop-casted on the filler because of the difficulty to achieve a thin uniform coating on the entire filler if we directly drop-casted the solution. The AG-GLY film was saturated with deionized water before placing on the filler. The film is approximately 90-130 μm thick. The laminated filler was finally placed inside the collection well of the microfluidic patch.

5.7.4 Device characterization

Sensor characterizations were performed on CHI1430 (CH Instruments, USA). The pH sensor was tested using McIlvaine's buffer of pH 4 to 8, and Cl^- sensor was tested using NaCl solution of concentration ranging from 25 to 200 mM. The potential difference with respect to a reference electrode was measured for both sensors. Levodopa sensor was measured by applying 0.35 V with respect to a shared reference/counter silver electrode. Flow rate experiments were carried out using Harvard Apparatus PHD 2000 Syringe Pump.

5.7.5 On-body sweat analysis

On-body human trials were carried out at the University of California, Berkeley in compliance with the human research protocol (CPHS 2014-08-6636 and CPHS 2015-05-7578) approved by the Berkeley Institutional Review Board (IRB). Both male and female subjects (between aged 21 to 45) were recruited from the Berkeley campus through campus flyers and verbal recruitments. Informed consents were obtained from all study subjects before enrollment in the study. Trials in **Figure 3** were conducted at 40-50% relative humidity with temperatures indicated in the figure. Trials in **Figure 4** were conducted at 21 °C and 40 % relative humidity. Targeted locations for sweat analysis were wiped with alcohol swab and gauze before application of the microfluidic device. Subjects were allowed to wear comfortable clothing. For heart rate measurements, a pulse oximeter (Zacurate Model 500DL) was used. The double-sided adhesive that was laminated between the skin and the patch was from Adhesive Research (93551). To ensure device could stay firmly on skin for the measurement durations, an additional adhesive (93690 from Adhesive Research) was applied on top of the patch. No irritation from these adhesives or prolonged patch wear, and no adhesive delamination, were found during the extended on-body trials, consistent with the adhesives' suitability of over 14 days of wear as stated by the manufacturer. Electrical sweat rate data were collected using E4980AL precision LCR meter (Keysight Technologies).

5.8 References

1. Foster, K. G., Hey, E. N. & O'Connell, B. Sweat function in babies with defects of central nervous system. *Arch Dis Child* **46**, 444–451 (1971).
2. Harpin, V. A. & Rutter, N. Development of emotional sweating in the newborn infant. *Arch Dis Child* **57**, 691–695 (1982).
3. Satoh, T., Ogawa, T. & Takagi, K. Sweating During Daytime Sleep. *The Japanese Journal of Physiology* **15**, 523–531 (1965).
4. Korpelainen, J. T., Sotaniemi, K. A. & Myllylä, V. V. Asymmetric sweating in stroke: a prospective quantitative study of patients with hemispheral brain infarction. *Neurology* **43**, 1211–1214 (1993).
5. Wood, D. *et al.* Combat-Related Post-Traumatic Stress Disorder: A Case Report Using Virtual Reality Graded Exposure Therapy With Physiological Monitoring With a Female Seabee. *Military medicine* **174**, 1215–22 (2009).
6. Cheshire, W. P. & Freeman, R. Disorders of sweating. *Semin Neurol* **23**, 399–406 (2003).
7. Micieli, G., Tosi, P., Marcheselli, S. & Cavallini, A. Autonomic dysfunction in Parkinson's disease. *Neurol Sci* **24 Suppl 1**, S32-34 (2003).
8. Harker, M. Psychological sweating: a systematic review focused on aetiology and cutaneous response. *Skin Pharmacol Physiol* **26**, 92–100 (2013).
9. Yang, Y. *et al.* A laser-engraved wearable sensor for sensitive detection of uric acid and tyrosine in sweat. *Nature Biotechnology* **38**, 217–224 (2020).
10. Parlak, O., Keene, S. T., Marais, A., Curto, V. F. & Salleo, A. Molecularly selective nanoporous membrane-based wearable organic electrochemical device for noninvasive cortisol sensing. *Science Advances* **4**, eaar2904 (2018).
11. Lee, H. *et al.* Wearable/disposable sweat-based glucose monitoring device with multistage transdermal drug delivery module. *Science Advances* **3**, e1601314 (2017).

12. Yokus, M. A., Songkakul, T., Pozdin, V. A., Bozkurt, A. & Daniele, M. A. Wearable multiplexed biosensor system toward continuous monitoring of metabolites. *Biosens Bioelectron* **153**, 112038 (2020).

13. Emaminejad, S. *et al.* Autonomous sweat extraction and analysis applied to cystic fibrosis and glucose monitoring using a fully integrated wearable platform. *PNAS* **114**, 4625–4630 (2017).

14. Jia, W. *et al.* Electrochemical Tattoo Biosensors for Real-Time Noninvasive Lactate Monitoring in Human Perspiration. http://pubs.acs.org/doi/abs/10.1021/ac401573r (2013) doi:10.1021/ac401573r.

15. Kim, J. *et al.* Noninvasive Alcohol Monitoring Using a Wearable Tattoo-Based Iontophoretic-Biosensing System. http://pubs.acs.org/doi/abs/10.1021/acssensors.6b00356 (2016) doi:10.1021/acssensors.6b00356.

16. Nyein, H. Y. Y. *et al.* Regional and correlative sweat analysis using high-throughput microfluidic sensing patches toward decoding sweat. *Science Advances* **5**, eaaw9906 (2019).

17. Alizadeh, A. *et al.* A wearable patch for continuous monitoring of sweat electrolytes during exertion. *Lab Chip* **18**, 2632–2641 (2018).

18. Bandodkar, A. J., Jeang, W. J., Ghaffari, R. & Rogers, J. A. Wearable Sensors for Biochemical Sweat Analysis. *Annu Rev Anal Chem (Palo Alto Calif)* **12**, 1–22 (2019).

19. Li, S., Ma, Z., Cao, Z., Pan, L. & Shi, Y. Advanced Wearable Microfluidic Sensors for Healthcare Monitoring. *Small* **16**, 1903822 (2020).

20. Koh, A. *et al.* A soft, wearable microfluidic device for the capture, storage, and colorimetric sensing of sweat. *Science Translational Medicine* **8**, 366ra165-366ra165 (2016).

21. Twine, N. B. *et al.* Open nanofluidic films with rapid transport and no analyte exchange for ultra-low sample volumes. *Lab Chip* **18**, 2816–2825 (2018).

22. Bariya, M. *et al.* Roll-to-Roll Gravure Printed Electrochemical Sensors for Wearable and Medical Devices. *ACS Nano* **12**, 6978–6987 (2018).

23. Lin, S. *et al.* Natural Perspiration Sampling and in Situ Electrochemical Analysis with Hydrogel Micropatches for User-Identifiable and Wireless Chemo/Biosensing. *ACS Sens.* **5**, 93–102 (2020).

24. Hauke, A. *et al.* Complete validation of a continuous and blood-correlated sweat biosensing device with integrated sweat stimulation. *Lab Chip* **18**, 3750–3759 (2018).

25. Berger, M. J. & Kimpinski, K. Test–Retest Reliability of Quantitative Sudomotor Axon Reflex Testing. *Journal of Clinical Neurophysiology* **30**, 308–312 (2013).

26. Taylor, N. A. & Machado-Moreira, C. A. Regional variations in transepidermal water loss, eccrine sweat gland density, sweat secretion rates and electrolyte composition in resting and exercising humans. *Extreme Physiology & Medicine* **2**, 4 (2013).

27. Bariya, M. *et al.* Glove-based sensors for multimodal monitoring of natural sweat. *Science Advances* **6**, eabb8308 (2020).

28. Hussain, J. N., Mantri, N. & Cohen, M. M. Working Up a Good Sweat – The Challenges of Standardising Sweat Collection for Metabolomics Analysis. *Clin Biochem Rev* **38**, 13–34 (2017).

29. Koo, H.-J. & Velev, O. D. Design and characterization of hydrogel-based microfluidic devices with biomimetic solute transport networks. *Biomicrofluidics* **11**, 024104 (2017).

30. Shay, T., Dickey, M. D. & Velev, O. D. Hydrogel-enabled osmotic pumping for microfluidics: towards wearable human-device interfaces. *Lab Chip* **17**, 710–716 (2017).

31. Zhao, F. J. *et al.* Ultra-simple wearable local sweat volume monitoring patch based on swellable hydrogels. *Lab Chip* **20**, 168–174 (2019).
32. Barrangou, L. M., Daubert, C. R. & Foegeding, E. A. Textural properties of agarose gels. I. Rheological and fracture properties. *Food Hydrocolloids* **20**, 184–195.
33. Lee, H. *et al.* A graphene-based electrochemical device with thermoresponsive microneedles for diabetes monitoring and therapy. *Nature Nanotechnology* **11**, 566–572 (2016).
34. Tai, L.-C. *et al.* Wearable Sweat Band for Noninvasive Levodopa Monitoring. *Nano Lett.* **19**, 6346–6351 (2019).
35. Nyein, H. Y. Y. *et al.* A Wearable Electrochemical Platform for Noninvasive Simultaneous Monitoring of Ca2+ and pH. http://pubs.acs.org/doi/abs/10.1021/acsnano.6b04005 (2016) doi:10.1021/acsnano.6b04005.
36. Allen, A. P. *et al.* The Trier Social Stress Test: Principles and practice. *Neurobiol Stress* **6**, 113–126 (2016).
37. Passias, T. C., Meneilly, G. S. & Mekjavić, I. B. Effect of hypoglycemia on thermoregulatory responses. *J Appl Physiol (1985)* **80**, 1021–1032 (1996).
38. Buono, M. & Verity, L. Cholinergic-Induced Sweat Rate During Hypo-and Hyperglycemia. *Clinical Kinesiology* **58**, (2004).
39. Chow, E. *et al.* Risk of cardiac arrhythmias during hypoglycemia in patients with type 2 diabetes and cardiovascular risk. *Diabetes* **63**, 1738–1747 (2014).
40. Kenny, G. P., Sigal, R. J. & McGinn, R. Body temperature regulation in diabetes. *Temperature (Austin)* **3**, 119–145 (2016).
41. Burke, H. M., Davis, M. C., Otte, C. & Mohr, D. C. Depression and cortisol responses to psychological stress: A meta-analysis. *Psychoneuroendocrinology* **30**, 846–856 (2005).
42. Tian, Y., Liu, H., Zhao, G. & Tatsuma, T. Shape-Controlled Electrodeposition of Gold Nanostructures. *J. Phys. Chem. B* **110**, 23478–23481 (2006).
43. Lin, Y. *et al.* Porous Enzymatic Membrane for Nanotextured Glucose Sweat Sensors with High Stability toward Reliable Noninvasive Health Monitoring. *Advanced Functional Materials* **29**, 1902521 (2019).
44. Meredith, S., Xu, S., Meredith, M. T. & Minteer, S. D. Hydrophobic salt-modified Nafion for enzyme immobilization and stabilization. *J Vis Exp* e3949 (2012) doi:10.3791/3949.
45. Ojuroye, O., Torah, R. & Beeby, S. Modified PDMS packaging of sensory e-textile circuit microsystems for improved robustness with washing. *Microsyst Technol* (2019) doi:10.1007/s00542-019-04455-7.
46. Randall, G. C. & Doyle, P. S. Permeation-driven flow in poly(dimethylsiloxane) microfluidic devices. *PNAS* **102**, 10813–10818 (2005).

5.9 Appendix

5.9.1 Rationale for microfluidic channel dimensions

The sweat gland is treated as a volumetric fluid source generating sweat at rate Q and exiting the sweat gland with secretory pressure P_g. This sweat is forced into the device with hydraulic resistance $R_{tot} = R_{well} + R_{channel}$, producing a pressure drop of $\Delta P = R_{tot}Q$. To sustain this flow in the device, P_g must be larger than ΔP (ignoring atmospheric and Laplace pressures). P_g higher than this required pressure does not change the flow rate Q in the device but instead means that sweat will exit the microfluidic channel with some nonzero pressure.

Hydraulic resistance of the channel is given by

$R_{channel} = 12 \, \mu L / [0.37 * w^4]$

where $L = 15$ cm, $w = 70$ um, and $\mu =$ viscosity $= 9.5 * 10^{-4}$ Pa-s.[2] By Darcy's law,

$R_{well} = \mu L / kA = 2.17 * 10^{13}$ Pa-s/m^3

where $k =$ Darcy permeability for 2% agarose hydrogels of 100 μm thickness ≈ 620 nm^2,[3] $L = 100$ μm, and $A =$ cross sectional area of 3-mm diameter well.

Secretory pressures of the sweat gland for exercise and sauna-induced sweat are around 2.5 kPa, while those of chemically induced sweat can reach upwards of 70 kPa.[1, 4] Using the lower pressure as a conservative estimate, we can scale it down to lower resting sweat volumes (drawing on proportionalities indicated by Hoff's law $P = \sigma RT \Delta C$ since we expect the osmolality gradient to be related to secretion rate) assuming 2.5 kPa pressure corresponds conservatively to high rates of 20 nL min^{-1} gland^{-1}. Then at extreme resting sweat rates of 1 nL min^{-1} cm^{-2} in a 3-mm diameter well, corresponding to 70.7 nL min^{-1} entering the device, we can compare the estimated sweat gland secretory pressure of 1.2 kPa to the hydraulic pressure drops associated with different channel geometries to arrive at optimal dimensions. We assume a square channel cross section and a channel length that overall allows us to hold around 750 nL in the channel.
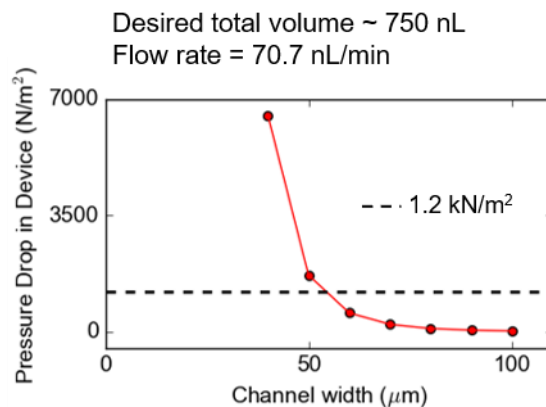
Choosing a channel width and height of 70 µm and a length around 15 cm allows a large enough volume capacity as well as a cross sectional area that is small enough to ensure fast sweat speed in the channel (necessary for high-resolution sweat rate measurement) but large enough to avoid excessive hydraulic pressure losses. In this case $R_{tot} = R_{well}+R_{channel} = 1.92 * 10^{14} + 2.17 * 10^{13}$ Pa-s/m^3 = 2.1 * 10^{14} Pa-s/m^3. ΔP is calculated for a broad range of resting sweat secretion and flow rates (high, medium, and low) and compared to the secretory pressure expected at those flow rates (according to $P = 2.5$ kPa * Q/(20 nL min^{-1} gland^{-1})) in a 3-mm diameter region with 7 glands based on typical sweat gland densities of 100 glands cm^{-2}) to confirm that the gland is a sufficient pump to inject sweat into a device of these dimensions.

Sweat secretion rate	Q (flow rate in device)	P (secretory pressure)	ΔP (hydraulic pressure loss in device)
1000 nL/min-cm²	70.7 nL/min	1.2 kN/m²	247 N/m²
50 nL/min-cm²	3.53 nL/min	63 N/m²	12.4 N/m²
3 nL/min-cm²	0.21 nL/min	3.8 N/m²	0.74 N/m²

5.9.2 Impact of Taylor dispersion on sensor lag times and accuracy

Analyte diffusivity, sweat collection volume, and sweat secretion rate will impact the time lag between when sweat of a certain composition is secreted and when it is registered by the sensor. To estimate this, we consider sweat mixing and Taylor dispersion in the collection well and channel respectively using extremes of the above parameters. The following considerations are applied in our simulations:

1. The effective volume of the hydrogel-containing collection well is 72 nL for a 3 mm-diameter region. Because of the large-area proportions of the collection well, there is bulk mixing between older and fresher sweat that is treated as a continual averaging in the well.
2. We consider three sweat secretion rates (high – 1000 nL min^{-1} cm^{-2}, medium – 50 nL min^{-1} cm^{-2}, and low – 3 nL min^{-1} cm^{-2}) that encompass a broad range of resting sweating rates. We consider sweat collection only in the 3 mm-diameter well as this broad range encompasses rates expected with the larger 8 mm opening. We consider the channel with cross section of 70 µm x 70 µm.
3. Diffusivities of H$^+$, Cl$^-$, and levodopa fall between 1 and 10 (x10^{-9}) m^2/s in water and in the agarose hydrogel, so these extreme values are used in the simulations.[5, 6]
4. The concentration of sweat at the sensor position depends on older sweat deeper in the channel and on sweat upstream in the channel and well. Sensor accuracy thus depends on the specific sweat composition profile, but to give a general sense of the time lags involved we consider a step concentration profile in which sweat entering the channel has concentration 0.5 for t < 0 and concentration of 1 at t ≥ 0. We solve the diffusion-advection equation in 1D (along the channel length) while incorporating Taylor dispersion to consider the temporal accuracy with which our device can reconstruct this concentration profile.

Microchannel: In the channel, the plots below compare smearing out of the concentration transition step at the sensor location (0.4 cm into the channel) at the three different secretion rates and extreme diffusivities. The table captures the time lag between when the step occurs at the entrance to the channel and is registered by the sensor as 90 % of the complete step in concentration. Note that the time for the sensor to register this step without diffusion or dispersion is related to the sweat secretion rate and speed in the device, so the time to 90% reconstruction must be compared to this value.
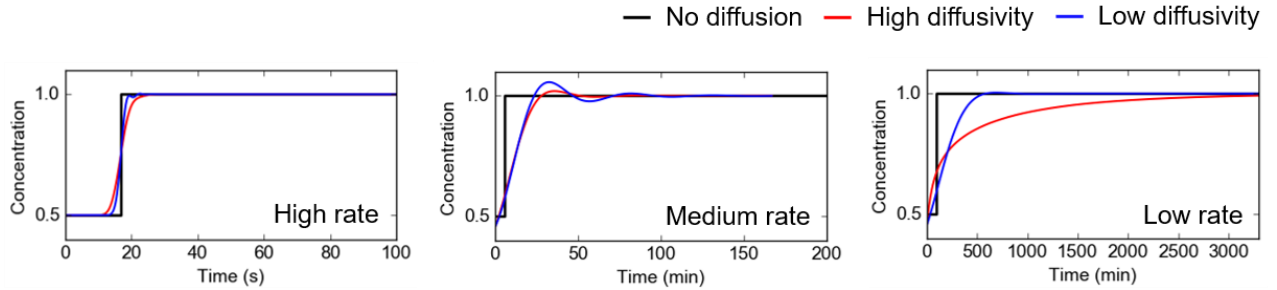
Sweat secretion rate (nL/min-cm^2)	Diffusivity (m^2/s)	Time for sensor to register step without diffusion or dispersion	Time for sensor to register 90% of step with diffusion and dispersion
1000	1 * 10^{-9}	16.6 s	18.2 s
	10 * 10^{-9}		19.8 s
50	1 * 10^{-9}	5.6 min	20.4 min
	10 * 10^{-9}		22.4 min
3	1 * 10^{-9}	92.4 min	403.7 min
	10 * 10^{-9}		1390.5 min

Collection well: In the collection well, the plot below averages sweat at concentration 0.5 before t = 0 with subsequent secretion of sweat at concentration 1 for t > 0 for the three sweat rates. The table below captures the the time lag between when sweat at concentration 1 starts secreting and when the well captures 90 % of the full change in concentration. Note that this time lag is related to the rate of sweat secretion and the time for adequate replacement of earlier sweat in the well.

Sweat secretion rate (nL/min-cm^2)	Time for 90% change in concentration with diffusion and dispersion
1000	2.3 min
50	46.8 min
3	781 min
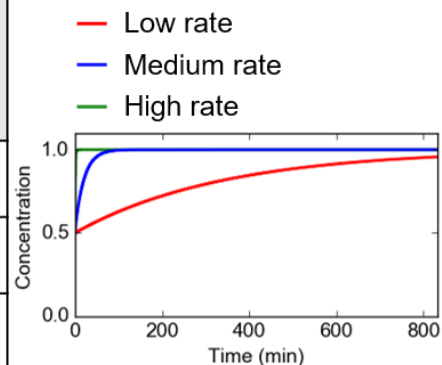
Overall, mixing and Taylor dispersion through the sections of the device indicate that at relatively high resting sweating rates on the fingertips, the sensor has a lag of around 3 minutes between when sweat at a certain composition is secreted and when it is detected at the sensor.

5.9.3 Figure S1: Geometric parameters and dimensions for the microfluidic patch.
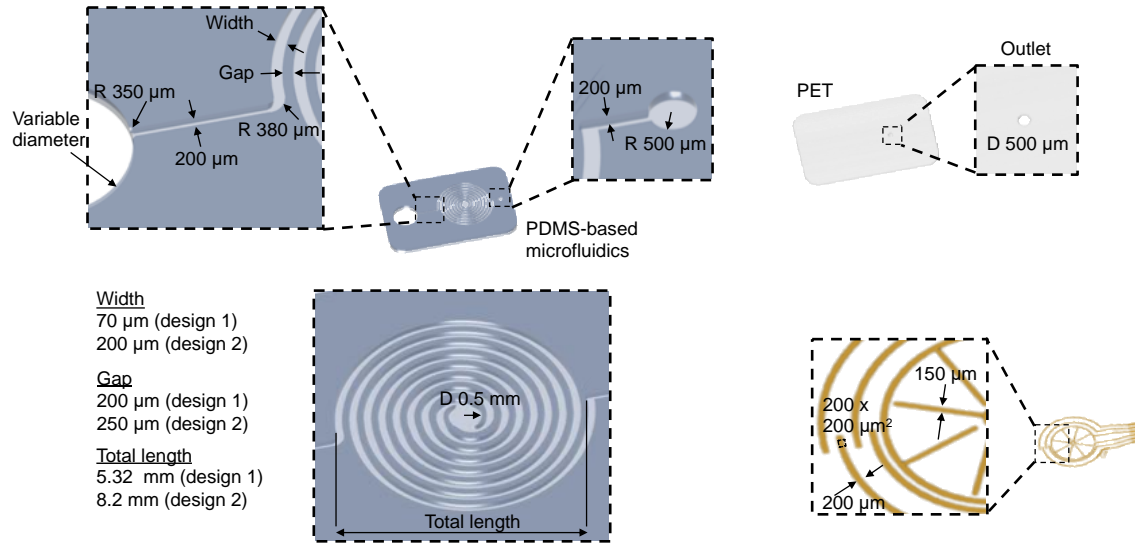
5.9.4 Figure S2: Structure and function of the hydrogel-filler stack in the sweat collection well.
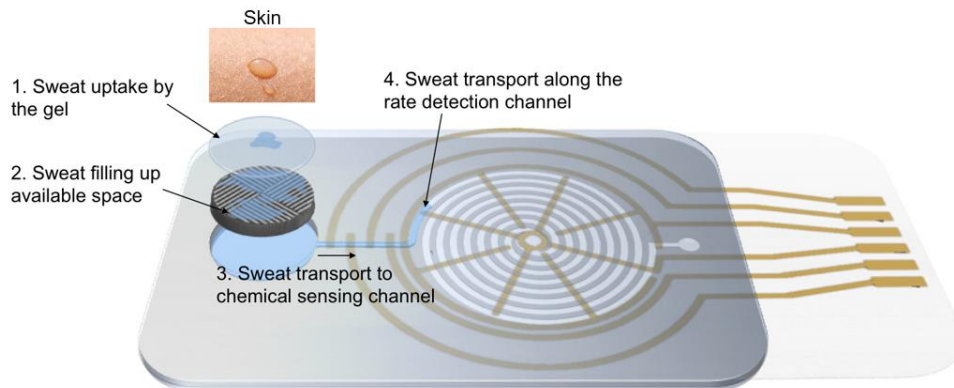
Figure S3. Optical images of the microfluidic patch and filler component. a) Image of the assembled patch with PDMS microfluidic and electrode layers. b) Image of the SU8 filler after fabrication of PET backing substrate. The filler has grooves for sweat to flow through but is connected and held together due to overexposure of SU8 during lithography. The filler is peeled off the PET backing for insertion into the collection well.

Figure S4. Sweat rate sensor can be used to detect a) flow rate in a short period of time with assistance of the hydrophilic filler. The collection well of the sensor has a 3 mm diameter and can hold ~ 2.8 μL of fluid. The flow rate corresponds to 1700 nL min^{-1} cm^{-2}. The sensor can detect b) flow rate as low as 2 nL min^{-1}. Flow rate is measured electrically via admittance between the spoked electrodes underlying the channel. Note that injection pumps set to nL min^{-1} flow rates can generate pulsatile flow, causing some variations and transient effects in flow rate measured in the device.

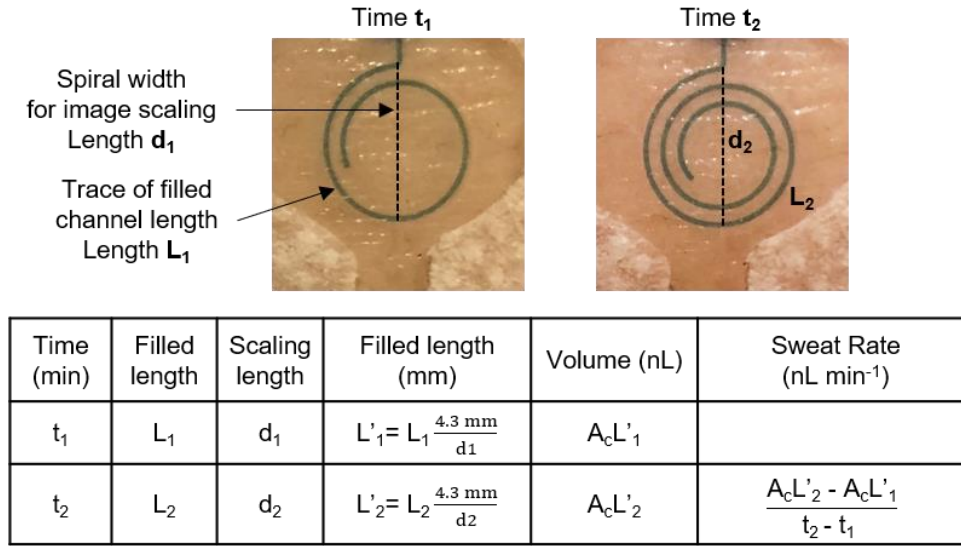*5.9.7 Figure S5: Image processing for optical sweat rate measurement.*

Time (min)	Filled length	Scaling length	Filled length (mm)	Volume (nL)	Sweat Rate (nL min^{-1})
t_1	L_1	d_1	$L'_1 = L_1 \frac{4.3 \text{ mm}}{d1}$	$A_cL'_1$	
t_2	L_2	d_2	$L'_2 = L_2 \frac{4.3 \text{ mm}}{d2}$	$A_cL'_2$	$\dfrac{A_cL'_2 - A_cL'_1}{t_2 - t_1}$

Figure S5. Image processing for optical sweat rate measurement. Blue dye aids in identifying the channel length occupied by sweat. In AutoCAD, a trace is made of this filled blue length and of the microfluidic spiral diameter (dashed black), which has a known length (4.8 mm for the patch worn on the finger as shown below) that can be used to scale and convert the processing software trace length into real-world units. This length is multiplied by the cross sectional area A_c (200 µm x 70 µm) to give the total sweat volume in the channel. This volume is subtracted from the calculated volume at the subsequent time point and divided by the intervening time to calculate the average sweat rate between when the images were recorded.

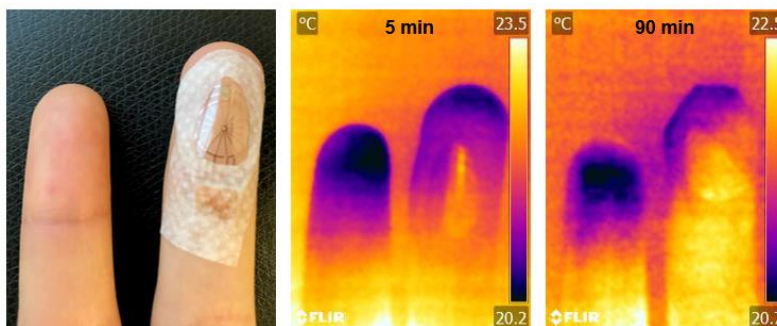*5.9.8 Figure S6: Heat generation analysis during on-body patch attachment*

Figure S6. Heat generation analysis during on-body patch attachment. Thermal infrared images captured 5 min and 90 min into on-body sensor wear. There is negligible difference in local skin surface temperature produced by the patch.

5.9.9 Figure S7: Comparison of sweat rate measured by the microfluidic sweat patch and the gravimetric method.
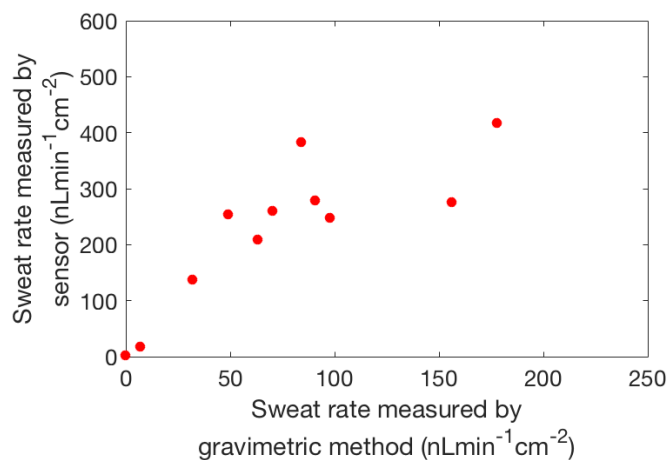

Figure S7. Comparison of sweat rate measured by the microfluidic sweat patch and the gravimetric method. Sweat rate measured by the sweat patch is 2 times higher than that measured by the gravimetric method.

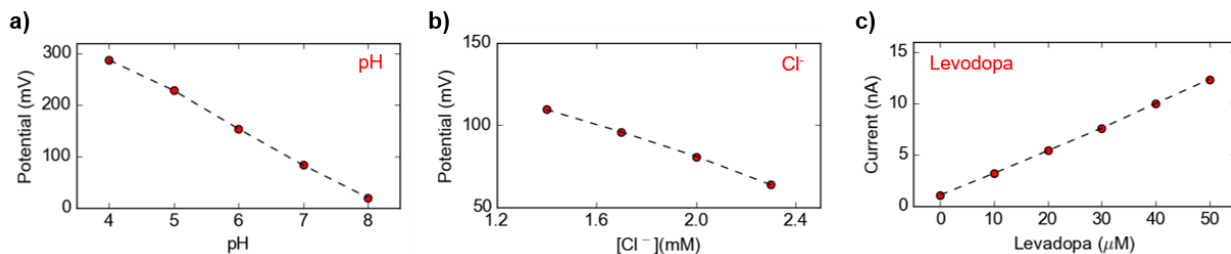*5.9.10 Figure S8: Calibration plots showing linear response of pH, Cl⁻, and levodopa sensors.*

Figure S8. Calibration curves of sensor signal versus analyte concentration for a) pH, b) Cl⁻, and c) levodopa. Data is obtained from the potentiometry and chronoamperometry curves in Figure 3f-h and demonstrates each sensor's linear response.

5.9.11 Figure S9: Reproducibility, stability, and bending tests of pH, Cl⁻, and levodopa sensors.
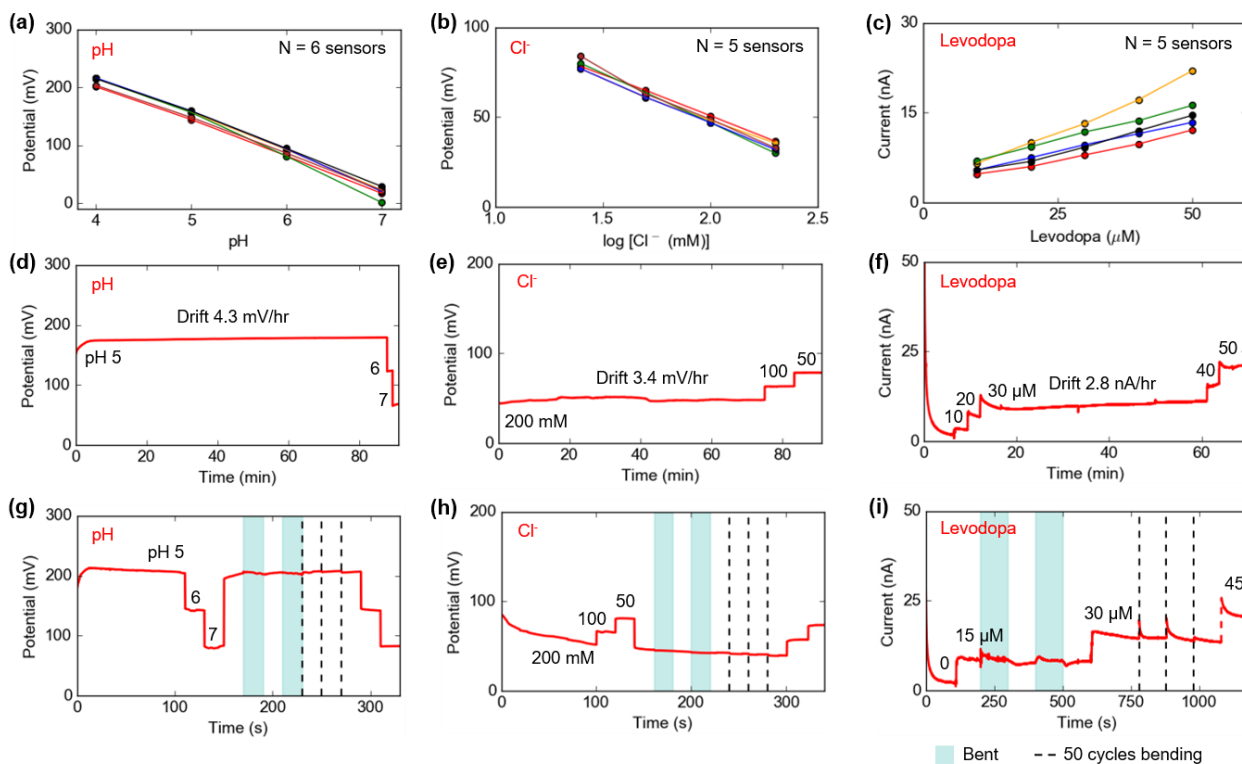

Figure S9. (a)-(c) Reproducibility, (d)-(f) stability and drift analysis, and (g)-(i) bending tests using 0.66 cm radius of curvature for the pH, Cl⁻, and levodopa sensors.

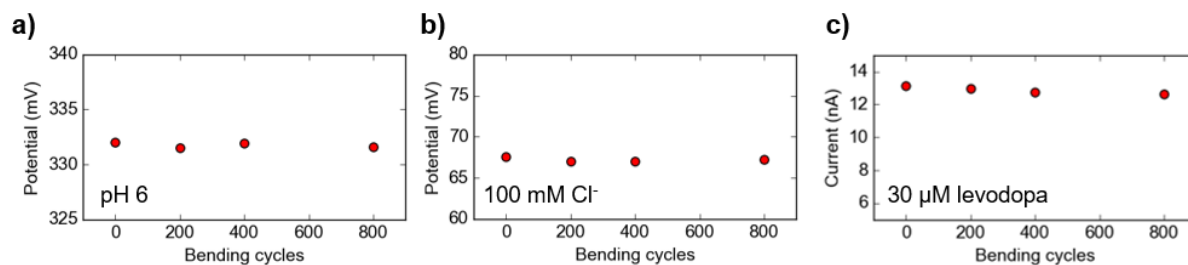*5.9.12 Figure S10: Extended bending tests of pH, chloride, and levodopa sensors.*

Figure S10. Extended bending tests of pH, chloride, and levodopa sensors. Sensor signals are reported before bending and after 200, 400, and 800 cycles of bending with 0.66 cm radius of curvature.

Chapter 6: Summary and Outlook

Wearable sensors have shown great promise for overcoming the limitations of traditional, reactive, hospital-based health assessments. Sweat sensors in particular have exciting prospects for non-invasively deriving insights into the body's chemical state. This dissertation has highlighted multi-disciplinary efforts towards making sweat sensing ubiquitous. This includes high-throughput fabrication methods such as roll-to-roll gravure printing of electrochemical electrodes and laser patterning of adhesive layers for rapidly assembled microfluidics. Integrated microfluidic sensors were presented to enable dynamic sweat capture and analysis for continuous measurement of sweat secretion rate and analyte levels. Such systems pave the way for correlation studies to compensate for dilution of analyte levels at high secretion rates, to use multiplexed sensing to identify relationships between the secretion mechanisms and concentrations of different analytes, and to broadly decode how evolving sweat concentrations relate to deeper body physiology. Finally, wearable sensors were presented that enable sweat sensing during daily activities, including while sitting or sleeping, instead of relying on disruptive modes of sweat generation such as exercise, thermal treatment, or iontophoresis. These systems represent a key advancement for enabling sweat sensing to become a viable, routine approach to personalized health monitoring.

There are many aspects of sweat sensing that must be further developed to take the field forward. Apart from the big challenges associated with interpreting sensor data for predictive healthcare, improvements at the device level will also contribute to how reliable and useful sweat sensor measurements can be. Areas where further research and development is needed include finding better ways of packaging sensors into robust and easy-to-wear systems that are less susceptible to noise from strain or motion, particularly at the interface between soft sensing components and more rigid electronics. Reducing power consumption is another consideration for advancing sensor prototypes beyond the initial research stage. Moving towards ASIC technologies to consolidate electronics, reduce power, and miniaturize devices can help improve sensor usability. Even more crucially, developing methods to induce sweat secretion in sedentary environments is critical to expanding the opportunities for sweat-based health monitoring beyond athletic applications where sweat is readily available. Iontophoresis has shown promise for one-time measurement, but reducing current density demands, fabricating highly miniaturized sensors operable at low secretion rates, or developing alternate techniques for biomarker extraction will be necessary to enable continuous monitoring. To expand the wearable platform towards new analytes, more work is needed to develop sensitive and selective techniques for measuring sweat hormones and proteins amongst other complex analytes. To date, such sensors have been difficult to realize due to the intrinsic complexities of using antibodies or aptamers as biorecognition

elements, but these sensors could potentially give tremendous insight into the physiological state of our bodies. For sensors that have already been demonstrated towards simpler analytes like ions and metabolites, further work is needed to ensure they provide reliable, actionable data. More robust and stable sensing components must be designed to enable long-term use. Incorporating microfluidics and multiplexed sensing to improve data integrity must be combined with higher level investigation into the physiological relevance of sweat analytes using large-scale correlation studies. Parallel efforts to ensure safe handling of data, and adapting high-throughput fabrication methods, are also needed to make sweat sensors viable for wider use. These varied considerations present many opportunities for advancing sweat sensor technology, with the ultimate goal of enabling non-invasive probing of our bodies at molecular levels for diverse applications in personalized and predictive healthcare.